



저작자표시-비영리-변경금지 2.0 대한민국

이용자는 아래의 조건을 따르는 경우에 한하여 자유롭게

- 이 저작물을 복제, 배포, 전송, 전시, 공연 및 방송할 수 있습니다.

다음과 같은 조건을 따라야 합니다:



저작자표시. 귀하는 원저작자를 표시하여야 합니다.



비영리. 귀하는 이 저작물을 영리 목적으로 이용할 수 없습니다.



변경금지. 귀하는 이 저작물을 개작, 변형 또는 가공할 수 없습니다.

- 귀하는, 이 저작물의 재이용이나 배포의 경우, 이 저작물에 적용된 이용허락조건을 명확하게 나타내어야 합니다.
- 저작권자로부터 별도의 허가를 받으면 이러한 조건들은 적용되지 않습니다.

저작권법에 따른 이용자의 권리는 위의 내용에 의하여 영향을 받지 않습니다.

이것은 [이용허락규약\(Legal Code\)](#)을 이해하기 쉽게 요약한 것입니다.

[Disclaimer](#)

공학박사 학위논문

**Study on Numerical PMM Tests for
Prediction of Ship Manoeuvring
Coefficients in Waves**

파랑 중 선박 조종계수 추정을 위한 수치
PMM 해석에 대한 연구

2022년 8월

서울대학교 대학원

조선해양공학과

주 장

파랑 중 선박 조종계수 추정을 위한
수치 PMM 해석에 대한 연구

Study on Numerical PMM Tests for Prediction of
Ship Manoeuvring Coefficients in Waves

지도 교수 김 용 환

이 논문을 공학박사 학위논문으로 제출함
2022년 7월

서울대학교 대학원
공과대학 조선해양공학과
주 장

주장의 공학박사 학위논문을 인준함
2022년 7월

위 원 장 _____ 남 보 우

부 위 원 장 _____ 김 용 환

위 원 _____ 양 경 규

위 원 _____ 성 영 재

위 원 _____ 김 연 규

ABSTRACT

In recent years, the international long-term actions to cut greenhouse gas (GHG) emissions and carbon intensity from shipping have been proposed to address climate change. To improve the ship operational efficiency with lower fuel consumption and reduced CO₂ emissions, the International Maritime Organization (IMO) adopted the Energy Efficiency Design Index (EEDI) as the mandatory energy efficiency regulation for new ships. The regulations have set out the objectives that aim to reduce at least 50% of the total annual GHG emissions from international shipping by 2050 compared to 2008.

However, the EEDI reduction requirement and possible lower propulsion installment have risen a major concern that the underpowered ship could lose its manoeuvrability and safety when the ocean environment becomes harsh. Accordingly, the Marine Environment Protection Committee (MEPC) announced the guidelines for determining minimum propulsion power to maintain the manoeuvrability of ships in adverse conditions (**MEPC, 2017**). It emphasized the minimum power line that considers the ship manoeuvring motion in adverse weather. Therefore, the prediction of ship manoeuvrability in waves is a technical need for both ship operation and ship safety.

To evaluate ship manoeuvrability in waves, one of the major approaches has been the coupled seakeeping-manoeuving analysis, and many efforts have been proposed in the past decades for a deliberate prediction of the wave drift forces. However, the main limitation of such coupling analysis is that the simplified manoeuvring model and corresponding manoeuvring coefficients are obtained based on the calm-sea condition. The wave effect on those models and coefficients was neglected. Thus, it is necessary to revisit the mathematical models or manoeuvring coefficients under wave effects.

This study aims to observe the wave effects on the manoeuvring coefficients by conducting a series of planar motion mechanism (PMM) tests under waves. The test model is the KCS containership model. Firstly, a moving numerical tank is built based on the CFD method, and the dynamic wave field is generated and maintained via the volume of fluid (VOF) based wave forcing function. The coupling motion between the prescribed PMM movement and the wave-induced motion responses are achieved by a quaternion-based 6-DOF motion algorithm, and a stabilized $k-\omega$ SST turbulence model is considered for the strong turbulent flows that occur during ship PMM motion.

Secondly, the numerical uncertainties and validation have been examined for the calm-sea PMM test and the seakeeping test of the KCS model. For the calm-sea PMM cases, multiple PMM tests including static drift test, pure sway test, pure yaw test, and combined drift-yaw test have been validated with the experimental measurement. For the ship seakeeping test, the wave-induced motion responses and added resistance are examined with respect to different wave frequencies or wave directions.

Thirdly, the incident wave conditions are introduced for the traditional PMM tests. The coupling between the low-frequency PMM motion and the high-frequency wave-induced motions has caused the issues, such as the dynamic ship orientation in waves, and the possible memory effect of the dynamic PMM tests. These issues were discussed. Various wave conditions were considered for the PMM tests, and the manoeuvring coefficients were observed under the effects of wave frequency, wave slope, and wave direction.

Keyword: manoeuvrability in waves, manoeuvring coefficients, PMM test, CFD, KCS

학번: 2017-34082

Content

1. Introduction	1
1.1 Research background	1
1.2 Research objectives	6
2. PMM Tests for Ship Manoeuvring	9
2.1 Ship manoeuvring model	9
2.2 Ship PMM tests	12
2.3 Study outline	18
3. Numerical Method	23
3.1 Basic solver	23
3.2 Finite volume discretization	25
3.3 Turbulence model	27
3.4 Computational conditions	28
3.4.1 Computational domain	28
3.4.2 Boundary conditions	31
3.4.3 Computational cost	33
4. Numerical Uncertainties	36
4.1 Procedure of uncertainty estimation	36
4.2 Case I: PMM test in calm sea	41
4.2.1 Uncertainty of time window	41
4.2.2 Uncertainty of boundary layer mesh	46
4.2.3 Uncertainty of discretization parameter	54
4.3 Case II: Seakeeping test	63
4.3.1 Uncertainty of time window	63

4.3.2	Uncertainty of discretization parameters	65
5.	Validation of Numerical Method	73
5.1	Case I: PMM test in calm sea	73
5.1.1	Static drift test	73
5.1.2	Pure sway test	77
5.1.3	Yaw test	80
5.2	Case II: Seakeeping test	84
5.2.1	Wave frequency effect	84
5.2.2	Wave direction effect	87
6.	Numerical PMM Tests in Waves	95
6.1	Wave frequency effect	96
6.1.1	Static drift test	96
6.1.2	Pure yaw test	106
6.2	Wave slope effect	113
6.2.1	Static drift test	114
6.2.2	Pure yaw test	125
6.3	Wave direction effect	130
6.3.1	Static drift test	131
6.3.2	Pure yaw test	136
7.	Conclusions	142
	Reference	145
	APPENDIX	155

List of Tables

Table 2.1 Force/moment components and corresponding manoeuvring coeffs. of each PMM tests.....	17
Table 2.2 Main particulars of KCS hull	20
Table 2.3 Overview of the V&V study I: PMM tests in calm sea.....	21
Table 2.4 Overview of the V&V study II: seakeeping tests	21
Table 2.5 Overview of the study cases: PMM tests in waves	22
Table 3.1 Boundary conditions of flow fields	31
Table 3.2 Main features of two computational resources.....	33
Table 3.3 Estimated computational cost based on 100 cluster cores.....	35
Table 4.1 Time window uncertainty of static drift test, $\beta_0=18^\circ$	43
Table 4.2 The time window uncertainty of drift-yaw test, $r_0'=0.5$, $\beta_0=12^\circ$...	45
Table 4.3 Uncertainty of the boundary mesh resolution for static drift test, $\beta_0 =$ 18° (fixed: $L/\Delta x = 380$, $1/\Delta t = 200$)	49
Table 4.4 Uncertainty of the boundary mesh resol. for drift-yaw test, $r_0' = 0.5$, $\beta_0 = 12^\circ$ (fixed: $L/\Delta x = 380$, $1/\Delta t = 200$)	53
Table 4.5 Uncertainty of the general mesh resolution for static drift test, $\beta_0 =$ 18° (fixed: $L/\Delta n = 10^4$, $1/\Delta t = 200$).....	56
Table 4.6 Uncertainty of the general mesh resolution for drift-yaw test, $r_0' =$ 0.5 , $\beta_0 = 12^\circ$ (fixed: $L/\Delta n = 10^4$, $T_0/\Delta t = 2236$)	59
Table 4.7 Uncertainty of the time-step for static drift test, $\beta_0 = 18^\circ$ (fixed: $L/\Delta x = 380$, $L/\Delta n = 10^4$).....	60
Table 4.8 Uncertainty of the time-step for drift-yaw test, $r_0' = 0.5$, $\beta_0 = 12^\circ$ (fixed: $L/\Delta x = 380$, $L/\Delta n = 10^4$).....	61
Table 4.9 Time window uncertainty of the seakeeping test ($\lambda/L = 1.0$).....	65
Table 4.10 Test cases with different discretization parameters	66

Table 4.11 Uncertainty of the mesh resolution for seakeeping test (fixed: $\Delta x/\Delta z = 9$, $U_e \cdot \Delta t/\Delta x = 0.20$)	69
Table 4.12 Uncertainty of the time-step for seakeeping test (fixed: $\lambda/\Delta x = 100$, $U_e \cdot \Delta t/\Delta x = 0.20$)	72

List of Figures

Fig. 2.1 Ship 6-DOF motions in coordinate systems	9
Fig. 2.2 Ship planar motion variables in coordinate systems	12
Fig. 2.3 Ship PMM trajectories	13
Fig. 2.4 KCS bare hull.....	18
Fig. 2.5 KCS body plan.....	18
Fig. 3.1 Computational domain.....	29
Fig. 3.2 Distribution of exponential wave forcing weights ($\lambda = L$)	30
Fig. 3.3 Unstructured mesh system	30
Fig. 3.4 Scalability of present computational machines.....	34
Fig. 4.1 Flowchart of uncertainty estimation	37
Fig. 4.2 Example of the grid convergence test for combined drift-yaw test .	40
Fig. 4.3 Force/moment signals of static drift test, $\beta_0 = 18^\circ$	42
Fig. 4.4 Force/moment signals of combined drift-yaw test, $r_0'=0.5, \beta_0=12^\circ$.	44
Fig. 4.5 Mesh structure near hull surface	46
Fig. 4.6 Convergence test of boundary mesh resolution, $\beta_0=18^\circ$	47
Fig. 4.7 Surface y^+ field of static drift test, $\beta_0=18^\circ$	50
Fig. 4.8 Convergence test of boundary mesh resolution, $r_0'=0.5, \beta_0=12^\circ$	52
Fig. 4.9 Convergence test of mesh resolution, $\beta_0=18^\circ$	55
Fig. 4.10 Convergence test of mesh resolution, $r_0'=0.5, \beta_0=12^\circ$	58
Fig. 4.11 Force/moment signals with different time-steps, $r_0'=0.5, \beta_0=12^\circ$..	62
Fig. 4.12 Typical motion and resistance signals, $\lambda/L=1.0, H/\lambda=1/60$	64
Fig. 4.13 Wave profiles inside the wave tank.....	66
Fig. 4.14 Convergence test of mesh resolution on the wave elevations.....	67
Fig. 4.15 Convergence test of mesh resolution on motion and added resistance	68

Fig. 4.16 Convergence test of time step on the wave elevations.....	70
Fig. 4.17 Convergence test of time step on motion and added resistance.....	71
Fig. 5.1 Free surface pattern of static drift test, $\beta_0 = 18^\circ$	73
Fig. 5.2 Streamlines and vorticity field near the hull, $\beta_0 = 18^\circ$	74
Fig. 5.3 Comparison of the normalized force/moment w.r.t. drift angle	76
Fig. 5.4 Sequential wave pattern of pure sway test, $v_0' = 0.309$ ($t/T_0 = 1.00$, 1.25, 1.50, 1.75).....	78
Fig. 5.5 Comparison of the normalized force/moment w.r.t. sway acceleration	79
Fig. 5.6 Sequential wave pattern of pure yaw test $r_0' = 0.5$ ($t/T_0 = 1.00$, 1.25, 1.50, 1.75)	81
Fig. 5.7 Force/moment signals of the combined drift-yaw test.....	82
Fig. 5.8 Comparison of the normalized force/moment w.r.t. drift angle and yaw rate	83
Fig. 5.9 Comparison of the motion responses w.r.t. wavelength.....	85
Fig. 5.10 Comparison of the added resistance w.r.t. wavelength	86
Fig. 5.11 Comparison of the motion responses w.r.t. wave direction.....	89
Fig. 5.12 Comparison of the added resistance w.r.t. wave direction	90
Fig. 5.13 Sequential wave patterns under different wave directions (a)	92
Fig. 5.14 Sequential wave patterns under different wave directions (b)	93
Fig. 5.15 Surface distribution of added pressure under different wave directions	94
Fig. 6.1 Sequential development of wave pattern and hull dynamic pressure	97
Fig. 6.2 Sequential development of wave pattern and hull dynamic pressure	98
Fig. 6.3 Sequential development of wave pattern and hull dynamic pressure	99
Fig. 6.4 Force/moment signals under different wavelengths, $\beta_0 = 18^\circ$	100
Fig. 6.5 Ship motion RAOs w.r.t. wavelengths and drift angles	102

Fig. 6.6 Added forces and moment w.r.t. wavelengths.....	103
Fig. 6.7 Relation between added force/moment and drift angle.....	104
Fig. 6.8 Wavelength effect on the coefficients Y_v and N_v	105
Fig. 6.9 Sequential wave pattern of the pure yaw test in waves.....	107
Fig. 6.10 Sequential vorticity field of the pure yaw test in waves	108
Fig. 6.11 Force/moment signals under different wavelengths, $r_0' = 0.5$	110
Fig. 6.12 Added forces and moment w.r.t. wavelengths.....	111
Fig. 6.13 Wavelength effect on the coefficients Y_r and N_r	112
Fig. 6.14 Ship waterlines under different wave slopes.....	113
Fig. 6.15 Force/moment signals under different wave slopes, $\beta_0 = 18^\circ$	115
Fig. 6.16 The nonlinear phenomena under different wave slopes, $\beta_0 = 18^\circ$	116
Fig. 6.17 Wave patterns under various wave slopes, $\beta_0 = 18^\circ$	118
Fig. 6.18 Added pressure distribution under various wave slopes, $\beta_0 = 18^\circ$	119
Fig. 6.19 Exciting vertical force Z and heave motion ξ_3 w.r.t. wave slope..	121
Fig. 6.20 Exciting pitch moment M and pitch motion ξ_5 w.r.t. wave slope .	122
Fig. 6.21 Force/moment of the static drift test w.r.t. wave slope.....	123
Fig. 6.22 Wave slope effect on the manoeuvring coefficients Y_v and N_v	124
Fig. 6.23 Motion signal of the pure yaw test in waves.....	126
Fig. 6.24 Force/moment signal of the pure yaw test in waves	127
Fig. 6.25 Wave slope effect on the added force/moment of pure yaw test..	128
Fig. 6.26 Wave slope effect on manoeuvring coefficients.....	129
Fig. 6.27 Wave incident direction for the manoeuvring ship	130
Fig. 6.28 Wave direction effect on wave-induced motions for static drift tests	132
Fig. 6.29 Wave direction effect on added force/moment for static drift test	133
Fig. 6.30 Wave direction effect on the manoeuvring coefficients Y_v and N_v	135
Fig. 6.31 Signals of ship motion for the pure yaw test in an oblique sea....	138

Fig. 6.32 Signals of ship force/moment for the pure yaw test in an oblique sea	139
Fig. 6.33 Wave direction effect on the wave-induced motions for pure yaw test	140
Fig. 6.34 Wave direction effect on the manoeuvring coefficients N_r	141

1. Introduction

1.1 Research background

In recent decades, the greenhouse gas (GHG) emissions and carbon intensity from the shipping industry becomes a concern to the international maritime society. More demands turn to the improvement of ship operation efficiency and the reduction of GHG emissions. To this end, the International Maritime Organization (IMO) set up a long-term project to cut the GHG emissions from shipping and adopted the Energy Efficiency Design Index (EEDI) as the mandatory energy efficiency regulation in 2011. The new ships are required to have improved operational efficiency and reduced fuel consumption, the global target is to reduce at least 50% of the total annual GHG emissions from the international shipping industry by 2050 compared to 2008.

On the other hand, the new ships that satisfy the growing EEDI requirement might be underpowered so the harsh ocean environment would be risky to the ship's manoeuvrability and safety. Accordingly, the Marine Environment Protection Committee (MEPC) of IMO proposed the guidelines for determining minimum propulsion power to maintain the manoeuvrability of ships in adverse conditions (**MEPC, 2017**). The target is to assess a minimum power line above which the ship would not lose its manoeuvrability when adverse weather is coming. Therefore, the prediction of ship manoeuvrability in waves is a technical need for both ship operation and ship safety.

The main approaches to evaluating ship manoeuvrability include the sea trial, direct manoeuvring model tests, mathematical manoeuvring models, and empirical formulas. The sea trial and direct model tests provide more direct

observations of ship various manoeuvring performances, and the testing or manoeuvring trajectories are more close to what happens in the real ocean environment. The mathematical manoeuvring model decomposes the ship manoeuvrability into manoeuvring coefficients (also called hydrodynamic coefficients or manoeuvring derivatives). The manoeuvring coefficients provide an insightful understanding of the ship manoeuvring performance under the single or coupled motion conditions. The empirical formula is proposed based on a wide database of ship manoeuvring performance, and this method is almost free of time-consuming.

To couple the traditional manoeuvring problem with the seakeeping effect, the seakeeping-manoeuving coupling analysis has been widely conducted by either free-running tests or numerical analysis. The early works that carried out the ship manoeuvring tests in regular or irregular waves can be found by **Hirano et al.(1980)**, **Hirayama and Kim (1994)**, **Ueno et al. (2003)**, **Yasukawa (2006, 2008)**, **Sanada et al. (2013)**. **Yasukawa et al. (2015)** conducted the free-running tests of a KVLCC2 model in irregular sea. The turning circle test and zigzag test have been compared with the results of MMG-based predictions. **Sprenger et al. (2016)** carried out a joint project on the ship manoeuvring performance in waves. The KVLCC2 tanker and the DTC containership have been selected to observe the wave frequency effect and the wave direction effects. **Kim et al. (2019)** performed the turning circle tests of a KVLCC2 tanker in regular waves. The drifting distance and the drift angles were observed to be convergent as the turning becomes larger than 360°. **Rablias and Kristiansen (2019)** considered the uncertainty analysis for the course keeping test, the turning circle test, and the zigzag test in waves. The ship model is the DTC containership, and various wave directions were involved. **Hasnan et al. (2019)**, **Yasukawa et al. (2020)**, **Yasukawa et al.**

(2021) have conducted a series of turning circle tests in regular and irregular waves based on KCS container model and KVLCC2 tanker model. **Kim et al. (2020)** focus on the initial turning capability of a manoeuvring ship from ship safety viewpoint. The KCS containership model was considered, and the effects of wave steepness and wave frequency were investigated. **Milanov et al. (2021)** observed the ship controllability in waves at low speed, considering the EEDI requirements on ship power consumption and propeller restriction.

On the numerical works of ship seakeeping-manoeuving analysis. **Skejjic and Faltinsen (2008)**, **Yasukawa and Nakayama (2009)**, and **Yen et al. (2010)** applied the two-time-scale models involving the wave drift forces. **Seo and Kim (2011)** applied the three-dimensional Rankine panel method for the nonlinear wave drift forces, with the approximation of a uniform flow on the time-varying ship speed. **Zhang et al. (2017)** considered the vortex shedding phenomenon of ship manoeuvring motion by implementing the vortex sheet technique into the seakeeping-manoeuving analysis. **Wicaksono and Kashiwagi (2019)** investigated the coupling effect contributed by the wave drift forces of each direction. **Lee et al. (2020)** considered the steady-flow induced effect for the ship seakeeping part handled by the three-dimensional Rankine panel method. **Lee et al. (2021)** enhanced the traditional two-time-scale method by introducing a bilinear model that considered the wave effects on the ship manoeuvring model.

To obtain the manoeuvring coefficients used for the mathematical manoeuvring models, either empiric or algorithm-based prediction (e.g., **Abkowitz, 1980; Clarke et al. 1983, Kijima et al., 1990; Yamato et al., 1990; Oltmann, 1992; Haddara and Wang, 1999; Hess et al., 2000; Vantorre, 2001; Mahfouz et al., 2003**), or the captive manoeuvring test that includes Planar Mechanic Mechanism (PMM) test or Circular Motion Test

(CMT) is generally considered; and the captive manoeuvring tests seem to provide more reliable coefficients at nowadays research stage. The philosophy of the PMM test is to obtain the dynamic motion coefficients of a rigid body by a series of forced motions. The forced motion pattern is designed to achieve the desired motion condition so that the external force/moment of the body can be obtained at this desired motion condition. Its application in the field of naval architecture has been widely discussed in the period 1960 ~ 1980, for example, **Gertler (1959)**, **Goodman (1960)**, **Strom-Tejsen and Chislett (1966)**, **Smitt and Chislett (1974)**, **Nomoto (1975)**, **Goodman et al. (1976)**, **Grim et al. (1976)**, **Vantorre and Eloot (1997)**. These works have been focusing on the specific PMM carriage and the limitation of the traditional towing tanks. The investigations have been carried out to understand the physics such as lateral motion amplitude, oscillatory frequency, memory effect, and blockage effect. The conclusions of these works have been systematically summarized in the recommendation brochure of ITTC which has been continuously updated (**ITTC, 2021**).

The main works of PMM tests in recent two decades become the applications. Particularly with the increasing trend of CFD computations, the virtual tank becomes an alternative way of carrying out PMM tests. Many works have covered both the experimental tests and the numerical tests, and the validation has provided a more reliable prediction of ship manoeuvring characteristics. The systematic study on the PMM tests of DTMB 5415 has been carried out by **Yoon (2009)** and **Sakamoto (2009)**, and these two works are based on the towing tank experiments and the CFD computations, respectively. The experimental uncertainties and the numerical uncertainties have been estimated, and the vortex shedding phenomenon has been examined in this PMM test. **Cura-Hochbaum (2011)** developed an in-house

RANS model for the virtual PMM tests. The PMM test results of KVLCC2 hull have been further applied to simulate ship manoeuvring trajectory. **Simonsen et al. (2012)** compared the experimental measurement and the numerical computation on the static drift tests of KCS hull. **Xing et al. (2012)** investigated the vortex shedding phenomenon of the static drift test based on the DES solver. A double-body model of KVLCC2 hull was employed to observe the surface streamlines and shedding vortical structures. As a continued work, **Abdel-Maksoud et al. (2016)** carried out the corresponding experiment of the double-body model in a wind tunnel, and a very large drifting condition of 30° was involved for observing the vortex shedding phenomenon. **Sung and Park (2015)** conducted both the experimental tests and the numerical computations for the large-scaled KCS and KVLCC models. The satisfactory agreements have been achieved on the PMM tests, and the manoeuvring coefficients were further applied for predicting ship manoeuvring trajectories. **Liu et al. (2018)** carried out the numerical PMM tests of KCS model with a commercial CFD solver. The work has investigated the Froude number effect with a series of PMM tests. **Islam and Soares (2018)** applied the OpenFOAM solver to the PMM tests of KCS model. The certain discrepancy with the experimental data was found on the pure yaw tests. **Ren et al. (2020)** focused on the vortex behavior of ship PMM tests. The four vortex identification methods were compared on the vortex shedding of various ship PMM motions. **Yao et al. (2021)** employed the OpenFOAM solver for the KVLCC2's PMM tests. The double-body model was considered, and the virtual disk was added to generate the ship manoeuvring coefficients.

With the recent concerns on the ship manoeuvrability in waves, it becomes necessary to consider the traditional PMM tests in waves. **Yasukawa and Adnan (2006)** carried out the static drift test in head sea and beam sea. The

containership model S-175 was given a 6-DoF motion, and the wave drift forces and moment were observed under the coupling between the incident waves and lateral drifting motions. **Xu et al. (2007)** conducted a series of pure sway tests in head waves, which observed the wave frequency effect and the wave slope effect on the damping forces. **Sung et al. (2012)** applied to towing tank facility for an obliquely towing test of KCS containership. The wavelength effect has been investigated based on several oblique angles. **Yasukawa et al. (2010)** developed a strip theory based solver to predict the ship static drift motion in head sea and beam sea. **Lee et al. (2020)** combined the vortex sheet technique with the time-domain Rankine panel method, and calculated the wave drift forces for ship manoeuvring in waves. **Zhang et al. (2020)** also used the Rankine panel method to validate the static drift test of S-175 containership in head and beam sea. **Lee et al. (2021)** proposed a bilinear model that considers the wave effect on ship manoeuvring coefficients, and the bilinear coefficients were obtained by a series of potential-based computations on the steady drifting motion and the steady yawing motion in waves.

1.2 Research objectives

The main objective of this study is to observe the ship manoeuvring coefficients under the effects of various wave conditions. To this end, a series of PMM tests in waves are carried out to observe the effect of wave frequency, wave slope, and wave direction. The numerical tank is selected, and the overall works can be categorized as follows.

1) Construction of a numerical tank for multiple PMM tests

Given the spatial limitation of experimental tanks, the primary objective is to construct a flexible numerical tank that can be used for multiple PMM tests in various wave conditions. The 6-DoF body-wave interaction algorithm will be modified to handle the coupling of prescribed planar motions and wave-induced motions. An effective wave forcing function will be implemented to generate and maintain the numerical wave fields inside the tank, and the overproduction phenomenon of turbulence fields will be controlled by an enhanced version of the $k-\omega$ SST turbulence model. Meanwhile, the computational efficiency will be summarized so as to understand the total cost of conducting a series of PMM tests.

2) Numerical uncertainties and validation tests

The estimation of numerical uncertainty as well as the validation tests are necessary for both the calm-sea PMM tests and the seakeeping tests. The uncertainties of time window, grid resolution and time step will be estimated for the different types of tests, the static drift test, the dynamic PMM test, and the seakeeping tests. For validation, a wide range of PMM tests that covers static tests, pure dynamic tests, and combined dynamic tests will be considered and compared with the experimental measurement. The seakeeping test will also be carried out under different wave frequencies and wave directions, and the validation of ship motions and added resistance will be used to examine the effectiveness of the numerical wave field and the 6-DOF body-wave interaction module.

3) Study of the various wave effect on manoeuvring coefficients

To investigate the wave effect on ship manoeuvring coefficients, the PMM tests will be conducted under various wave conditions. Three wave parameters will be observed, namely wave frequency, wave slope, and wave direction. The hydrodynamic characteristics (e.g., the wave pattern and the added pressure distribution) will be presented to understand the ship seakeeping and manoeuvring performance. The wave added forces and moment are examined with respect to wave parameters, and the manoeuvring coefficients are observed at the last stage.

2. PMM Tests for Ship Manoeuvring

2.1 Ship manoeuvring model

The ship six-degrees-of-freedom (6-DOF) motion in three-dimensional space is defined in the body coordinate system o - xyz . The origin of body coordinate system is typically located at the mid-ship position. Fig. 2.1 shows the ship 6-DOF motion in coordinate systems. It includes three translational motions (surge x , sway y , and heave z) and three rotational motions (roll ϕ , pitch θ , and yaw ψ). The velocity u , v , w , p , q , r and corresponding accelerations are also denoted in the figure. The system o_e - $x_e y_e z_e$ denotes the space inertia system.

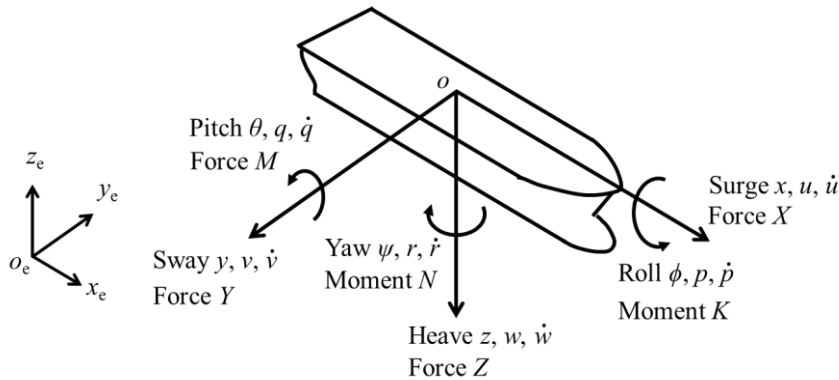


Fig. 2.1 Ship 6-DOF motions in coordinate systems

Based on the 6-DOF motion and coordinate systems, the generalized equations of ship manoeuvring motion (Abkowitz, 1969) are given as Eq. (2.1). As described in Fig. 2.1, the X , Y , N represent the surge force, sway force, yaw moment, respectively; and the K , M , N indicate the roll moment,

pitch moment, and yaw moment, respectively. The term m is ship mass, and the three-dimensional location of the ship mass center is denoted by x_G, y_G, z_G . The I_x, I_y, I_z are the ship moments of inertia in x, y, z axis. The coupling terms $(qw - rv)$, $(ru - pw)$, and $(pv - qu)$ indicate the centripetal acceleration and the terms $(I_z - I_y)qr$, $(I_x - I_z)rp$, $(I_y - I_x)pq$ represent the gyroscopic effects.

$$m[\dot{u} + qw - rv - x_G(q^2 + r^2) + y_G(pq - \dot{r}) + z_G(pr + \dot{q})] = X \quad (2.1-a)$$

$$m[\dot{v} + ru - pw - y_G(r^2 + p^2) + z_G(qr - \dot{p}) + x_G(qp + \dot{r})] = Y \quad (2.1-b)$$

$$m[\dot{w} + pv - qu - z_G(p^2 + q^2) + x_G(rp - \dot{q}) + y_G(rq + \dot{p})] = Z \quad (2.1-c)$$

$$I_x \dot{p} + (I_z - I_y)qr + m[y_G(\dot{w} + pv - qu) - z_G(\dot{u} + ru - pw)] = K \quad (2.1-d)$$

$$I_y \dot{q} + (I_x - I_z)rp + m[z_G(\dot{u} + qw - rv) - x_G(\dot{w} + pv - qu)] = M \quad (2.1-e)$$

$$I_z \dot{r} + (I_y - I_x)pq + m[x_G(\dot{v} + ru - pw) - y_G(\dot{u} + qw - rv)] = N \quad (2.1-f)$$

For the traditional 3-DOF manoeuvring equations, the ship heave, roll, and pitch motion are assumed to be neglected that $w = p = q = \dot{w} = \dot{p} = \dot{q} = 0$. Meanwhile, the hull is assumed to have a symmetric behavior so that the y_G is zero. Then the equations of motion can be simplified as follows.

$$m(\dot{u} - rv - x_G r^2) = X \quad (2.2-a)$$

$$m(\dot{v} + ru - x_G \dot{r}) = Y \quad (2.2-b)$$

$$I_z \dot{r} + mx_G(\dot{v} + ur) = N \quad (2.2-c)$$

The external forces and moment X, Y, N are contributed by the surrounding fluid, steering rudder surface, and propulsion. There are two popular

approaches to model the external force/moment by applying manoeuvring coefficients. One is the Abkowitzs model which assumes all the external force/moment are functions of ship motion parameters and rudder deflection condition (e.g. **Abkowitz, 1969**), and another one is the Maneuvering Modeling Group (MMG) model that considers the hull force, rudder force, and propulsion force as three independent mathematical models (e.g. **Yasukawa and Yoshimura, 2015**).

This study only focuses on the manoeuvring coefficients of the bare hull, and the MMG model that decomposes the bare hull, the rudder, and the propeller to be independent is selected. As given by Eq. (2.3), the forces and moment are decomposed into independent components, where the subscript “*H*”, “*R*”, “*P*” indicates the hull, rudder, and propeller.

$$X = X_H + X_R + X_P \quad (2.3-a)$$

$$Y = Y_H + Y_R \quad (2.3-b)$$

$$N = N_H + N_R \quad (2.3-c)$$

The hull force/moment is modelled as the functions of ship motion variables and corresponding manoeuvring coefficients, and the functions are expanded to be a 3rd-order Taylor series expansion.

$$X'_H = X'_* + X'_{\dot{u}}\dot{u}' + X'_{vv}v'^2 + X'_{rr}r'^2 + (X'_{vr} - Y'_{\dot{v}})v'r' \quad (2.4-a)$$

$$Y'_H = Y'_{\dot{v}}\dot{v}' + Y'_vv' + Y'_{vvv}v'^3 + Y'_{\dot{r}}\dot{r}' + (Y'_r + X'_{\dot{u}}u)r' + Y'_{rrr}r'^3 + Y'_{vrr}v'r'^2 + Y'_{vvv}v'^2r' \quad (2.4-b)$$

$$N'_H = N'_{\dot{v}}\dot{v}' + N'_vv' + N'_{vvv}v'^3 + N'_{\dot{r}}\dot{r}' + N'_rr' + N'_{rrr}r'^3 + N'_{vrr}v'r'^2 + N'_{vvv}v'^2r' \quad (2.4-c)$$

The X^* is the ship steady resistance without drift condition. The terms $X_{\dot{u}}$, $Y_{\dot{v}}$, $Y_{\dot{r}}$, $N_{\dot{v}}$, $N_{\dot{r}}$ are the added mass coefficients. The uncoupled damping coefficients (e.g. Y_v , Y_{vvv}) and the cross-coupled damping coefficients (e.g. Y_{vrr} , Y_{rvv}) indicate the derivatives of hull force or moment with respect to the ship motion condition (u , v , and r).

2.2 Ship PMM tests

Fig. 2.2 describes the ship planar motion variables of the numerical PMM tests in waves. The ship moves with a constant speed U_0 which corresponds to the Fn condition. The speed U_0 can be further decomposed into the u , v , β_0 which represents the surge velocity, sway velocity, and drift angle, respectively. The r is the yaw rate. The body forces and moment in horizontal plane are the surge force X , sway force Y , and yaw moment N . The incident waves are described by the wave frequency ω , the wave amplitude A , and the wave direction χ . The direction $\chi = 180^\circ$ indicates the head sea condition, and the direction $\chi = 0^\circ$ indicates the following sea condition.

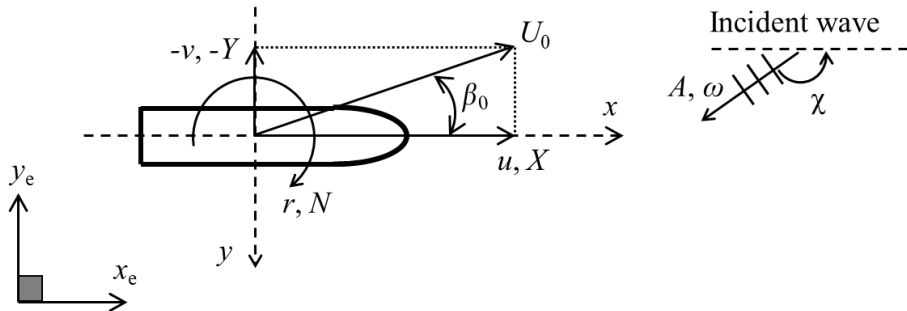


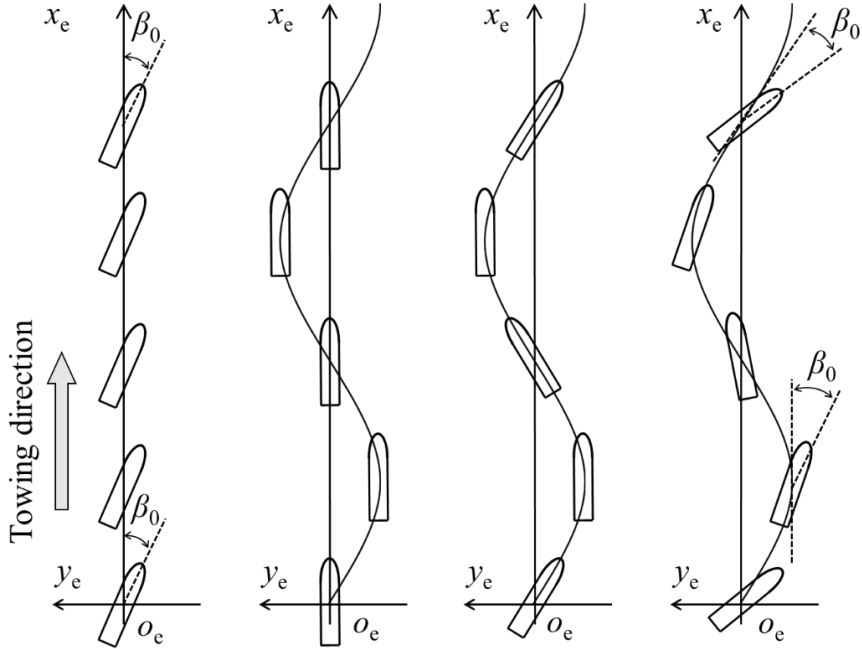
Fig. 2.2 Ship planar motion variables in coordinate systems

In this work, the harmonic force/moment components are marked by a superscript. For example, the $N^{(0)}$ means the mean component of yaw moment, and the $N^{(1,\cos)}$ represents the 1st-order cosine component of yaw moment.

Eq. (2.5) lists the normalization of motion variables and body forces. L and T are the ship length and design draft, U_0 is the total velocity determined by Froude number. ω is the frequency of PMM motion, y is the displacement in sway direction and ρ is the density of water.

$$\omega' = \frac{\omega L}{U_0} \quad y' = \frac{y}{L} \quad v' = \frac{v}{U_0} \quad \dot{v}' = \frac{\dot{v} L}{U_0^2} \quad r' = \frac{r L}{U_0} \quad \dot{r}' = \frac{\dot{r} L^2}{U_0^2} \quad (2.5-a)$$

$$X' = \frac{X}{0.5 \rho U_0^2 T L} \quad Y' = \frac{Y}{0.5 \rho U_0^2 T L} \quad N' = \frac{N}{0.5 \rho U_0^2 T L^2} \quad (2.5-b)$$



(1) Static drift test (2) Pure yaw test (3) Pure yaw test (4) Drift-yaw test

Fig. 2.3 Ship PMM trajectories

The captive PMM test can be carried out in various ways to obtain a complete list of the hull manoeuvring coefficient. This study will consider four types of tests, and the trajectories are described in Fig. 2.3.

(i) Static drift test: this is a static towing test that the ship is given a fixed drift angle β_0 with respect to the towing direction. As given by Eq. (2.6), the fixed drift angle indicates a steady sway velocity so this test is designed for sway damping coefficients. The forces and moment of this test are decomposed following Eq. (2.7). The surge force is of quadratic function, while the sway force and the yaw moment are of cubic functions. The steady resistance coefficient X_* is measured without drift condition.

$$\beta_0 = \tan^{-1}(-v/u) \quad (2.6)$$

$$X = X^{(0)} = X_* + X_{vv}v^2 \quad (2.7-a)$$

$$Y = Y^{(0)} = Y_vv + Y_{vvv}v^3 \quad (2.7-b)$$

$$N = N^{(0)} = N_vv + N_{vvv}v^3 \quad (2.7-c)$$

(ii) Pure sway test: this is a dynamic towing test that the ship is given a harmonic sway motion. The swaying motion is to achieve the prescribed sway velocity or v_0 or the prescribed sway acceleration \dot{v}_0 . To this end, the swaying frequency ω_0 and the swaying amplitude y_0 are applied as Eq. (2.8). The force/moment decomposition of this dynamic test is given by Eq. (2.9). It can be seen that the force/moment are composed of multiple harmonic components. The cosine functions are used to extract the damping coefficients related to sway velocity, and the sine functions are used to extract the added mass coefficients related to sway acceleration.

$$v = -v_0 \cos(\omega_0 t) = -y_0 \omega_0 \cos(\omega_0 t) \quad (2.8-a)$$

$$\dot{v} = \dot{v}_0 \sin(\omega_0 t) = y_0 \omega_0^2 \sin(\omega_0 t) \quad (2.8-b)$$

$$\begin{aligned} X &= X_* + X_{vv} v^2 \\ &= X^{(0)} + X^{(2,\cos)} \cos(2\omega_0 t) \end{aligned} \quad (2.9-a)$$

$$\begin{aligned} Y &= Y_{\dot{v}} \dot{v} + Y_v v + Y_{vvv} v^3 \\ &= Y^{(1,\sin)} \sin(\omega_0 t) - Y^{(1,\cos)} \cos(\omega_0 t) - Y^{(3,\cos)} \cos(3\omega_0 t) \end{aligned} \quad (2.9-b)$$

$$\begin{aligned} N &= N_{\dot{v}} \dot{v} + N_v v + N_{vvv} v^3 \\ &= N^{(1,\sin)} \sin(\omega_0 t) - N^{(1,\cos)} \cos(\omega_0 t) - N^{(3,\cos)} \cos(3\omega_0 t) \end{aligned} \quad (2.9-c)$$

(iii) Pure yaw test: this is a dynamic towing test that the ship is given a harmonic yaw motion. The ship starts with a given heading direction, and then it moves along the yawing trajectory without body lateral motion, as described in Fig. 2.3. To achieve the prescribed yawing rate or the prescribed yawing acceleration, Eq. (2.10) gives the relation with yawing frequency ω_0 and the maximum heading angle ψ_0 . The decompositions of force/moment are given by Eq. (2.11). The sine components are used to extract the damping coefficients related to yaw rate, and the cosine components are used for the added mass coefficients related to yaw acceleration.

$$\psi = -\psi_0 \cos(\omega_0 t) \quad (2.10-a)$$

$$r = r_0 \sin(\omega_0 t) = \psi_0 \omega_0 \sin(\omega_0 t) \quad (2.10-b)$$

$$\dot{r} = \dot{r}_0 \cos(\omega_0 t) = \psi_0 \omega_0^2 \cos(\omega_0 t) \quad (2.10-c)$$

$$\begin{aligned} X &= X_* + X_{rr} r^2 \\ &= X^{(0)} + X^{(2,\cos)} \cos(2\omega_0 t) \end{aligned} \quad (2.11-a)$$

$$\begin{aligned} Y &= Y_{\dot{r}} \dot{r} + Y_r r + Y_{rrr} r^3 \\ &= Y^{(1,\cos)} \cos(\omega_0 t) + Y^{(1,\sin)} \sin(\omega_0 t) - Y^{(3,\sin)} \sin(3\omega_0 t) \end{aligned} \quad (2.11-b)$$

$$\begin{aligned}
N &= N_{\dot{r}}\dot{r} + N_r r + N_{rrr} r^3 \\
&= N^{(1,\cos)} \cos(\omega_0 t) + N^{(1,\sin)} \sin(\omega_0 t) - N^{(3,\sin)} \sin(3\omega_0 t)
\end{aligned} \tag{2.11-c}$$

(iv) Combined drift-yaw test: this is a combined dynamic test based on the pure yaw test. A constant drift angle β_0 is added to the harmonic yawing ship, which provides an additional steady sway velocity. Based on this combined test, the coupling manoeuvring coefficients that involve both sway velocity v and yaw rate r can be obtained. The decompositions of force/moment are given by Eq. (2.13). The yaw rate has a sine function, so the sine components of force/moment are used to calculate the coupling coefficients Y_{rv} and N_{rv} . Meanwhile, the coupling coefficients Y_{vr} and N_{vr} can be extracted by either the mean force/moment components or the 2nd-order cosine force/moment components.

$$\psi = -\psi_0 \cos(\omega_0 t) - \beta_0 \tag{2.12-a}$$

$$r = r_0 \sin(\omega_0 t) = \psi_0 \omega_0 \sin(\omega_0 t) \tag{2.12-b}$$

$$\dot{r} = \dot{r}_0 \cos(\omega_0 t) = \psi_0 \omega_0^2 \cos(\omega_0 t) \tag{2.12-c}$$

$$\begin{aligned}
X &= X_* + X_{vv} v^2 + X_{rr} r^2 + X_{vr} vr \\
&= X^{(0)} + X^{(1,\sin)} \sin(\omega_0 t) - X^{(2,\cos)} \cos(2\omega_0 t)
\end{aligned} \tag{2.13-a}$$

$$\begin{aligned}
Y &= Y_{\dot{r}}\dot{r} + Y_v v + Y_{vvv} v^3 + Y_{vrr} vr^2 + Y_r r + Y_{rrr} r^3 + Y_{rvv} rv^2 \\
&= Y^{(0)} + Y^{(1,\cos)} \cos(\omega_0 t) + Y^{(1,\sin)} \sin(\omega_0 t) \\
&\quad - Y^{(2,\cos)} \cos(2\omega_0 t) - Y^{(3,\sin)} \sin(3\omega_0 t)
\end{aligned} \tag{2.13-b}$$

$$\begin{aligned}
N &= N_{\dot{r}}\dot{r} + N_v v + N_{vvv} v^3 + N_{vrr} vr^2 + N_r r + N_{rrr} r^3 + N_{rvv} rv^2 \\
&= N^{(0)} + N^{(1,\cos)} \cos(\omega_0 t) + N^{(1,\sin)} \sin(\omega_0 t) \\
&\quad - N^{(2,\cos)} \cos(2\omega_0 t) - N^{(3,\sin)} \sin(3\omega_0 t)
\end{aligned} \tag{2.13-c}$$

In a summary, the manoeuvring coefficients and their corresponding force/moment components measured from each type of PMM test are given in Table 2.1. The high-order harmonic components were not considered in this work, only the mean components or first-order harmonic components are used.

Table 2.1 Force/moment components and corresponding manoeuvring coeffs.
of each PMM tests

Type of tests	Force/moment components	Coefficients
Static drift	Mean components $X^{(0)}, Y^{(0)}, N^{(0)}$	$X^*,$ $X_{vv}, Y_v, Y_{vvv}, N_v, N_{vvv}$
Pure sway	In-phase components $Y^{(1,\sin)}, N^{(1,\sin)}$	$Y_{\dot{v}}, N_{\dot{v}}$
Pure yaw	Out-phase components $Y^{(1,\cos)}, N^{(1,\cos)}$	$Y_{\dot{r}}, N_{\dot{r}}$
	In-phase components $Y^{(1,\sin)}, N^{(1,\sin)}$	$Y_r, Y_{rrr}, N_r, N_{rrr}$
Drift-yaw	Mean components $Y^{(0)}, N^{(0)}$	Y_{vrr}, N_{vrr}
	In-phase components $X^{(1,\sin)}, Y^{(1,\sin)}, N^{(1,\sin)}$	X_{vr}, Y_{rvv}, N_{rvv}

2.3 Study outline

The KRISO Container Ship (KCS) model without appendages was considered for all the tests involved in this study. Fig. 2.4 and 2.5 present the bare hull shape and the body plan. From the viewpoint of CFD analysis, this hull has a sharp leading edge (small flare angle) and an extruded bulbous structure that is possible to induce strong vortex shedding. It also introduces a large variation of waterlines at different draft conditions, raising the concern about the nonlinearity caused by wave slopes. Meanwhile, because of the small flare angle and the high forecastle deck, it would be interesting to observe the nonlinear wave impact on the bow under ship manoeuvring motions. The stern is overhanging the free surface. The overall hull is a slender shape, with a blockage coefficient of 0.651.



Fig. 2.4 KCS bare hull

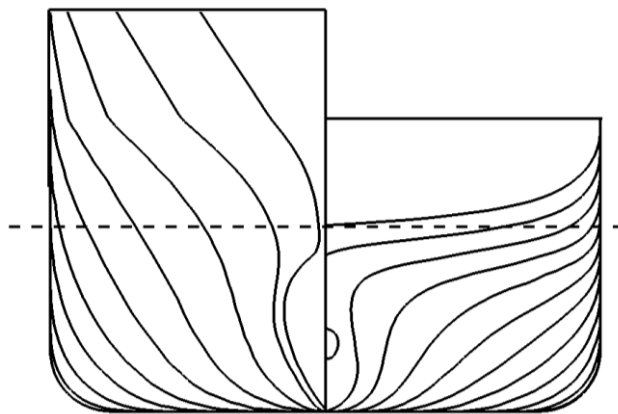


Fig. 2.5 KCS body plan

There were three different scales of the KCS model being used in this study, as listed in Table 2.2. The model scale was determined according to the experiments carried out by different research groups. The 1/85 scaled model was used to validate the KCS seakeeping tests conducted by **Stoker (2016)**, and the 1/40 scaled model was used to validate the calm-sea PMM tests conducted by **Sung and Park (2015)**. The 1/75 scaled model was selected according to the KCS turning circle tests in waves carried out by **Yasukawa et al. (2021)**. The present study used this 1/75 scaled model for the numerical PMM tests in waves. The Froude condition was reduced to 0.16 for this 1/75 scaled model, trying to match the conditions used in the turning circle experiment.

The test matrices are summarized in Tables 2.3 and 2.4. Two verification and validation (V&V) studies have been carried out systematically. The uncertainties of the time window and main discretization parameters were examined for both the PMM test and the seakeeping test. The validation tests were also conducted accordingly. The PMM tests in waves summarized in Table 2.5 were carried out based on a series of static drift tests and pure yaw tests. The effect of three wave parameters (wave frequency, wave slope, and wave direction) on the PMM tests have been examined independently, and the relationship between the wave parameters and the measured manoeuvring coefficients was observed at the final stage.

Table 2.2 Main particulars of KCS hull

Scale	1	1/40 ^[1]	1/85 ^[2]	1/75 ^[3]
L [m]	230	5.75	2.7	3.06
B [m]	32.2	0.805	0.378	0.428
T [m]	10.8	0.270	0.127	0.144
∇ [m ³]	52030	0.813	0.084	0.126
x_G [%]	-1.48	-1.48	-1.48	-1.48
C_b	0.651	0.651	0.651	0.651
KG [m]	-	0.358	0.168	0.191
I_{xx}/B	0.40	0.40	0.40	0.49
I_{yy}/L	0.250	0.250	0.250	0.250
Re	2.39×10^9	9.88×10^6	3.18×10^6	2.36×10^6
Fn	0.26	0.26	0.26	0.16
U (m/s)	24 kn	1.953	1.338	0.877
Application in this work	-	PMM test in calm sea	Seakeeping test	*PMM test in waves
<p>^[1]: Sung and Park (2015), ^[2]: Stocker (2016), ^[3]: Yasukawa et al. (2021)</p> <p>*In the experiment work^[3], this 1/75 model was used for the turning circle tests in wave.</p>				

Table 2.3 Overview of the V&V study I: PMM tests in calm sea

Model scale		1/40
Environment		calm sea
Fn		0.26
Fixed motions		roll
Verification work	Static drift test $\beta_0 = 18^\circ$	Items of uncertainty: 1) time window 2) boundary layer mesh 3) general grid resolution 4) time step
	Combined drift-yaw test $r_0' = 0.5, \beta_0 = 12^\circ$	
Validation work	Static drift test	$\beta_0 = 0^\circ \sim 18^\circ$
	Pure sway test	$\dot{v}_0' = 0.1 \sim 0.3$
	Pure yaw test	$r_0' = 0.1 \sim 0.5$
	Combined drift-yaw test	$r_0' = 0.1 \sim 0.5, \beta_0 = 0^\circ \sim 12^\circ$
Reference		Sung and Park (2015)

Table 2.4 Overview of the V&V study II: seakeeping tests

Model scale		1/85
Environment		waves
Fn		0.26
Fixed motions		sway, yaw
Verification work	Motion in head sea $\lambda/L = 1$	Items of uncertainty: 1) time window 2) general grid resolution 3) time step
Validation work	Wave frequency effect	$\lambda/L = 0.5 \sim 1.8$
	Wave direction effect	$\chi = 180^\circ \sim 0^\circ$
Reference		Stocker (2016)

Table 2.5 Overview of the study cases: PMM tests in waves

Model scale		1/75
Environment		waves
Fn		0.16
Fixed motions		roll
Test cases		Static drift test $\beta_0 = 0^\circ \sim 12^\circ$ Pure yaw test: $r' = 0.1 \sim 0.5$
Observation	Effect of wave freq.	Fixed cond': - $H/\lambda = 1/60, \chi = 180^\circ$ Variation: - $\lambda/L = 0.5, 1.0, 1.5$
	Effect of wave slope	Fixed cond': - $\lambda/L = 1.0, \chi = 180^\circ$ Variation: - $\lambda/L = 1.0$ - $H/\lambda = 1/90, 1/60, 1/30$
	Effect of wave direction	Fixed cond': - $\lambda/L = 1.0, H/\lambda = 1/60$ Variation: - $\chi = 0^\circ \sim 360^\circ$

3. Numerical Method

3.1 Basic solver

The numerical PMM tests were carried out using the *snuMHLFoam* which is a CFD package developed based on the OpenFOAM® v1912 platform. The fundamental VOF solver, *interfoam*, which is designed for two incompressible and immiscible fluids was employed. The solver was further coupled with the *waves2Foam* toolkit for solving the continuity equation and momentum equations.

$$\nabla \vec{u} = 0 \quad (3.1)$$

$$\frac{\partial(\rho \vec{u})}{\partial t} + \nabla(\rho \vec{u} \cdot \vec{u}) = -\nabla p_{\text{rgh}} - g \vec{h} \cdot \nabla \rho + \nabla(\vec{T}) + \rho \vec{f}_{\text{ext}} \quad (3.2)$$

where ρ , \vec{u} , and p are the density of the fluid, velocity, and pressure, respectively. Based on the Eqs. (3.3) and (3.4), Eq. (3.1) was derived by assuming the zero material derivative of incompressible flow. p_{rgh} is the dynamic pressure that the hydrostatic pressure $\rho g \vec{h}$ has been subtracted. \vec{h} is the height vector of volume cell in the gravitational direction. \vec{T} is the deviatoric stress tensor of incompressible flow and \vec{f}_{ext} is the external forces including gravitational force. The surface tension between the two phases was neglected.

$$\frac{\partial \rho}{\partial t} + \nabla(\rho \vec{u}) = 0 \quad (3.3)$$

$$\frac{D\rho}{Dt} = \frac{\partial\rho}{\partial t} + \vec{u} \cdot \nabla\rho = 0 \quad (3.4)$$

Based on the volume of fluid (VOF) method, the volume of fraction α that represents the fluid phase was defined by Eq. (3.5). Present work specified the phase 1 and 2 to be the air and water, respectively.

$$\alpha = \begin{cases} 0 & \text{phase 1 (air)} \\ 1 & \text{phase 2 (water)} \\ 0 \sim 1 & \text{mixture} \end{cases} \quad (3.5)$$

To overcome the numerical diffusion generated by discrete convection schemes and to main the sharpness of the VOF-based interface, the original solver applied the interface compression method and a limiter called the multidimensional universal limiter for explicit solution (MULES), as the theory described by **Zalesak (1979)** and **Deshpande et al. (2012)**. The transport equation of scalar α was given by Eq. (3.6), and the third term is the compression term. The compression velocity \vec{u}_c compresses the interface from the normal direction instead of the tangential direction, and the compression strength was 1.0 in the present study.

$$\frac{\partial\alpha}{\partial t} + \nabla(\alpha\vec{u}) + \nabla[\alpha(1-\alpha) \cdot \vec{u}_c] = 0 \quad (3.6)$$

$$\vec{u}_c = \frac{c_\alpha \cdot \nabla\alpha}{|\nabla\alpha|} \cdot \vec{u} \quad (3.7)$$

The properties of transport fluid were calculated by Eq. (3.8) and (3.9). The

term ν_t is the eddy viscosity that will be discussed in next section.

$$\rho = \alpha \rho_{water} + (1 - \alpha) \rho_{air} \quad (3.8)$$

$$\nu = \alpha \nu_{water} + (1 - \alpha) \nu_{air} + \nu_t \quad (3.9)$$

3.2 Finite volume discretization

The finite volume method (FVM) uses the integral form of the governing equations and discretizes the computational domain into finite control volumes. The surface and volume integrals are transformed into discrete algebraic relations using quadrature formulae, and then the variations of variables are approximated between the volume cells and faces to transform the algebraic relation into a system of algebraic equations.

The discrete terms of governing equations can be categorized into four mathematical terms: the transient term $\partial/\partial t$, the gradient term ∇ , the divergence term $(\nabla \cdot)$, and the Laplacian term Δ .

The transient term is handled by the implicit Euler scheme. The gradient terms are calculated by the Gauss linear scheme, and a limiter is applied to ensure that the face values obtained by extrapolating the cell values are bounded by the minimum and maximum neighbor cell values.

The divergence term $\nabla \cdot$ is selected depending on the transported quantity. The total variation diminishing (TVD) scheme with a van Leer limiter is used for the volume fraction. The linear upwind scheme is chosen for the turbulence quantities, and the central-differencing scheme is adopted for the velocity.

The Laplacian term $\nabla \cdot (\Gamma \nabla \phi)$ in the momentum equation is discretized by

combining an interpolation scheme for the diffusion coefficient Γ and a surface-normal gradient scheme for the gradient $\nabla\phi$. The linear interpolation is used to transform the diffusion coefficient from the cell to its faces. The surface-normal gradient scheme is to calculate the normal component of the gradient evaluated at the center of two neighboring grids. The central differencing scheme is used for the surface-normal gradient. To improve the accuracy of the face gradient estimated between two neighboring grids, a blending non-orthogonal correction is added to control the discrepancy caused by mesh non-orthogonality. The details of non-orthogonal correction can be found in **OpenFOAM® (2019)**.

The discrete equations are represented by a matrix system of linear algebraic equation $A\mathbf{x} = b$ and it is handled using an iterative solver. The equation for pressure p is solved using the conjugate gradient based methods, and the solution is accelerated by the preconditioner method. The equations for other variables. (e.g., velocity, turbulence, VOF) are solved using the Gauss-Seidel smoother method.

The coupling between pressure and velocity is iterated by the PIMPLE algorithm which is a combination of PISO (Pressure Implicit with Splitting of Operators) algorithm and SIMPLE (Semi-Implicit Method for Pressure Linked Equations) algorithm. Two outer iterations of the entire system of equations and two inner iterations of the pressure corrector are solved in each time step.

3.3 Turbulence model

The present study employed the k - ω SST model and the transport equations of turbulent kinetic energy k and specific dissipation ω are given as follows.

$$\frac{\partial \rho k}{\partial t} + \frac{\partial \rho u_j k}{\partial x_j} - \frac{\partial}{\partial x_j} \left[\rho (\nu + \sigma_k \nu_t) \frac{\partial k}{\partial x_j} \right] = \rho P_k - \rho \beta^* \omega k + S_k \quad (3.10)$$

$$\frac{\partial \rho \omega}{\partial t} + \frac{\partial \rho u_j \omega}{\partial x_j} - \frac{\partial}{\partial x_j} \left[\rho (\nu + \sigma_\omega \nu_t) \frac{\partial \omega}{\partial x_j} \right] = \frac{\gamma}{\nu_t} \rho G - \rho \beta \omega^2 + 2(1 - F_1) \rho \frac{\sigma_{\omega 2}}{\omega} \frac{\partial k}{\partial x_j} \frac{\partial \omega}{\partial x_j} \quad (3.11)$$

where ν and ν_t are the fluid viscosity and the eddy viscosity, respectively. S_k is the source term. P_k is the production term of turbulent kinetic energy k , and

G equals to $\nu_t \frac{\partial u_i}{\partial x_j} \left(\frac{\partial u_i}{\partial x_j} + \frac{\partial u_j}{\partial x_i} \right)$. γ , F_1 , F_{23} are blending functions and σ_k , σ_ω , $\sigma_{\omega 2}$,

β , β^* , a_1 , b_1 are model constants. S is the flow mean rate of strain.

The buoyancy sink term G_b (Devolder et al., 2017) and an additional limiter F' (Larsen and Fuhrman, 2018) were added considering the unconditionally unstable turbulence fields near the free surface (Devolder et al. (2017), Kim et al. (2017), Larsen and Fuhrman (2018)).

$$\nu_t = a_1 \frac{k}{\max(a_1 \omega, b_1 F_{23} S, F')} \quad (3.12)$$

$$G_b = -\frac{\nu_t}{\sigma_t} \frac{\partial \rho}{\partial x_j} g \quad (3.13)$$

$$F' = a_1 \lambda_2 \frac{\beta}{\beta^* \alpha} \frac{p_0}{p_\Omega \omega} \quad (3.14)$$

where $p_0 = 2\mathbf{S}:\mathbf{S}$, $p_\Omega = 2\mathbf{\Omega}:\mathbf{\Omega}$. The \mathbf{S} and $\mathbf{\Omega}$ are mean strain tensor and mean rotation rate tensor, respectively. The strength of sink term σ_t was 0.85, and the λ_2 adopted the empirical value 0.05.

3.4 Computational conditions

3.4.1 Computational domain

A moving circular domain was applied for the various PMM tests under a wave or calm-sea environment. Fig. 3.1 presents the computational domain including the free surface and four rigid boundaries. The boundary “*inlet*” surrounds the circular side of domain. The boundary “*top*” indicates the top ceiling of domain, and the boundary “*bottom*” represents the deep bottom of domain. The boundary “*hull*” was actually further divided into several sub-surfaces (port side, starboard side, deck, stern), so the highly curly and sharp edges of hull can be well meshed. The radius of the circular domain was determined by ship length L and wavelength λ . The length of the circular wave forcing zone was λ and the radius of the inner part was $(0.5L + 0.5\lambda)$. The exponential wave forcing function was applied to enforce the wave generation and to eliminate the wave reflection. The length λ was replaced to be L for the calm-sea cases. The vertical height of the computational domain is not critical for the present deep-water problems, L and $2L$ were used as the upwards height and downwards depth, respectively.

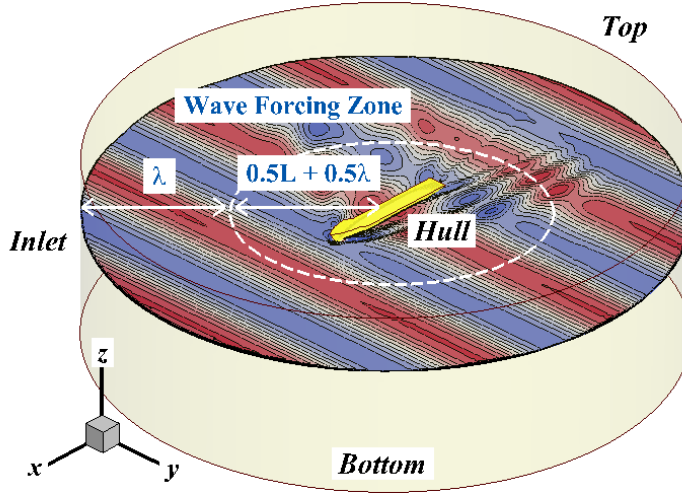


Fig. 3.1 Computational domain

To enable the ship to undergo various PMM motions in calm water or waves, the circular computational domain worked as a moving wave tank. This moving tank performs like the virtual PMM carriage, it is attached to the ship and it undergoes the prescribed planar motions. The wave-induced motions, such as heave and pitch, were achieved by deforming the local mesh near the hull.

For the numerical wave field, this study implemented the 2nd-order waves based on the *waves2foam* toolkit (Jacobsen et al., 2011). This toolkit provides an explicit function to generate and maintain the numerical waves, as Eqs. (3.15) and (3.16). The ϕ_{theory} and ϕ_{computed} indicate the theoretical values and the computed values, respectively. The calculation of forcing weight w_e involved the exponent f (to be 3.5 in this work) and the relative radius σ was specified by the radial coordinate r , the inner/outer radius (R_{inner} , R_{outer}) of the circular forcing zone. Fig. 3.2 presents the distribution of the forcing weight inside the domain.

$$\phi = (1 - w_e)\phi_{\text{theory}} + w_e\phi_{\text{computed}} \quad (3.15)$$

$$w_e = \frac{\exp \sigma^f - 1}{\exp 1 - 1} = \begin{cases} 0 & \sigma = 1 \\ 1 & \sigma = 0 \end{cases} \quad (3.16)$$

$$\sigma = \frac{r - R_{\text{inner}}}{R_{\text{outer}} - R_{\text{inner}}} \quad (3.17)$$

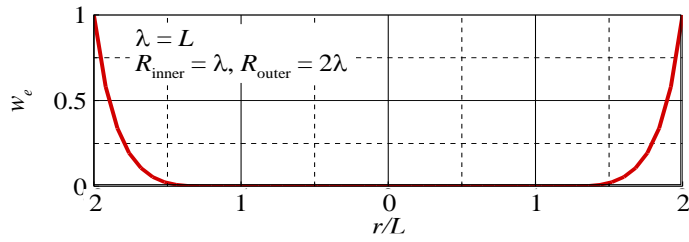


Fig. 3.2 Distribution of exponential wave forcing weights ($\lambda = L$)

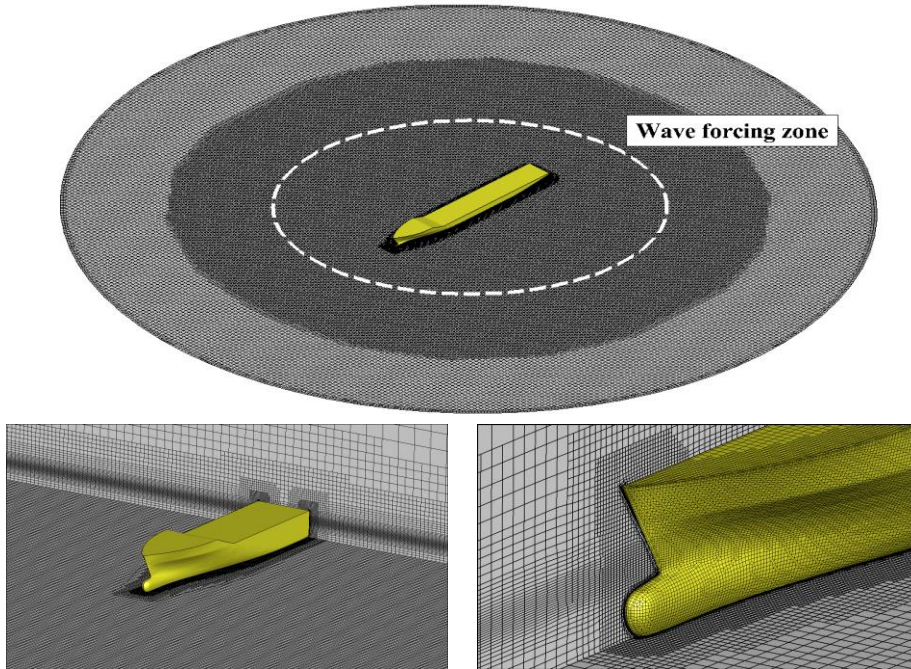


Fig. 3.3 Unstructured mesh system

The unstructured mesh system shown in Fig. 3.3 was considered for the present works, and local refinement was applied near the free surface and ship body. The refinement near the free surface was extended to the wave forcing zone in order to avoid the wave diffusion caused by the transition of grid size. The same resolution was used in longitudinal and transverse directions, namely $\Delta x = \Delta y$. The selection of mesh resolution and the corresponding numerical uncertainties will be introduced in Chapter 4.

3.4.2 Boundary conditions

Table 3.1 Boundary conditions of flow fields

Boundary	Fields			
	Volume fraction	Velocity	Pressure	Turbulence (k, ω, ν_t)
Top	zero-grad.	zero-grad.	Fixed value ($p_t = 0$)	zero-grad.
Inlet	zero-grad.	zero-grad.	zero-grad.	zero-grad.
Bottom	zero-grad.	zero-grad.	zero-grad.	zero-grad.
Hull	zero-grad.	Fixed value ($\mathbf{u} = \mathbf{u}_0$)	zero-grad.	Wall func.

There were two types of boundary conditions applied in the present computational domain. One was the “zero-gradient” condition, which is a Neumann-type condition that specifies the zero normal gradients of values at the boundary. Another one was the “fixed value” condition, which is a Dirichlet-type condition that specifies a fixed value at the boundary. Table 3.1 has given the conditions of each domain boundary for the computational variables. The “zero-gradient” condition was more widely applied, while the “top” boundary used a zero total pressure condition. For the velocity condition

of the “hull” boundary, it used a no-slip condition and the velocity equals the prescribed motion velocity u_0 that should be updated at every time step.

Meanwhile, the wall functions that are based on both the Newmann condition and the Dirichlet condition were applied for the turbulence fields (k , ω , ν_t) near the hull. The turbulent kinetic energy k used a zero-gradient condition. The specific dissipation ω and the eddy viscosity ν_t used the fixed-value condition based on stepwise blending functions, as given by Eq. (3.18) and (3.19). The empirical constants β_1 , C_μ , κ , and E used the model’s default values 5.5, 0.09, 0.41, 9.793, respectively. The dimensionless wall distance y^+ and the estimated value y_{lam}^+ were used to blend the wall functions. Eq. (3.20) and (3.21) give the calculation of y^+ , y is the distance to the nearest wall, ν is the kinematic viscosity. u^* is the frictional velocity determined by wall shear stress τ_w . The estimated wall distance y_{lam}^+ is interpreted as the intersection between the viscous layer and log layer.

$$\omega = \begin{cases} \frac{6\nu}{\beta_1 y^2} & \text{in viscous layer, } y^+ < y_{\text{lam}}^+ \\ \frac{\sqrt{k}}{(C_\mu)^{0.25} \kappa y} & \text{in log layer, } y^+ > y_{\text{lam}}^+ \end{cases} \quad (3.18)$$

$$\nu_t = \begin{cases} 0 & \text{in viscous layer, } y^+ < y_{\text{lam}}^+ \\ \nu \left(\frac{\kappa y^+}{\ln(\max[Ey^+, 1])} - 1 \right) & \text{in log layer, } y^+ > y_{\text{lam}}^+ \end{cases} \quad (3.19)$$

$$y^+ = \frac{u^* y}{\nu} \quad (3.20)$$

$$u^* = \sqrt{\frac{\tau_w}{\rho}} \quad (3.21)$$

3.4.3 Computational cost

Given the diversity of PMM tests, it is necessary to understand the overall computational cost for obtaining a complete set of hull manoeuvring coefficients. In particular, the computational burden would be significantly increased by further considering various wave conditions.

Table 3.2 listed the main features of the two computational resources used for the present numerical PMM tests. The cluster is composed of 20 nodes and there are 4 or 6 cores on each node. The workstation has a single thread with 52 cores. The same MPI platform was built for two machines, and the workstation has more updated processors and larger RAM size.

Table 3.2 Main features of two computational resources

Machine	Cluster	Workstations
RAM	15G	282G
CPU	Intel E3-1230 (2011), 3.4GHz	Intel Gold 6230R (2020), 2.1GHz
Cores	100	52
Cores distribution	4×10 + 6×10 (10 + 10 nodes)	Single thread
MPI platform	Open MPI 1.10.7	Open MPI 1.10.7

Fig. 3.4 presents the scalability of two machines. The speedup in parallel computation was calculated by $t(1)/t(N)$, where $t(1)$ is the computational time by a single processor, and $t(N)$ is the computational time by N processors. The ideal speedup should be equal to the number of processors.

It must be emphasized that the scalability shown in Fig. 3.4 cannot be generalized. The scalability is not purely determined by the quality of the processors or the memory card. There are more factors (e.g., the optimized combination of hardware, the parallelization and communication algorithm,

and the decomposition of mesh system) that can affect the scalability.

Based on 100 cores of the cluster shown above, Table 3.3 has estimated the computational cost for a series of PMM tests that were conducted under calm-sea or wave conditions. The static drift test requires 20 seconds of test time, and the harmonic PMM tests require 40 seconds which is nearly 2-3 harmonic cycles. The static drift test was less sensitive to the time step so the time step can be relatively large. The time step of harmonic PMM tests was determined by the harmonic period T_{PMM} . The tests involving waves used the time step based on the wave encountering speed U_e and the grid size near waves (Δx). The uncertainties of the mesh resolution and time step will be discussed in Chapter 4. By the parallel computations, a complete set of hull manoeuvring coefficients was expected to be obtained within 18 days. The time can be reduced to approximately 12 days because it is not necessary to run all the combined drift-yaw tests. The total number of combined tests can be reduced by half. For the tests in waves that neither the combined drift-yaw test nor the tests for added mass coefficients were considered, it would take 10 days to complete a series of the test under single wave conditions. The computational cost is multiplied depending on the considered wave parameters.

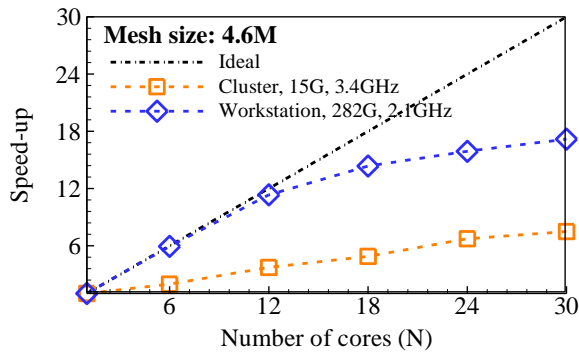


Fig. 3.4 Scalability of present computational machines

Table 3.3 Estimated computational cost based on 100 cluster cores

	Environment		calm sea				single wave condition	
	Test type	static drift	pure sway	pure yaw	*drift-yaw	static drift	pure yaw	
Test	Test range	$\beta_0 = 0 \sim 18^\circ$	$\psi' = 0.05 \sim 0.3$	$r_0' = 0.1 \sim 0.5$	$r_0' = 0.1 \sim 0.5$ $\beta_0 = 3^\circ \sim 18^\circ$	$\beta_0 = 0 \sim 18^\circ$	$r_0' = 0.1 \sim 0.5$	
	# of test cases	7	5	5	*30	7	5	
	Test time per case	20s	40s (2-3 cycles)	40s (2-3 cycles)	40s (2-3 cycles)	20s	40s (2-3 cycles)	
Numerical model	Mesh	3.9 M				4.6 M		
	Time step	$\Delta t = 0.01s$	$T_{P_{MAX}}/\Delta t = 2800$ ($\Delta t = 0.005s$)			$U_e \cdot \Delta t/\Delta x = 0.20$ ($\Delta t = 0.002s$)		
	Algorithm	2 inner iterations; 2 outer iterations; 3 VOF sub-steps						
Parallel computation	# of cores per case	12	20	20	20	12	20	
	# of parallel	7	5	5	5	7	5	
	Cost for single case	18 hr	51 hr	51 hr	51 hr	92 hr	140 hr	
	Overall cost	$18 \times 1 + 51 \times 1 + 51 \times 1 + 51 \times 6$ $= 426 \text{ hr}$ (*18 days)					$92 \times 1 + 140 \times 1$ $= 232 \text{ hr}$ (10 days)	

*It is not necessary to run all the combined drift-yaw tests, the # of test cases can be reduced to 15, and the overall cost can be reduced to approximately 12 days.

4. Numerical Uncertainties

The numerical uncertainties of the present computational model were examined for both the PMM test in calm sea and the seakeeping tests. Three basic types of tests have been selected: (1) the static drift test ($\beta_0=18^\circ$) that the large drift condition can induce strong vortex shedding, (2) the combined drift-yaw test ($r_0'=0.5$, $\beta_0=18^\circ$) which involves the dynamic PMM motion pattern and the combined motion condition, (3) the seakeeping test in head waves ($\lambda/L=1.0$, $H/\lambda=1/60$) that involves the numerical wave field and the dynamic interaction between the hull and the waves.

The three aspects of the numerical computation have been examined: (1) the time window which is applied for data analysis, (2) the boundary mesh resolution that mainly affects the surface y^+ field for the viscous regime, (3) the two general discretization parameters, grid size and time step.

4.1 Procedure of uncertainty estimation

The uncertainty of the time window was estimated based on the running Fourier transform analysis which is used to extract the harmonic force/moment components of dynamic tests. For the mean force/moment components of static tests, this running Fourier transform analysis equals the running average analysis. The uncertainty of time window was specified to be the difference between the maximum and minimum values obtained by the running analysis.

The uncertainty of the discrete parameters (e.g. mesh size, boundary layer thickness, and time step) was estimated based on the flowchart summarized in Fig. 4.1. It has combined the several methods of uncertainty estimation

recommended by ITTC-7.5-03-01-01 (2021).

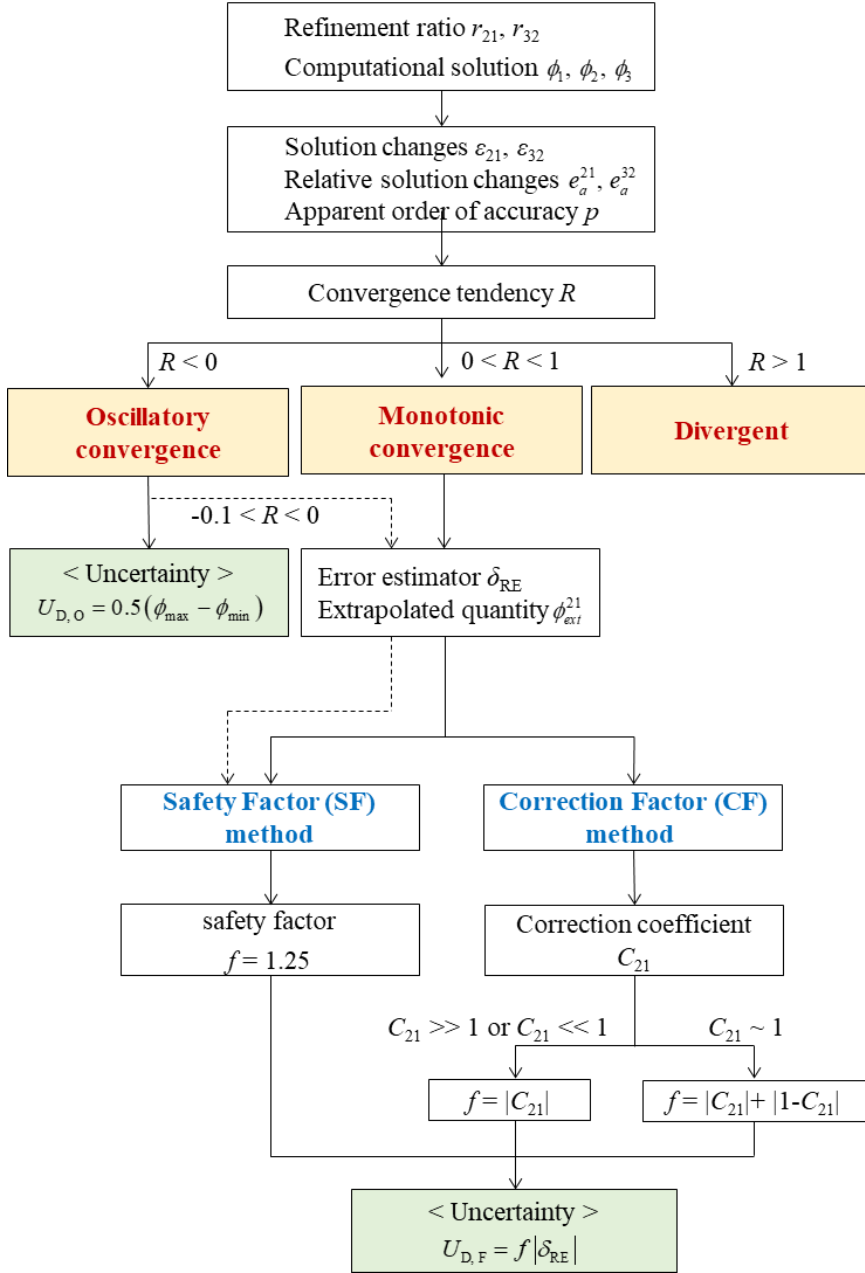


Fig. 4.1 Flowchart of uncertainty estimation

As illustrated by Fig. 4.1, three solutions ϕ_1 , ϕ_2 , ϕ_3 that are obtained based on three different discrete resolutions (mesh resolution or time step resolution) are necessary for estimating the relative changes and apparent order p . The refinement factor r_{21} and r_{32} are calculated by $r_{21} = h_2/h_1$, $r_{32} = h_3/h_2$, where the indices 1, 2, 3 which represent the fine resolution, medium resolution, and coarse resolution, respectively. The h_i is the representative item, such as grid size Δx or time step Δt .

The solution changes are specified by $\varepsilon_{21} = \phi_2 - \phi_1$, $\varepsilon_{32} = \phi_3 - \phi_2$ and the relative solution changes are calculated by $e_a^{21} = |(\phi_1 - \phi_2)/\phi_1|$ and $e_a^{32} = |(\phi_2 - \phi_3)/\phi_2|$. The apparent order p stands for the theoretical order of the numerical solution, it is evaluated iteratively through Eqs. (4.2) and (4.3) when the refinement factor is not constant.

$$\varepsilon_i = \phi_i - \phi_{\text{exact}} = c \cdot h_i^p + \text{H.O.T} \quad (4.1)$$

$$p = \frac{|\ln|\varepsilon_{32}/\varepsilon_{21}| + q(p)|}{\ln(r_{21})} \quad (4.2)$$

$$q(p) = \ln\left(\frac{r_{21}^p - 1}{r_{32}^p - 1}\right) \quad (4.3)$$

$$R = \varepsilon_{21}/\varepsilon_{32} \quad (4.4)$$

For the oscillatory convergence case that the convergence ratio R is negative, the oscillatory uncertainty $U_{D,O}$ is estimated by the range between the maximum solution ϕ_{max} and the minimum solution ϕ_{min} , as Eq. (4.5).

$$U_{D,O} = 0.5(\phi_{\text{max}} - \phi_{\text{min}}) \quad (4.5)$$

For the monotonic convergence case that $0 < R < 1$, the methods that are based on the generalized Richardson extrapolation (**Roache (1998)** and **Celik et al. (2004)**) were considered. The extrapolated value ϕ_{ext}^{21} represents the expected convergent solution. The estimated error δ_{RE} is estimated for the fine case, and it is used to calculate the numerical uncertainty with a specified factor f .

$$\delta_{RE} = \frac{e_a^{21}}{r_{21}^p - 1} \quad (4.6)$$

$$\phi_{ext}^{21} = \frac{r_{21}^p \phi_1 - \phi_2}{r_{21}^p - 1} \quad (4.7)$$

$$U_{D,F} = f |\delta_{RE}| \quad (4.8)$$

To determine the factor f , one of the methods is the correction factor method which was proposed by **Stern et al (1999)**. This method introduces a correction coefficient C_{21} which is interpreted as the distance between the numerical solutions and the asymptotic line. It was proposed under an asymptotic assumption so it can only be used for the monotonic convergent case. The variable p_{est} in Eq. (4.9) is a theoretical value that equals the order of numerical scheme ($p_{est} = 2$ in this study).

$$C_{21} = \frac{r_{21}^p - 1}{r_{21}^{p_{est}} - 1} \quad (4.9)$$

Another method to determine the factor f is the safety factor (SF) method (**Roache, 1998; Celik et al. 2004**), which is also called the Grid Convergence Index (GCI) method or the Factor of Safety method. This method chooses an

empirical value $f = 1.25$ based on extensive CFD experience. This SF method can be applied to both monotonic and oscillatory convergent cases since the factor f is an empirical value. However, this safety factor method can lost its reliability when the oscillation of solutions is not mild. Fig. 4.2 provides an example on the behavior of SF method, the mean sway force and the 1st-order sine component of surge force of combined drift-yaw test are involved. The sway force $Y^{(0)}$ gradually convergent with a reasonable extrapolated value, although the slight oscillation convergence exists. By comparison, the surge force $X^{(1,\sin)}$ that shows a considerable oscillation generates a unreasonable extrapolated value. Therefore, the safety factor method is only considered for the convergence tendency $R > -0.1$, as marked in the flowchart of Fig. 4.1.

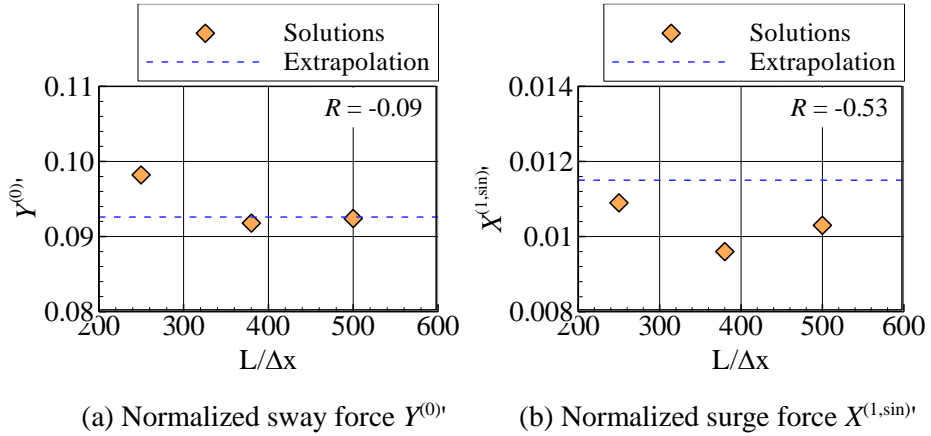


Fig. 4.2 Example of the grid convergence test for combined drift-yaw test

$$(r_0' = 0.5, \beta_0 = 12^\circ)$$

4.2 Case I: PMM test in calm sea

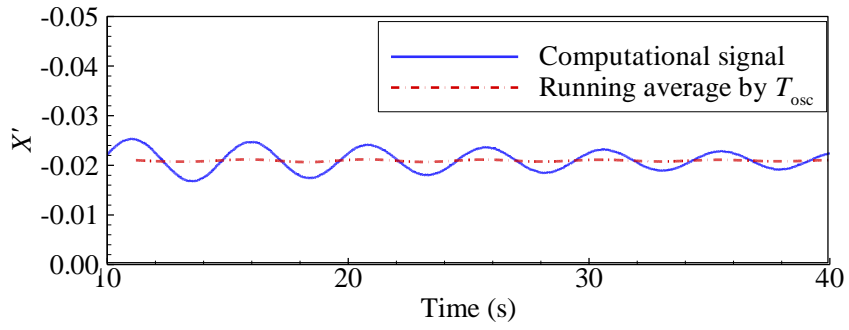
This series of tests was carried out using the 1/40 scaled KCS model listed in the previous Table 2.2. Considering the diverse motion patterns involved in the PMM tests, the numerical uncertainties were examined for both a static drift test with the large drift condition and a combined drift-yaw test with the highly coupling condition.

4.2.1 Uncertainty of time window

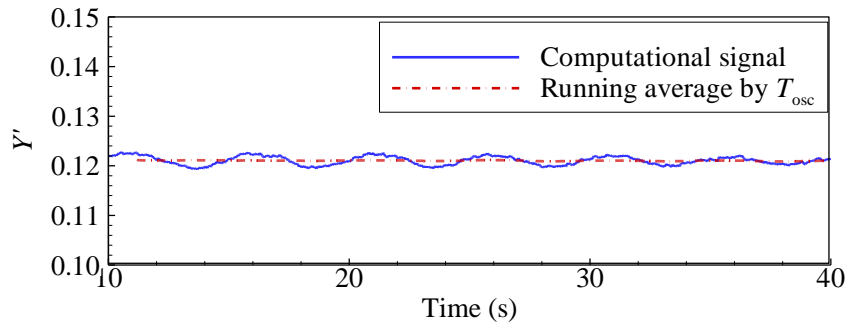
Unlike the double-body model in which the dynamic interaction between the body motion and the free surface is not considered, the free surface model involving the dynamic interaction always introduces an oscillation to the computational signals. This oscillation is induced by the transient stage of initial ship motion, and it is also influenced by the numerical oscillation of the computational model. This oscillation can affect the data analysis which is based on a selected time window. It is possible to totally damp the undesired oscillation of the computational signals, but the simulation time might be too long and unnecessary. Therefore, it is necessary to quantify the uncertainty of the time window.

A running Fourier transform analysis was applied to the computational signals and to obtain the Fourier components of interest. The uncertainty U_{RA} was calculated by the maximum value RA_{\max} and the minimum value RA_{\min} of the running analysis, as given by Eq. (4.10).

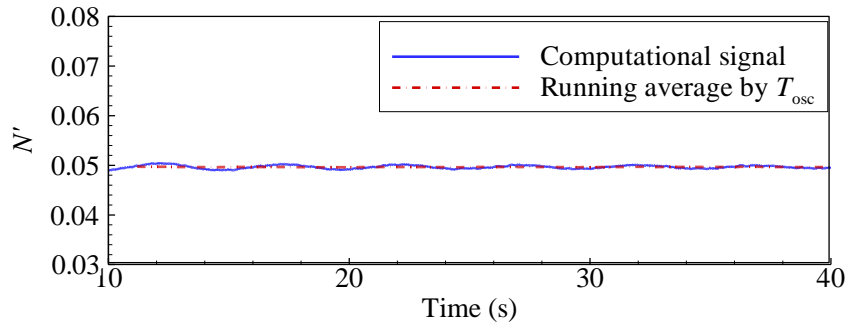
$$U_{RA} = 0.5 |RA_{\max} - RA_{\min}| \quad (4.10)$$



(a) Normalized surge force X'



(b) Normalized sway force Y'



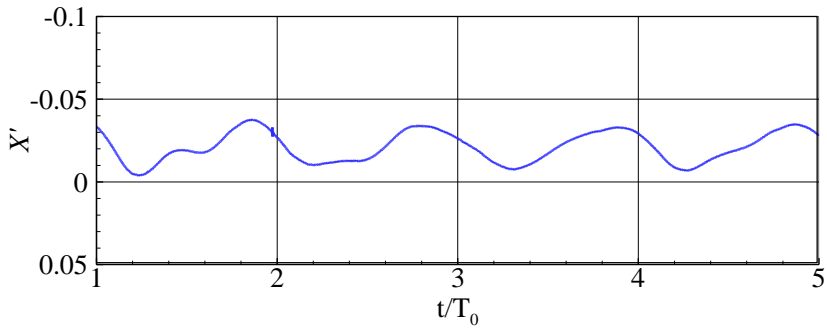
(c) Normalized yaw moment N'

Fig. 4.3 Force/moment signals of static drift test, $\beta_0 = 18^\circ$

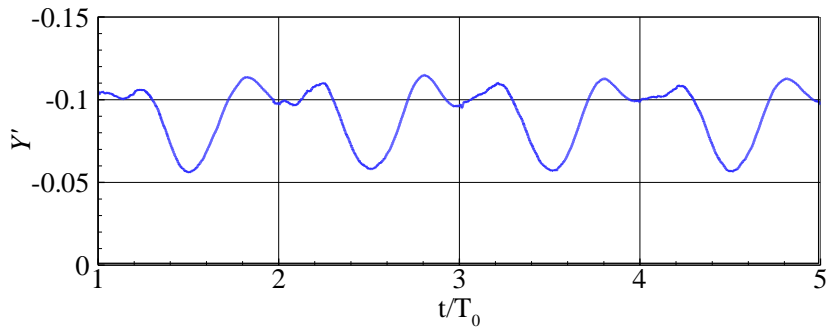
Fig. 4.3 presents the computational signals of the static drift test, including the surge force, sway force, and yaw moment. The ideal force signals of this static test should be steady, while the oscillation as discussed before can be observed in these force signals. The oscillation has a period of around 4.95s. This oscillation period (T_{osc}) is determined by the body Fn condition, the mesh structure, and the computational domain; meanwhile, a slight descending tendency can be observed on the oscillation. To perform the running analysis, the initial period of 10s was discarded due to the strong transition phenomenon at the initial towing stage, and a running average with the interval of $2T_{osc}$ was adopted. The analyzed results are given in Table 4.1, which shows very small uncertainties for both the body attitudes and body forces. Positive sinkage means the downward sink, and positive trim means the bow-up. The uncertainties are also acceptable when the interval of running analysis changes to be T_{osc} or higher than $2T_{osc}$. Therefore, the key to the time-window uncertainty is the period of the undesired oscillation.

Table 4.1 Time window uncertainty of static drift test, $\beta_0=18^\circ$

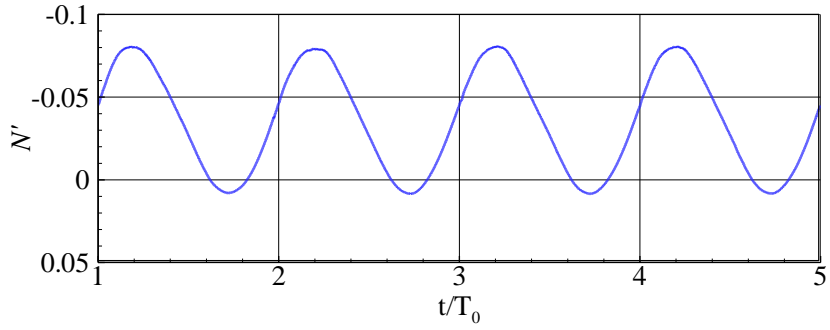
	Sinkage (m)	Trim ($^\circ$)	$X^{(0)'}$	$Y^{(0)'}$	$N^{(0)'}$
RA_{min}	-0.0289	0.3248	-0.0208	0.1210	0.0496
RA_{max}	-0.0290	0.3305	-0.0211	0.1212	0.0497
RA_{mean}	-0.0290	0.3277	-0.0210	0.1211	0.0497
U_{RA} (% RA_{mean})	0.2%	0.9%	0.7%	0.1%	0.1%
*Fixed condition: $L/\Delta x = 380$, $L/\Delta n = 10000$, $1/\Delta t = 200$					



(a) Normalized surge force X'



(b) Normalized sway force Y'



(c) Normalized yaw moment N'

Fig. 4.4 Force/moment signals of combined drift-yaw test, $r_0'=0.5$, $\beta_0=12^\circ$

Fig. 4.4 presents the computational signals of the combined drift-yaw test, including the surge force, sway force, and yaw moment. The period of the harmonic motion is T_0 . The ideal force/moment signals of this dynamic PMM test should be periodical and be composed of several harmonic components, while the periodical behavior can be influenced by the numerical oscillation. Same with the static drift test shown in Fig. 4.3, the oscillation period T_{osc} is also around 4.95s. To perform the running Fourier transform analysis, the initial first period of PMM motion was discarded due to the initial transition. The interval of running analysis is $2T_0$ and the analysis results are summarized in Table 4.2. The results include the harmonic components $X^{(1,sin)}$, $Y^{(1,cos)}$, and $N^{(1,sin)}$. The mean force components show quite small uncertainties, and relatively high uncertainties are found in the harmonic components. This is caused by the interference between the periodical PMM motion and the periodical numerical oscillation. The yaw moment has a large magnitude so the effect of numerical oscillation becomes negligible.

Table 4.2 The time window uncertainty of drift-yaw test, $r_0'=0.5$, $\beta_0=12^\circ$

	$X^{(0)'}$	$Y^{(0)'}$	$N^{(0)'}$	$X^{(1,sin)'}$	$Y^{(1,cos)'}$	$N^{(1,sin)'}$
RA_{min}	-0.0210	-0.0917	-0.0354	0.0109	-0.0200	-0.0428
RA_{max}	-0.0212	-0.0919	-0.0355	0.0113	-0.0206	-0.0429
RA_{mean}	-0.0210	-0.0918	-0.0354	0.0111	-0.0203	-0.0428
U_{RA} (% R_{mean})	0.5%	0.1%	0.2%	1.7%	1.5%	0.1%
*Fixed cond't: $L/\Delta x = 380$, $L/\Delta n = 10000$, $T_0/\Delta t = 2236$						

4.2.2 Uncertainty of boundary layer mesh

The mesh near the hull surface determines the y^+ field, and it affects the near wall field predicted by the computational model. The boundary layer mesh (also called the near-wall mesh or others) is composed of several layers of very thin grids, as described in Fig. 4.5. The thinnest grid locates at the boundary, and the thinness of grids expands along the normal direction. In the current work, eight layers of grids were considered, and the expansion ratio was 1.15. The Δx indicates the size of the uniform grids distributed around the hull, and the Δx is usually much larger than the thinness of boundary layer grids.

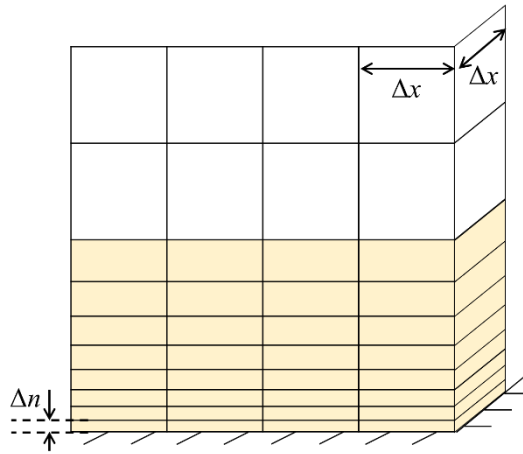
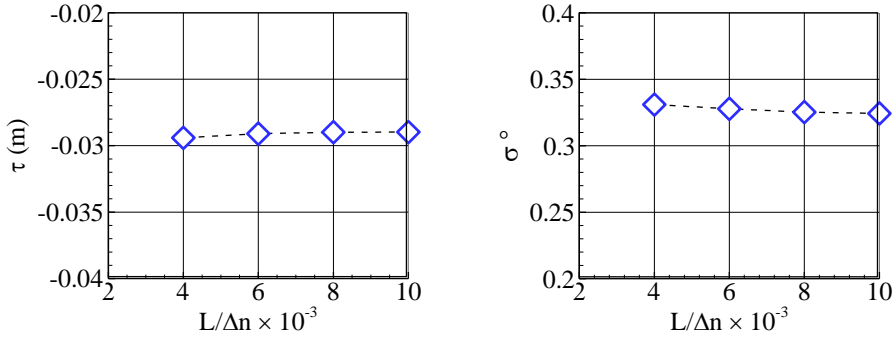
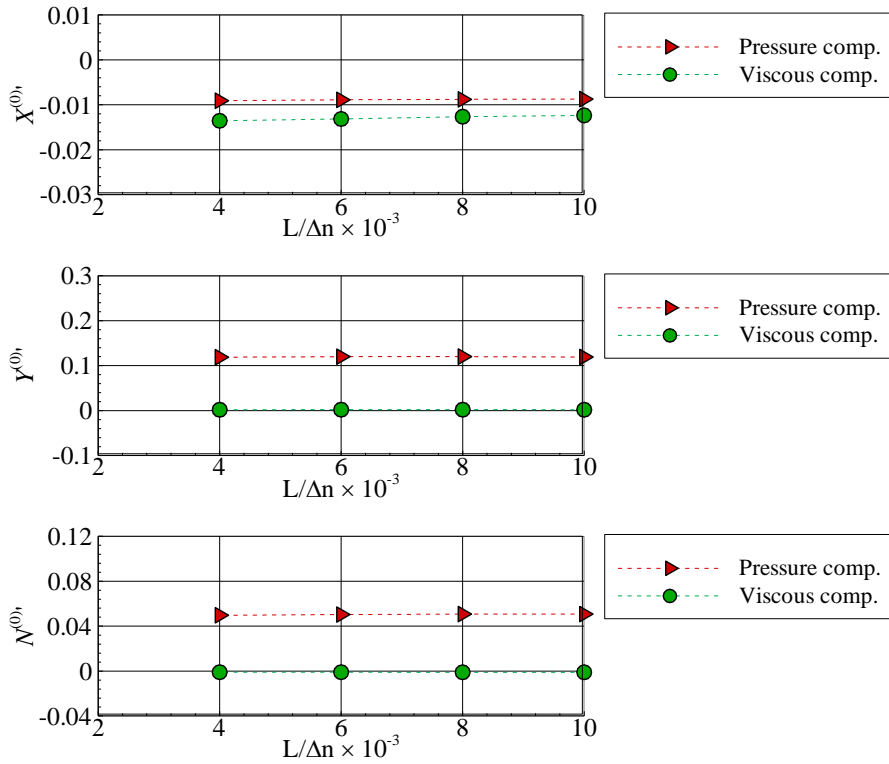


Fig. 4.5 Mesh structure near hull surface
(Dark color: boundary layer mesh)

Fig. 4.6 presents the convergence test for the static drift test. Fig. 4.6(a) contains the ship sinkage and trim, and Fig. 4.6(b) contains pressure/viscous components of the surge force, sway force, and yaw moment.



(a) Sinkage τ and trim σ



(b) Normalized force and moment components $X^{(0)}$, $Y^{(0)}$, $N^{(0)}$

Fig. 4.6 Convergence test of boundary mesh resolution, $\beta_0=18^\circ$

(fixed cond': $L/\Delta x=380$, $1/\Delta t=200$)

The body sinkage and trim have shown a convergent tendency as the increasing resolution of boundary layer mesh. The resolution of boundary layer mesh is presented by $L/\Delta n$, where L is ship length and Δn is the thickness of the first near-wall grid. It can be observed that the ship has a reduced sinkage and trim when the boundary mesh is of high resolution. This is caused by the behavior of surge force shown in Fig. 4.6(b). The surge force also has a decreasing tendency with respect to the resolution $L/\Delta n$, and this is mainly contributed by the viscous effect. By comparison, the sway force and the yaw moment are almost independent of the resolution $L/\Delta n$ because these force/moment are determined by the pressure acting on the ship lateral surface. In another word, the viscous effect mainly contributes to the ship surge force.

Table 4.3 has given the numerical uncertainties following the flowchart of Fig. 4.1. Three solutions based on different resolutions are provided, and the relative changes and the convergence ratio are estimated. The term “MT” indicates monotonic convergence, and the term “OSC” means oscillatory convergence. The uncertainties were given with respect to the solution (ϕ_1) of the most refined condition. The oscillatory uncertainty was estimated only for the “OSC” case, and the correction factor (CF) based uncertainty was estimated only for the “MT” case. The safety factor (SF) based uncertainty was also added for the cases $R > -0.1$, and the extrapolated solution based on the Richardson extrapolation was shown in a percentage format.

It can be observed from Table 4.3 that only the surge force shows a relatively high uncertainty. This is caused by the viscous effect as discussed in Fig. 4.6(b), while the uncertainty 5% ~ 6% is in an acceptable range.

Table 4.3 Uncertainty of the boundary mesh resolution for static drift test, $\beta_0 = 18^\circ$ (fixed: $L/\Delta x = 380$, $1/\Delta t = 200$)

	Sinkage (m)	Trim ($^\circ$)	Surge force $X^{(0)}$,	Sway force $Y^{(0)}$,	Yaw mom. $N^{(0)}$,
Boundary mesh resol. $L/\Delta n_1$	10000	10000	10000	10000	10000
Boundary mesh resol. $L/\Delta n_2$	8000	8000	8000	8000	8000
Boundary mesh resol. $L/\Delta n_3$	6000	6000	6000	6000	6000
Solution ϕ_1	-2.90E-02	3.24E-01	-2.11E-02	1.21E-01	4.97E-02
Solution ϕ_2	-2.90E-02	3.25E-01	-2.14E-02	1.22E-01	4.97E-02
Solution ϕ_3	-2.91E-02	3.28E-01	-2.20E-02	1.22E-01	4.93E-02
ε_{21}	-3.24E-06	1.01E-03	-3.44E-04	9.82E-04	1.94E-05
ε_{32}	-1.18E-04	2.40E-03	-6.02E-04	-8.32E-05	-4.06E-04
Convergence ratio R	0.03	0.42	0.57	-11.8	-0.05
Convergence tendency	MT	MT	MT	OSC	OSC
Oscillatory uncertainty (% ϕ_1)	-	-	-	0.41%	0.41%
CF-based uncertainty (% ϕ_1)	0.04%	0.67%	4.77%	-	-
SF-based uncertainty (% ϕ_1)	0.00%	0.55%	6.05%	-	0.00%
Extrapolated solution (% ϕ_1)	100%	100%	95%	-	100%

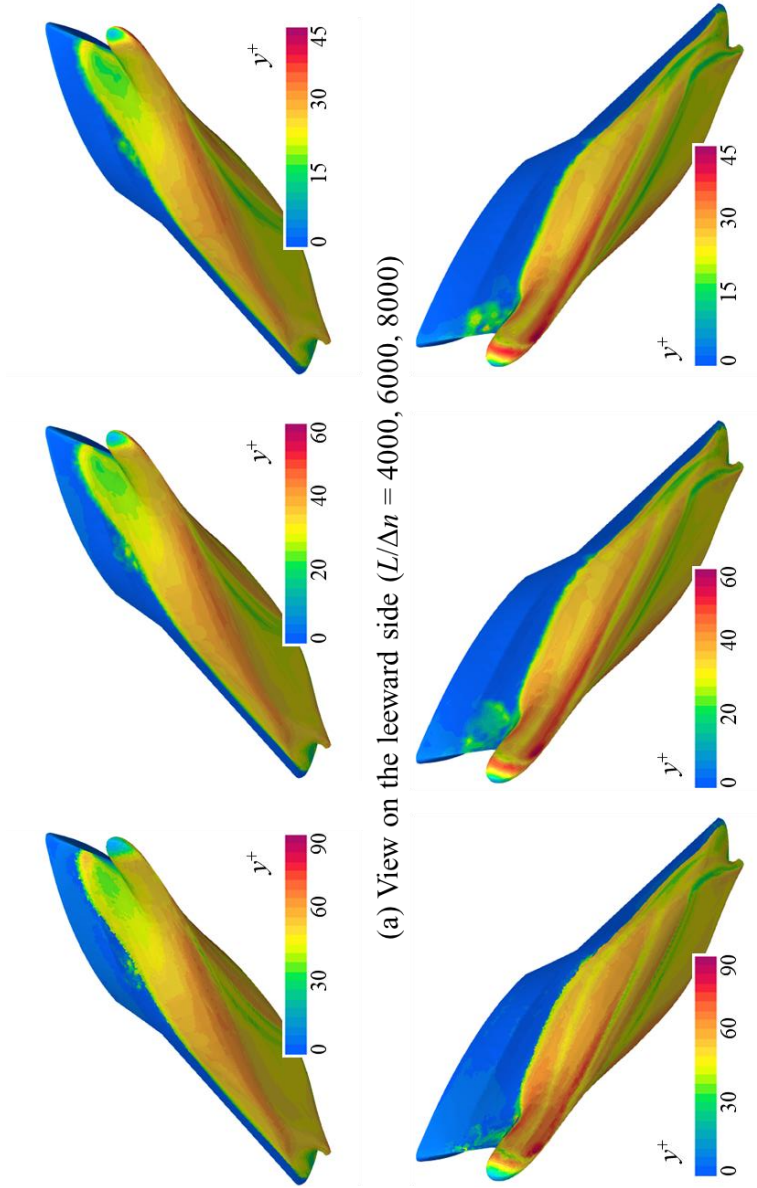
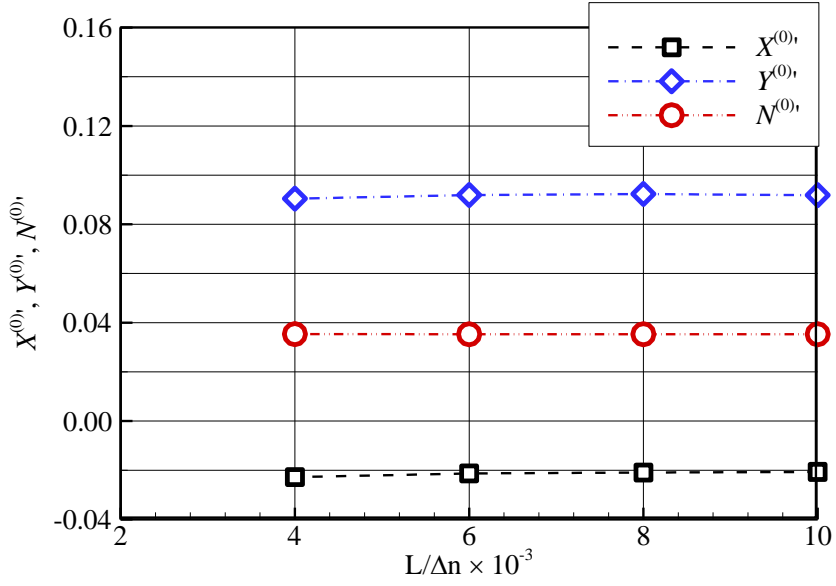


Fig. 4.7 Surface y^+ field of static drift test, $\beta_0=18^\circ$

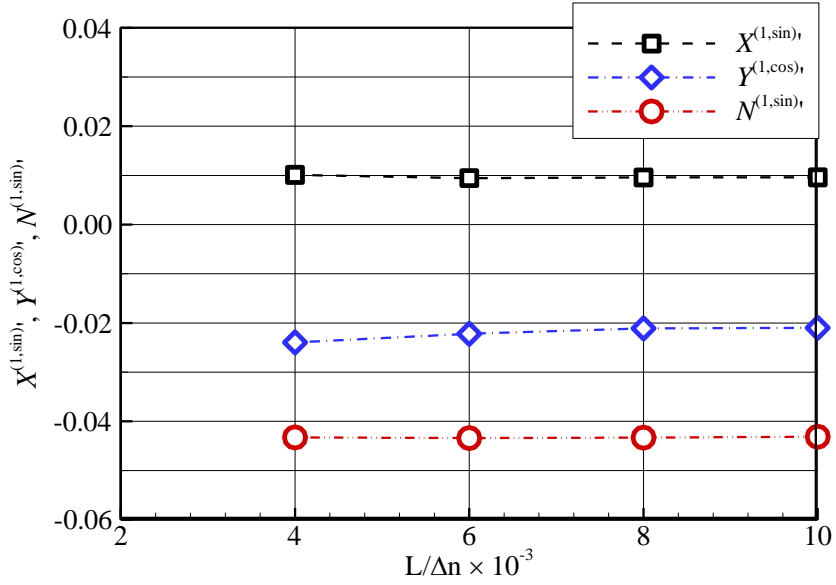
Based on the different resolutions of boundary layer mesh, the hull surface distributions of the y^+ field are compared in Fig. 4.7. The similar contours of y^+ are observed, while the legend proportionally changes with the resolution of $L/\Delta n$. The high y^+ value is mainly observed near the bow, especially beneath of bulbous bow where the strong bow vortex occurs and the wall shear stress is large. Near the bilge where bilge vortices are induced, the y^+ value is also found to be noticeable. For the resolution of $L/\Delta n = 10000$ that the numerical convergence is almost achieved, the y^+ value is about $30 \sim 40$ near the bulbous bow.

Fig. 4.8 shows the convergence test of boundary mesh resolution for the combined drift-yaw test. Similar to the phenomenon observed from the static drift test, the mean sway force and mean yaw moment are almost insensitive to the near-wall resolution because they have a large magnitude being dominated by the pressure on the lateral side. By comparison, the harmonic components of surge force and sway force show a gradually convergent tendency.

The numerical uncertainties are given in Table 4.4. The different force components have shown different convergent tendencies. The mean sway force and mean yaw moment are already convergent so the three solutions oscillate in a very small range. The surge force still has a monotonic convergence caused by the viscous effect. The yaw moment shows a convergence ratio higher than 1, but the three solutions are actually already convergent, as indicated by the SF-based uncertainty and the extrapolated solution.



(a) Mean force/moment component



(b) Harmonic force/moment component

Fig. 4.8 Convergence test of boundary mesh resolution, $r_0'=0.5$, $\beta_0=12^\circ$
(fixed cond': $L/\Delta x = 380$, $T_0/\Delta t = 2236$)

Table 4.4 Uncertainty of the boundary mesh resol. for drift-yaw test, $r_0' = 0.5$, $\beta_0 = 12^\circ$ (fixed: $L/\Delta x = 380$, $1/\Delta t = 200$)

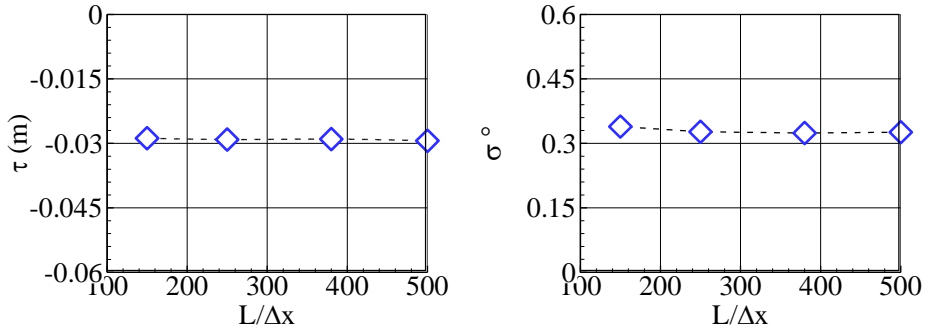
	Surge force $X^{(0)'}'$	Sway force $Y^{(0)'}'$	Yaw mom. $N^{(0)'}'$	Surge force $X^{(1,\sin)'}'$	Sway force $Y^{(1,\cos)'}'$	Yaw mom. $N^{(1,\sin)'}'$
Boundary mesh resol. $L/\Delta n_1$	10000	10000	10000	10000	10000	10000
Boundary mesh resol. $L/\Delta n_2$	8000	8000	8000	8000	8000	8000
Boundary mesh resol. $L/\Delta n_3$	6000	6000	6000	6000	6000	6000
Solution ϕ_1	-2.07E-02	9.18E-02	3.53E-02	9.60E-03	-2.10E-02	-4.31E-02
Solution ϕ_2	-2.09E-02	9.23E-02	3.53E-02	9.59E-03	-2.11E-02	-4.33E-02
Solution ϕ_3	-2.13E-02	9.19E-02	3.53E-02	9.44E-03	-2.22E-02	-4.34E-02
ε_{21}	4.78E-04	4.78E-04	7.22E-06	-1.19E-05	-1.20E-04	-1.80E-04
ε_{32}	-4.16E-04	-4.16E-04	-2.14E-05	-1.52E-04	-1.09E-03	-9.56E-05
Convergence ratio R	0.62	-1.15	-0.34	0.08	0.11	1.88
Convergence tendency	MT	OSC	OSC	MT	MT	Div
Oscillatory uncertainty (% ϕ_1)	-	0.26%	0.03%	-	-	-
CF-based uncertainty (% ϕ_1)	5.11%	-	-	0.42%	1.89%	1.26%
SF-based uncertainty (% ϕ_1)	6.46%	-	0.02%	0.03%	0.17%	0.27%
Extrapolated solution (% ϕ_1)	95%	-	100%	100%	100%	100%

4.2.3 Uncertainty of discretization parameter

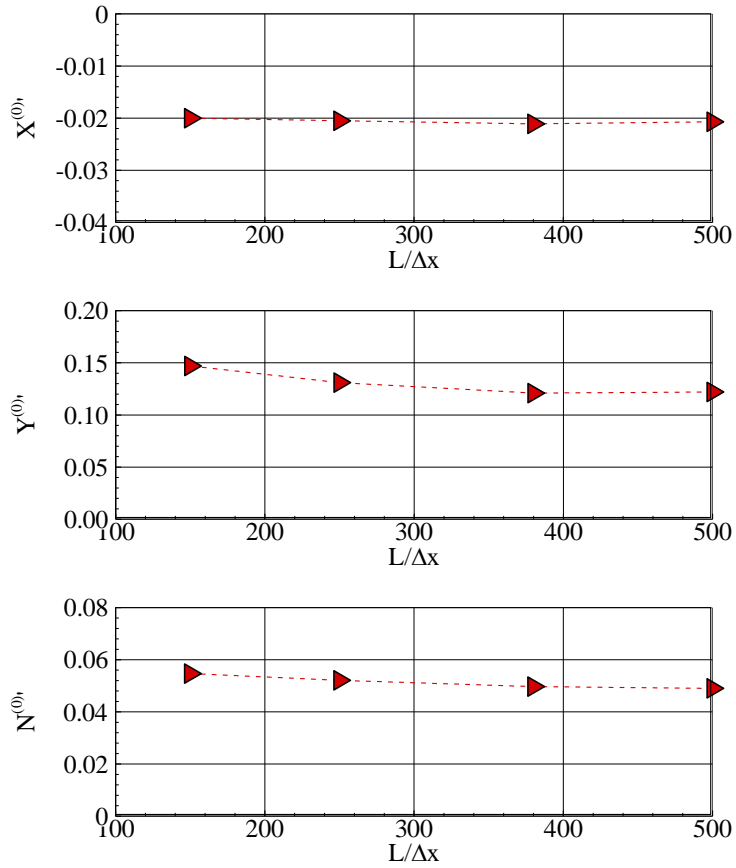
Two discretization parameters, grid size and time step, will be investigated in this section. In the previous section on the boundary layer mesh, only the mesh resolution near the hull surface changes for the uncertainty study. In this section, the boundary mesh resolution is fixed to be $L/\Delta n = 10000$, and the resolution of entire mesh system will be changed for the uncertainty estimation.

The first part of this section will investigate the mesh resolution represented by $L/\Delta x$. The Δx is the uniform mesh near the hull as described in Fig. 4.5. Fig. 4.9 shows the convergence test of $L/\Delta x$ for the static drift test, and the $L/\Delta x$ ranges from 150 to 500. The static tests usually have a small variation of body attitudes, so the sinkage and trim slightly change with respect to the grid resolution. The insignificant change of surge force is also observed because the surge force mainly comes from the bow.

Relative high dependency of the resolution $L/\Delta x$ is found on the sway force and yaw moment. The pressure field on hull is over-predicted when the mesh resolution is insufficient, which results in a slightly higher trim angle. As the resolution improves, the convergence can be well observed for the sway force and yaw moment, as shown in Fig. 4.9.



(a) Sinkage τ and trim σ



(b) Surge force X , sway force Y , and yaw moment N

Fig. 4.9 Convergence test of mesh resolution, $\beta_0=18^\circ$

(fixed cond': $L/\Delta n = 8000$, $1/\Delta t = 200$)

Table 4.5 Uncertainty of the general mesh resolution for static drift test, $\beta_0 = 18^\circ$ (fixed: $L/\Delta n = 10^4$, $1/\Delta t = 200$)

	Sinkage (m)	Trim ($^\circ$)	Surge force $X^{(0)}$,	Sway force $Y^{(0)}$,	Yaw mom. $N^{(0)}$,
Grid resolution $L/\Delta x_1$	500	500	500	500	500
Grid resolution $L/\Delta x_2$	380	380	380	380	380
Grid resolution $L/\Delta x_3$	250	250	250	250	250
Solution ϕ_1	-2.94E-02	3.26E-01	-2.07E-02	1.22E-01	4.90E-02
Solution ϕ_2	-2.90E-02	3.24E-01	-2.11E-02	1.21E-01	4.97E-02
Solution ϕ_3	-2.91E-02	3.27E-01	-2.05E-02	1.31E-01	5.21E-02
ε_{21}	4.05E-04	-1.47E-03	-3.79E-04	-7.79E-04	7.37E-04
ε_{32}	-1.19E-04	2.65E-03	5.97E-04	9.41E-03	2.35E-03
Convergence ratio R	-3.42	-0.55	-0.63	-0.08	0.31
Convergence tendency	OSC	OSC	OSC	OSC	MT
Oscillatory uncertainty (% ϕ_1)	0.69%	0.41%	1.44%	3.86%	-
CF-based uncertainty (% ϕ_1)	-	-	-	-	2.15%
SF-based uncertainty (% ϕ_1)	-	1.02%	5.34%	0.18%	2.41%
Extrapolated solution (% ϕ_1)	-	101%	96%	100%	98%

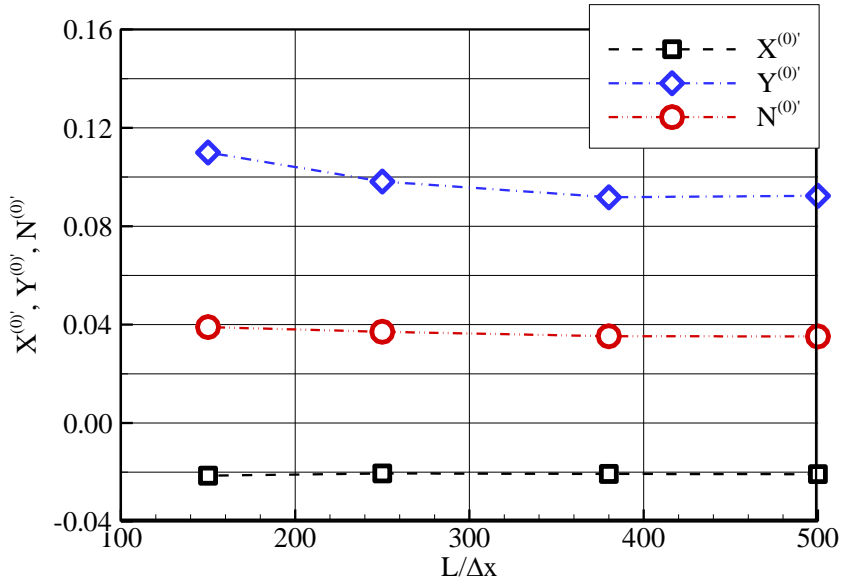
Fig. 4.10 and Table 4.6 present the convergence and the uncertainties of grid resolution for the combined drift-yaw test. The combined motion condition is selected to be $r_0' = 0.5$ and $\beta_0 = 12^\circ$. Fig. 4.10 (a) contains the mean components of surge force, sway force, and yaw moment; while Fig. 4.10 (b) is about the harmonic components.

In Fig. 4.10, the mean force/moment components of this combined PMM test have a similar tendency as that observed in the static drift test. The dependency of the mesh solution is mainly found on the sway force and yaw moment. The dependency is also observed on the harmonic force components.

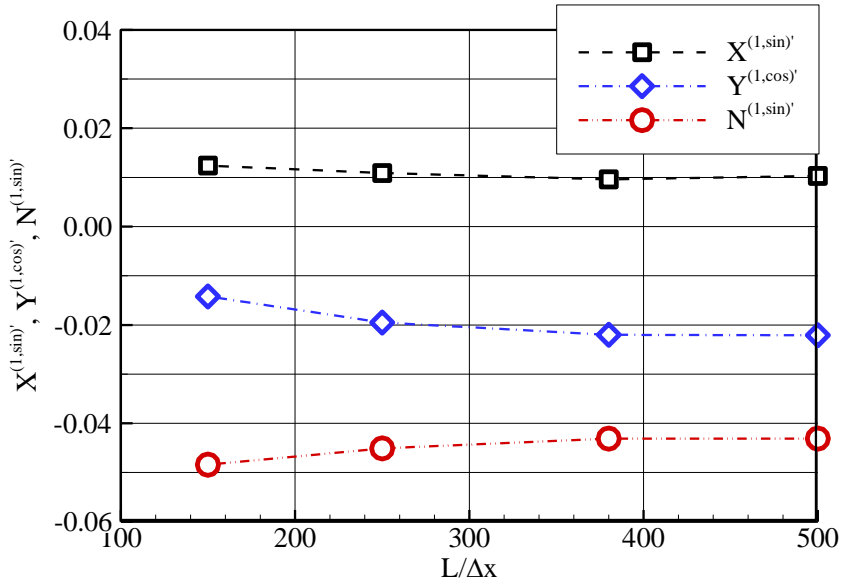
The numerical uncertainties are generally in an acceptable range, which means the solution is convergent at the high resolution of $L/\Delta x = 500$. The harmonic component $X^{(1,\sin)}$ has a high uncertainty because the periodical surge force is interfered with the oscillation caused by the initial transition stage. Such interference is weak on the sway force and yaw moment which have considerable magnitude.

Except for the mesh resolution, the time step as another important discretization factor will also be investigated in this study. The tests will consider three different time steps, $\Delta t = 0.005s, 0.0075s, 0.01s$.

Table 4.7 presents the uncertainties of time step for the static drift test. It is a static test so the uncertainties of time step are almost negligible. The uncertainties of the combined drift-yaw test (harmonic period $T_0 = 11.18s$) are shown in Table 4.8, and the force signals shown in Fig. 4.11 indicate that the current time step is also sufficient for the harmonic PMM tests.



(a) Mean force/moment components



(b) Harmonic force/moment components

Fig. 4.10 Convergence test of mesh resolution, $r_0'=0.5$, $\beta_0=12^\circ$
(fixed cond': $L/\Delta n = 8000$, $T_0/\Delta t = 2236$)

Table 4.6 Uncertainty of the general mesh resolution for drift-yaw test, $\tau_0' = 0.5$, $\beta_0 = 12^\circ$ (fixed: $L/\Delta n = 10^4$, $T_0/\Delta t = 2236$)

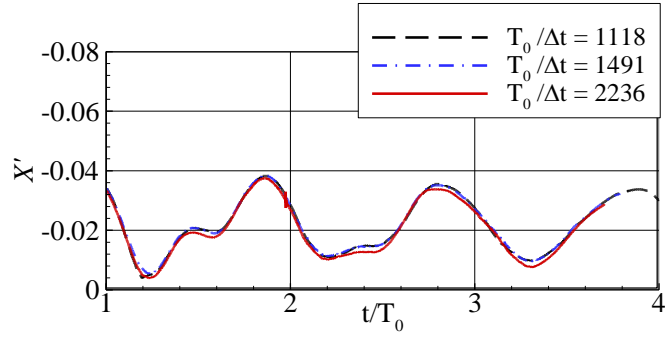
	Surge force $X^{(0)'}_1$	Sway force $Y^{(0)'}_1$	Yaw mom. $N^{(0)'}_1$	Surge force $X^{(1,\sin)'}_1$	Sway force $Y^{(1,\cos)'}_1$	Yaw mom. $N^{(1,\sin)'}_1$
Grid resolution $L/\Delta x_1$	500	500	500	500	500	500
Grid resolution $L/\Delta x_2$	380	380	380	380	380	380
Grid resolution $L/\Delta x_3$	250	250	250	250	250	250
Solution ϕ_1	-2.08E-02	9.24E-02	3.52E-02	1.03E-02	-2.21E-02	-4.308E-02
Solution ϕ_2	-2.07E-02	9.18E-02	3.53E-02	9.60E-03	-2.20E-02	-4.312E-02
Solution ϕ_3	-2.05E-02	9.82E-02	3.71E-02	1.09E-02	-1.95E-02	-4.514E-02
ε_{21}	1.40E-04	-5.79E-04	1.26E-04	-6.89E-04	7.44E-05	-4.47E-05
ε_{32}	1.74E-04	6.31E-03	1.80E-03	1.30E-03	2.46E-03	-2.02E-03
Convergence ratio R	0.81	-0.09	0.07	-0.53	0.03	0.02
Convergence tendency	MT	OSC	MT	OSC	MT	MT
Oscillatory uncertainty (% ϕ_1)	-	3.42%	-	6.34%	-	-
CF-based uncertainty (% ϕ_1)	2.15%	-	0.89%	-	0.89%	0.27%
SF-based uncertainty (% ϕ_1)	2.67%	0.19%	0.10%	14.07%	0.05%	0.01%
Extrapolated solution (% ϕ_1)	102%	100%	100%	111%	100%	100%

Table 4.7 Uncertainty of the time-step for static drift test, $\beta_0 = 18^\circ$ (fixed: $L/\Delta x = 380$, $L/\Delta n = 10^4$.)

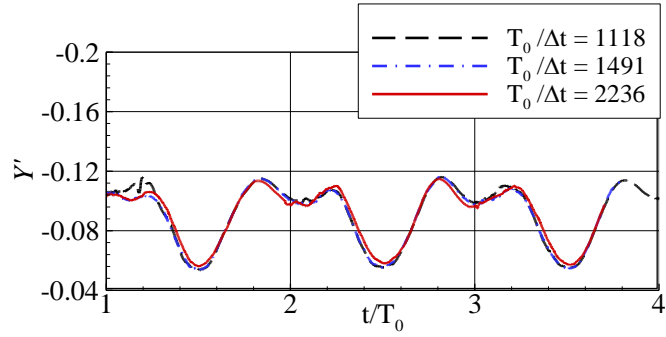
	Sinkage (m)	Trim ($^\circ$)	Surge force $X^{(0)}$,	Sway force $Y^{(0)}$,	Yaw mom. $N^{(0)}$,
Time-step $1/\Delta t_1$	200	200	200	200	200
Time-step $1/\Delta t_2$	133	133	133	133	133
Time-step $1/\Delta t_3$	100	100	100	100	100
Solution ϕ_1	-2.90E-02	3.24E-01	-2.11E-02	1.21E-01	4.97E-02
Solution ϕ_2	-2.89E-02	3.25E-01	-2.10E-02	1.21E-01	4.97E-02
Solution ϕ_3	-2.89E-02	3.25E-01	-2.11E-02	1.21E-01	4.97E-02
ε_{21}	4.68E-05	2.76E-04	8.15E-05	1.14E-04	-6.31E-05
ε_{32}	4.23E-06	-8.75E-05	-5.15E-05	4.76E-05	4.23E-05
Convergence ratio R	11.07	-3.16	-1.58	2.4	-1.49
Convergence tendency	Div	OSC	OSC	Div	OSC
Oscillatory uncertainty (% ϕ_1)	–	-0.04%	-0.12%	–	0.04%
CF-based uncertainty (% ϕ_1)	0.22%	–	–	0.17%	–
SF-based uncertainty (% ϕ_1)	0.04%	–	–	0.21%	–
Extrapolated solution (% ϕ_1)	100%	–	–	100%	–

Table 4.8 Uncertainty of the time-step for drift-yaw test, $r_0' = 0.5$, $\beta_0 = 12^\circ$ (fixed: $L/\Delta x = 380$, $L/\Delta n = 10^4$)

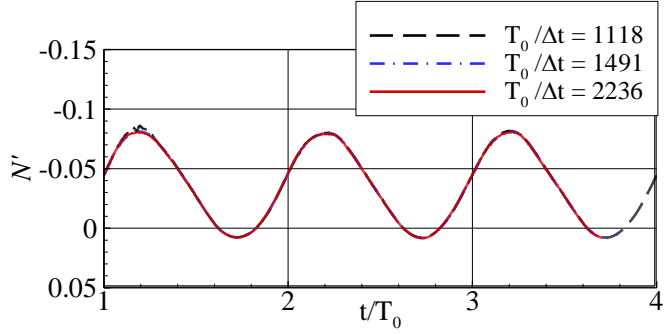
	Surge force $X^{(0)'} ,$	Sway force $Y^{(0)'} ,$	Yaw mom. $N^{(0)'} ,$	Surge force $X^{(1,\sin)'} ,$	Sway force $Y^{(1,\cos)'} ,$	Yaw mom. $N^{(1,\sin)'} ,$
Time-step $T_0/\Delta t_1$	2236	2236	2236	2236	2236	2236
Time-step $T_0/\Delta t_2$	1491	1491	1491	1491	1491	1491
Time-step $T_0/\Delta t_3$	1118	1118	1118	1118	1118	1118
Solution ϕ_1	-2.07E-02	9.18E-02	3.53E-02	9.60E-03	-2.10E-02	-4.31E-02
Solution ϕ_2	-2.12E-02	9.08E-02	3.54E-02	9.43E-03	-2.21E-02	-4.31E-02
Solution ϕ_3	-2.11E-02	9.16E-02	3.58E-02	9.93E-03	-2.38E-02	-4.36E-02
ε_{21}	-5.21E-04	-1.07E-03	1.15E-04	-1.76E-04	-1.11E-03	3.94E-06
ε_{32}	1.27E-04	7.79E-04	3.43E-04	5.06E-04	-1.71E-03	-4.36E-04
Convergence ratio R	-4.1	-1.4	0.3	-0.3	0.6	0
Convergence tendency	OSC	OSC	MT	OSC	MT	MT
Oscillatory uncertainty (% ϕ_1)	1.27%	0.58%	-	0.92%	-	-
CF-based uncertainty (% ϕ_1)	-	-	0.45%	-	4.76%	0.01%
SF-based uncertainty (% ϕ_1)	-	-	0.09%	0.81%	4.27%	0.00%
Extrapolated solution (% ϕ_1)	-	-	100%	101%	97%	100%



(a) Normalized surge force X'



(b) Normalized sway force Y'



(c) Normalized yaw moment N'

Fig. 4.11 Force/moment signals with different time-steps, $r_0'=0.5$, $\beta_0=12^\circ$
(fixed cond': $L/\Delta n = 8000$, $L/\Delta x = 380$)

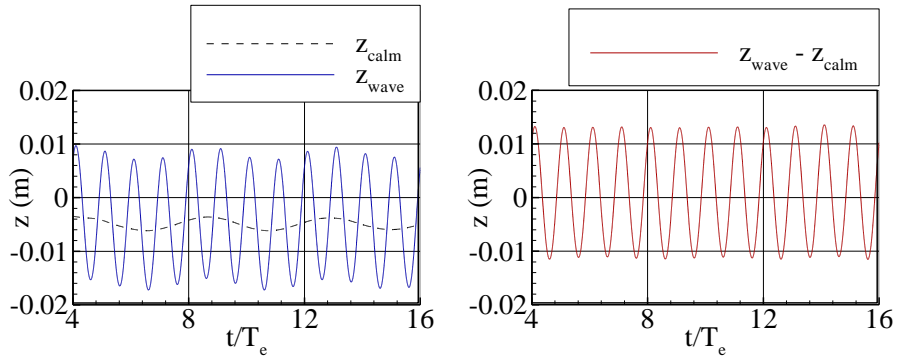
4.3 Case II: Seakeeping test

This part used the 1/85 scaled KCS model listed in the previous Table 2.2. One wave case ($\lambda/L = 1.0$, $H/\lambda = 1/60$, $\chi = 180^\circ$) was selected to estimate the numerical uncertainties. The time window and discretization parameters were examined, and the generated numerical waves were also observed.

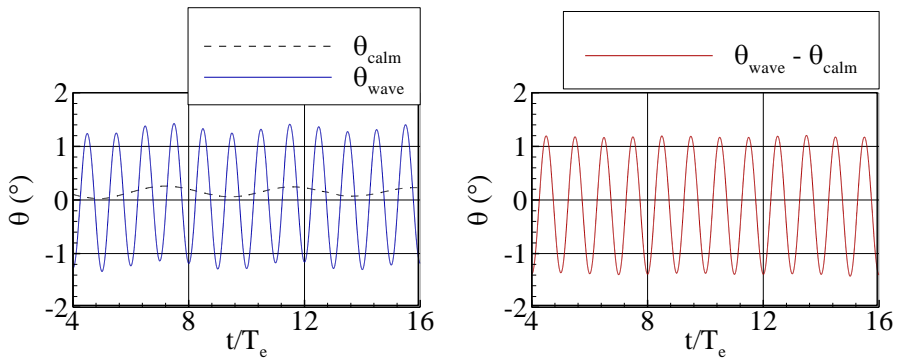
4.3.1 Uncertainty of time window

Previous calm-sea cases discussed the numerical oscillation phenomenon that can disturb the analysis results, and the corresponding uncertainty can be controlled by selecting an appropriate time window related to the period of numerical oscillation. However, the time window of a seakeeping case is mainly selected based on the wave encounter period, its selection associated with the original numerical oscillation could generate uncertainty. This uncertainty can be significant, especially for the added resistance data.

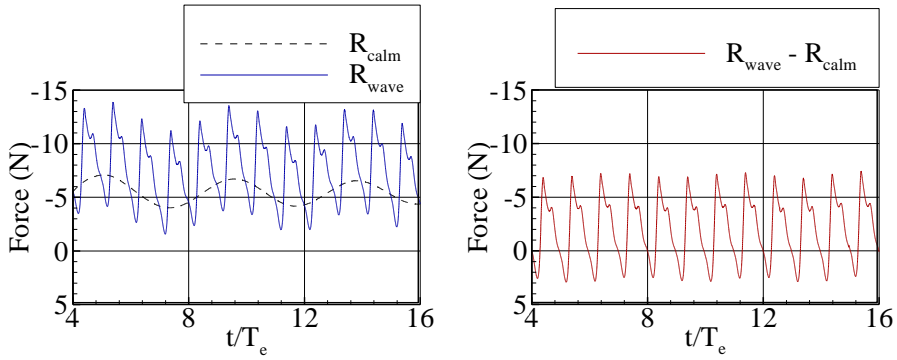
To focus on the wave effect, the present work choosed to observe the signal subtracted by the two raw signals that are obtained from the calm-sea condition and wave condition. The same mesh system was used for both the calm-sea test and the seakeeping test. Fig. 4.12 gives two groups of figures about the motion and resistance signals. The figures on the left-hand side are the raw signals obtained from the calm-sea condition and wave condition. The numerical oscillation discussed in Section 4.1.1 can be clearly observed, particularly on the resistance signal. The figures on the right-hand side are the signals subtracted from the two raw signals, it represents the pure wave effects and the original numerical oscillation becomes less significant.



(a) Heave motion z



(b) Pitch motion θ



(c) Resistance X

Fig. 4.12 Typical motion and resistance signals, $\lambda/L=1.0$, $H/\lambda=1/60$

Table 4.9 has summarized the running average results based on the subtracted signals. The interval of running average is $10T_e$. It can be observed that the uncertainty U_{RA} is acceptable.

Table 4.9 Time window uncertainty of the seakeeping test ($\lambda/L = 1.0$)

	Heave amplitude (m)	Pitch amplitude (°)	Mean resistance (N)
RA_{min}	0.0122	1.28	1.94
RA_{max}	0.0122	1.28	2.02
U_{RA} (% RA_{mean})	0.0%	0.0%	2.0%

4.3.2 Uncertainty of discretization parameters

To predict the ship motion in waves, the priority is to examine the quality of the propagating waves generated by the moving numerical tank. It is a common challenge for numerical wave tank that the wave dissipation or dispersion can be caused by discretization, interfere reconstruction and others.

The first discretization parameter to check is the grid size, and the term $\lambda/\Delta x$ is used as the refinement index. λ is wavelength, and Δx is the longitudinal size of the grids near waves. The transverse size of the grids remains the same as Δx . A change of this resolution $\lambda/\Delta x$ indicates a proportional change of both the overall mesh resolution and the time step. It indicates that the grid aspect ratio remains the same and the CFL condition should ideally be the same in each mesh cell. Table 4.10 outlines the discretization parameters for each test case, H is wave height, Δz is the vertical size of grids, T_e is the wave encounter period, and Δt is time step.

Table 4.10 Test cases with different discretization parameters

Case	$\lambda/\Delta x$	$H/\Delta z$	$U_e \cdot \Delta t/\Delta x$
# 1	40	6	0.20
# 2	60	9	0.20
# 3	80	12	0.20
# 4	100	15	0.20

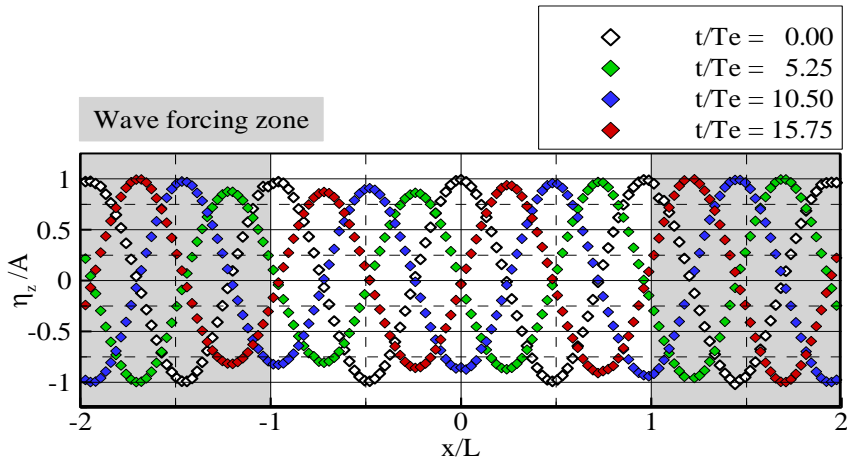


Fig. 4.13 Wave profiles inside the wave tank

$$(\lambda/\Delta x = 100, H/\Delta z = 15, U_e \cdot \Delta t/\Delta x = 0.20)$$

The typical wave profiles inside the tank are shown in Fig. 4.13. The x -axis indicates the longitudinal location x inside the tank, L is the ship length. The z_η is measured wave elevation. The wave profiles of four time instants are shown, namely the instants that t/T_e equals 0, 5.25, 10.50, 15.75. The region of grey color indicates the wave forcing zone. The smearing phenomenon of numerical waves is observed along with the spatial location, but the smearing is not exacerbated as time marches.

To observe the convergence of the numerical waves, the numerical wave probe was allocated at the center of computational tank. The first-order

amplitude of the probe signal is specified as the measured wave amplitude η . The convergence test with respect to mesh resolution is summarized in Fig. 4.14. The measured wave amplitude η is normalized by the nominal wave amplitude A , and it shows a gradually convergent tendency as the mesh resolution becomes finer. It should be admitted that the present tank provides the smearing of about 6% to the amplitude of generated waves.

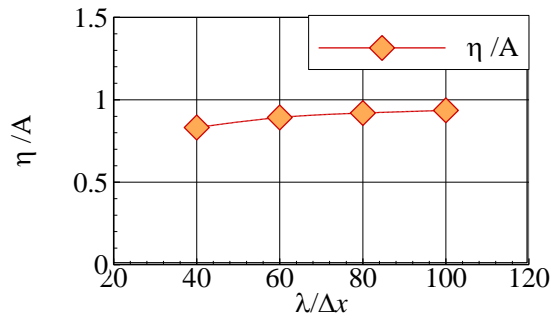


Fig. 4.14 Convergence test of mesh resolution on the wave elevations

The convergence with respect to mesh resolution was further observed in the wave-induced motions and wave added resistance. Fig. 4.15 shows the results and it has presented two normalization strategies for the predicted motion and added resistance. One normalization strategy is to use the nominal wave amplitude A and wavenumber k , which is the most common way for hydrodynamic analysis. However, unlike the analytical methods, the numerical computation could introduce uncertainty and bias to the generated wave fields, it might be more reasonable to use the measured wave amplitude rather than the nominal value. Thus, another normalization strategy is to normalize the motion responses and added resistance by the measured wave amplitude η which has been discussed in Fig. 4.14.

In Fig. 4.15, the results normalized by nominal wave amplitude are

underestimated by the coarse mesh resolution, and the results become convergent as increasing the mesh refinement. By comparison, the results normalized by the measured wave amplitude show less dependency on the mesh resolution. This means that the reliability of predicted motion and resistances are mainly determined by the quality of numerical waves.

The numerical uncertainty of mesh resolution is summarized in Table 4.11. The predicted waves show a monotonic convergence and the estimated numerical uncertainty is around 5~7%. For the motion and added resistance normalized by nominal wave amplitude A , the uncertainties are very small although a slight oscillatory tendency is observed. By comparison, the values normalized by measured wave amplitude η have shown relatively large uncertainties, especially the SF-based uncertainties. It is because the solutions are already convergent and the relative differences of solutions are too small.

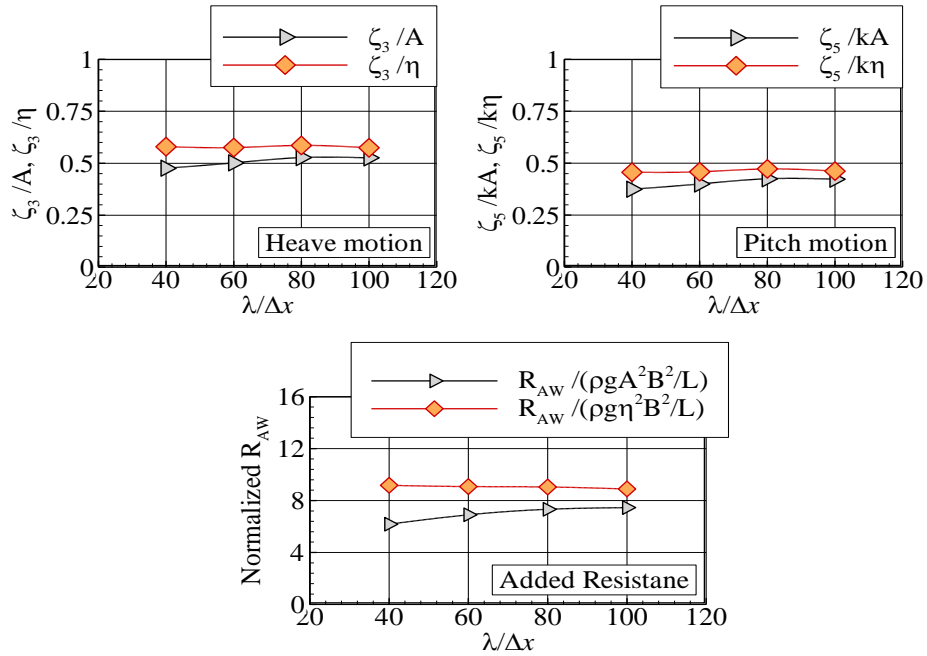


Fig. 4.15 Convergence test of mesh resolution on motion and added resistance

Table 4.11 Uncertainty of the mesh resolution for seakeeping test (fixed: $\Delta x/\Delta z = 9$, $U_c \Delta t/\Delta x = 0.20$)

	Wave amp. η/A	Heave ξ_3/A	Pitch ξ_5/kA	Added R_{aw} $/(\rho g A^2 B^2/L)$	Heave ξ_3/η	Pitch $\xi_5/k\eta$	Added R_{aw} $/(\rho g \eta^2 B^2/L)$
Grid resolution $\lambda/\Delta x_1$	100	100	100	100	100	100	100
Grid resolution $\lambda/\Delta x_2$	80	80	80	80	80	80	80
Grid resolution $\lambda/\Delta x_3$	60	60	60	60	60	60	60
Solution ϕ_1	9.16E-01	5.26E-01	4.23E-01	7.46E+00	5.74E-01	4.62E-01	8.89E+00
Solution ϕ_2	9.00E-01	5.27E-01	4.25E-01	7.33E+00	5.86E-01	4.72E-01	9.05E+00
Solution ϕ_3	8.72E-01	5.02E-01	4.00E-01	6.90E+00	5.75E-01	4.59E-01	9.08E+00
ε_{21}	-1.59E-02	1.39E-03	1.90E-03	-1.30E-01	1.17E-02	1.03E-02	1.56E-01
ε_{32}	-2.80E-02	-2.55E-02	-2.50E-02	-4.25E-01	-1.04E-02	-1.35E-02	3.08E-02
Convergence ratio R	0.57	-0.05	-0.08	0.31	-1.12	-0.76	5.07
Convergence tendency	MT	OSC	OSC	MT	OSC	OSC	Div
Oscillatory uncertainty (% ϕ_1)	-	2.43%	2.96%	-	0.91%	1.47%	-
CF-based uncertainty (% ϕ_1)	5.75%	-	-	4.88%	-	-	5.95%
SF-based uncertainty (% ϕ_1)	7.07%	0.04%	0.08%	1.77%	-	9.99%	0.23%
Extrapolated solution (% ϕ_1)	106%	100%	100%	101%	-	92%	100%

The second discretization parameter to check is the time step. A single mesh system of resolution ($\lambda/\Delta x = 80$, $H/\Delta z = 12$) was used to test the time-step $T_e/\Delta t$ varying from 200 to 500, where T_e is the wave encounter period. Fig. 4.16 shows the measured wave amplitude with respect to different time steps. The monotonic convergence is observed, and the relative differences in using various time steps are not that large.

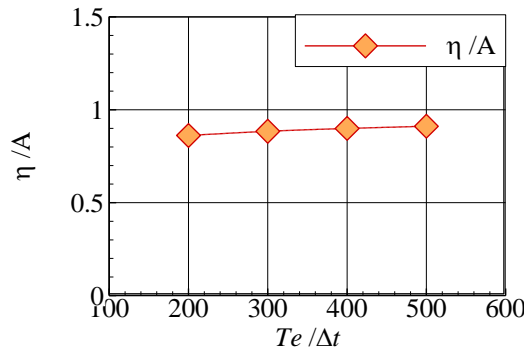


Fig. 4.16 Convergence test of time step on the wave elevations

For the wave-induced motion and added resistance shown in Fig. 4.17, the convergence shows a similar tendency as that observed in the previous convergence test of mesh resolution. The values normalized by the measured wave amplitude show a nearly constant tendency, since the dependency on time-step is also dominated by the predicted numerical waves. This study would choose the time step of $T_e/\Delta t = 500$ for further seakeeping cases.

Table 4.12 has summarized the numerical uncertainties of time-step. It can be found that the wave amplitude shows a huge uncertainty despite the monotonic convergence observed in previous Fig. 4.16. The reason is that the relative differences of solutions are too small, and the calculated apparent order p (Eq. 4.2) is about 0.04, which is too small compared with the

theoretical apparent order of 2. The pitch motion normalized by nominal wave amplitude A also shows a relatively large uncertainty under monotonic convergence. But this uncertainty can be well restrained by using the measured wave amplitude as the normalization factor.

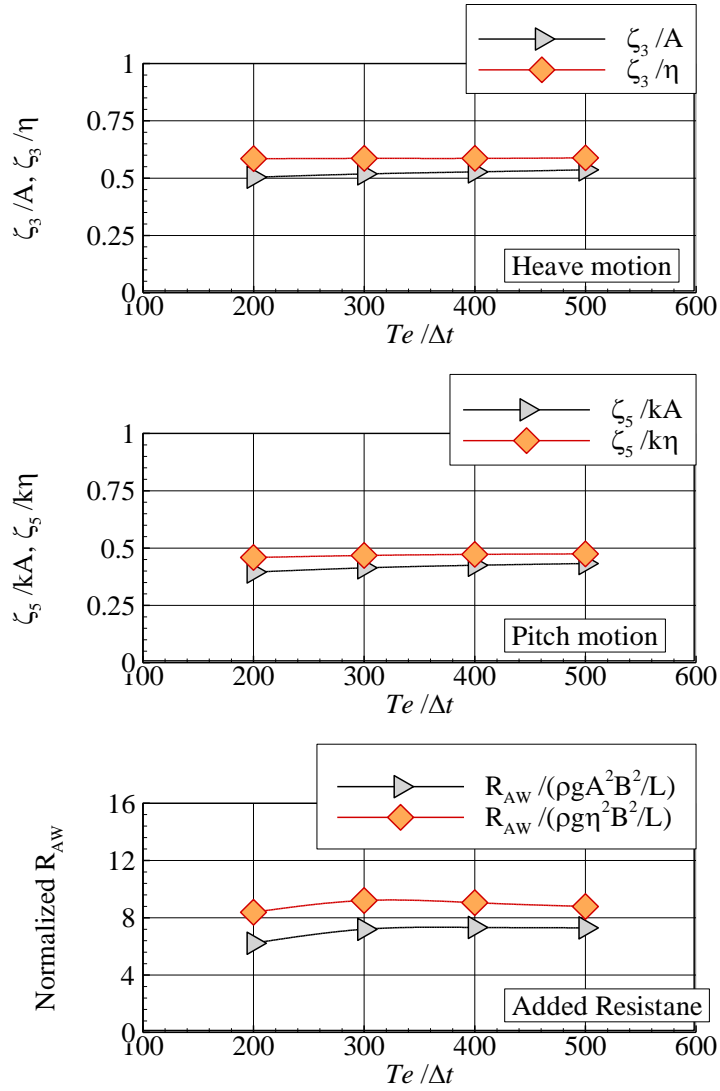


Fig. 4.17 Convergence test of time step on motion and added resistance

Table 4.12 Uncertainty of the time-step for seakeeping test (fixed: $\lambda/\Delta x = 100$, $U_c \Delta t/\Delta x = 0.20$)

	Wave amp. η/A	Heave ξ_3/A	Pitch ξ_5/kA	Added R_{aw} $/(\rho g A^2 B^2/L)$	Heave ξ_3/η	Pitch $\xi_5/k\eta$	Added R_{aw} $/(\rho g \eta^2 B^2/L)$
Time-step $T_e/\Delta t_1$	500	500	500	500	500	500	500
Time-step $T_e/\Delta t_2$	400	400	400	400	400	400	400
Time-step $T_e/\Delta t_3$	300	300	300	300	300	300	300
Solution ϕ_1	9.12E-01	5.36E-01	4.33E-01	7.30E+00	5.89E-01	4.75E-01	8.79E+00
Solution ϕ_2	9.00E-01	5.27E-01	4.25E-01	7.33E+00	5.86E-01	4.73E-01	9.05E+00
Solution ϕ_3	8.84E-01	5.18E-01	4.14E-01	7.20E+00	5.86E-01	4.68E-01	9.21E+00
ε_{21}	-1.19E-02	-9.14E-03	-7.66E-03	2.49E-02	-2.36E-03	-2.22E-03	2.65E-01
ε_{32}	-1.53E-02	-8.98E-03	-1.14E-02	-1.27E-01	-3.67E-05	-4.76E-03	1.53E-01
Convergence ratio R	0.78	1.02	0.67	-0.2	64.28	0.47	1.74
Convergence tendency	MT	Div	MT	OSC	Div	MT	Div
Oscillatory uncertainty (% ϕ_1)	-	-	-	0.87%	-	-	-
CF-based uncertainty (% ϕ_1)	147.90%	4.73%	12.58%	-	1.43%	0.83%	8.66%
SF-based uncertainty (% ϕ_1)	182.45%	5.81%	15.44%	0.16%	0.00%	1.04%	2.26%
Extrapolated solution (% ϕ_1)	246%	105%	112%	100%	100%	101%	98%

5. Validation of Numerical Method

Considering the limitation that no direct experimental tests can be used to validate the numerical PMM tests in waves. Two independent series of validation tests, the PMM tests in calm sea and the seakeeping tests, have been carried out based on the KCS container model.

5.1 Case I: PMM test in calm sea

This case applied a 1/40 scaled KCS model, and it was validated with the experimental work (**Sung and Park, 2015**) that includes static drift test, pure sway test, pure yaw test, and combined drift-yaw tests. The Froude number is 0.26 for this series of tests

5.1.1 Static drift test

The static drift tests have been carried out with the drift angle varying from 0 to 18°. The body surge force, sway force, and yaw moment were measured to obtain the derivatives with respect to the sway velocity which is represented by drift angle.

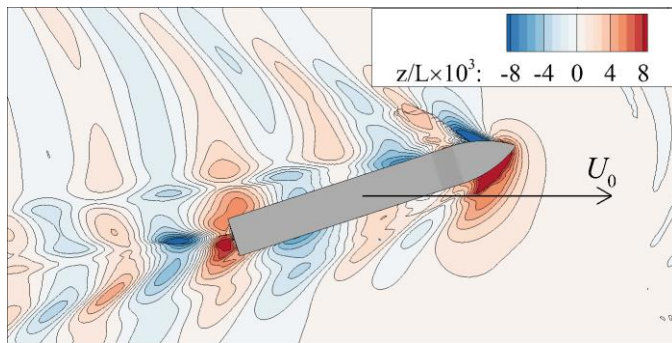


Fig. 5.1 Free surface pattern of static drift test, $\beta_0 = 18^\circ$

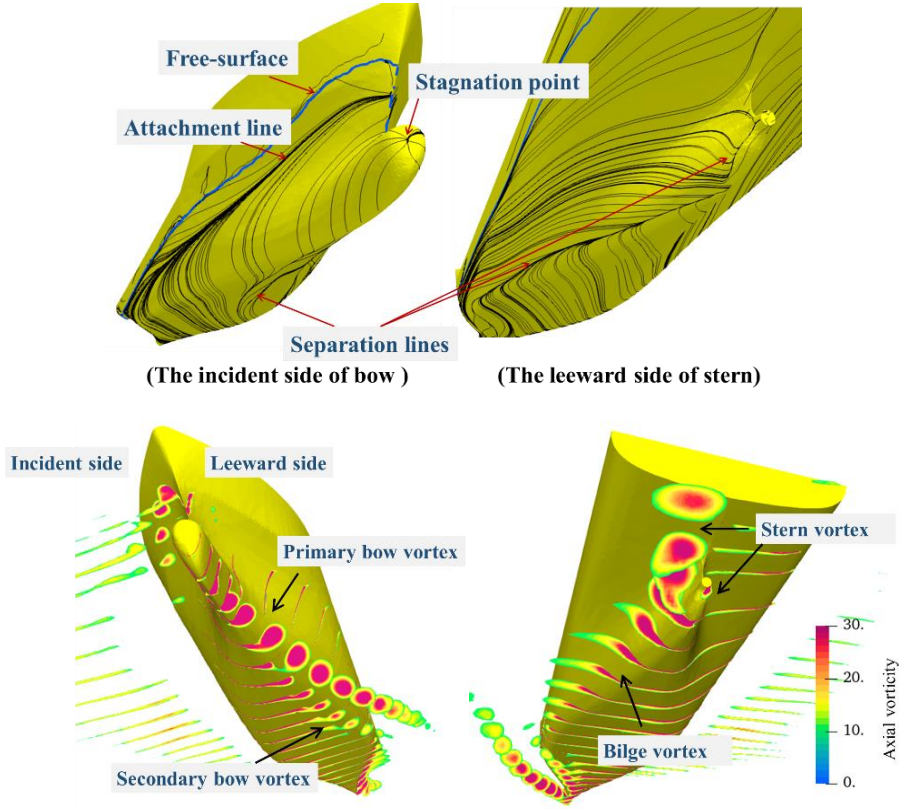


Fig. 5.2 Streamlines and vorticity field near the hull, $\beta_0 = 18^\circ$

The present work selected the 18° drift case to observe the vortex shedding intensified by the body transverse velocity. Fig. 5.1 is the free surface pattern that shows the motion trajectory due to drift angle and high Fn condition. The free surface elevation z is normalized by ship length L . The high wave elevation is observed near the bow, while the flow near the stern is mild. Fig. 5.2 presents the surface limiting streamlines and the sectional distribution of axial vorticity ($|\omega_x|$), illustrating how the vortices shed around the ship bow, bilge, and stern. Near the bow, a stagnation point is observed at the side of the drifting motion, and the separation line beneath the bow indicates the

generation of bow vortices. The separation lines extend along the ship bilge until the end section of the nominal propeller region. Meanwhile, the bow vortex induced by the bulbous bow has a significant strength as the stern vortex.

Fig. 5.3 compares the predicted force/moment under different drift angles. The viscous component of surge force predicted by the present CFD method is also added to understand the contribution of viscous effect. It can be seen that the viscous component increases as the static drift angle becomes high, but the main increase of surge force is still contributed by the pressure component. The sway force and yaw moment are dominated by the pressure on the ship lateral surface thus their viscous components are almost negligible. With respect to the static drift angle, the present KCS hull shows a nonlinear sway force and relatively linear yaw moment. The agreement between the present CFD results and the others is well achieved for both the body forces and moment.

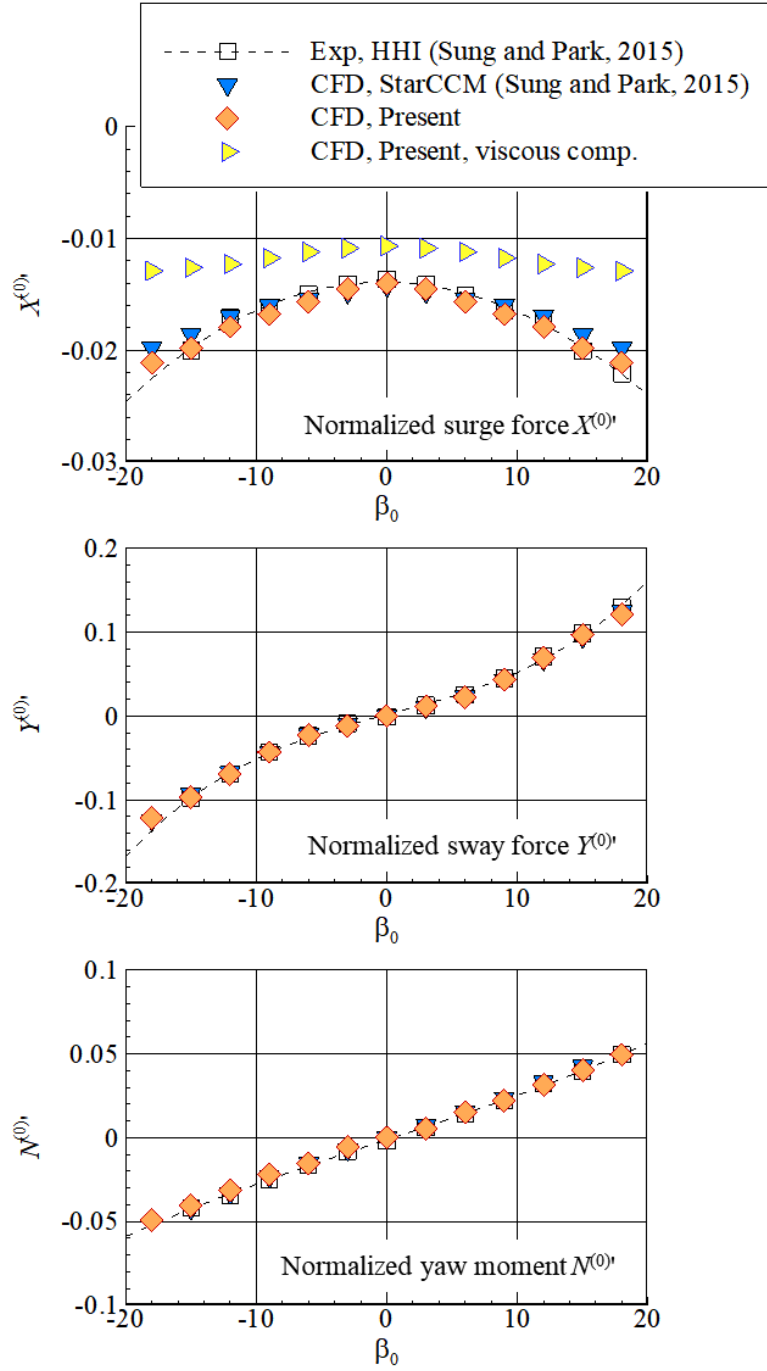


Fig. 5.3 Comparison of the normalized force/moment w.r.t. drift angle

5.1.2 Pure sway test

A series of pure sway tests have been carried out with the different sway acceleration (\dot{v}') conditions varying from 0.1 to 0.3. The evolution of the free surface pattern and the vorticity fields during the dynamic swaying motion is presented in Fig. 5.4. The sequential figures indicate the four stages that the ship has the maximum sway velocity or maximum sway acceleration in both two lateral directions. The T_0 is the harmonic swaying period. Free surface elevation z is normalized by ship length L .

One of the flow characteristics can be observed from this dynamic swaying test is the symmetric behavior of both the free surface pattern and the vorticity. For example, the instant $t/T_0 = 1.0$ generates the flow patterns that are almost symmetric to the flow patterns generated at the instant $t/T_0 = 1.5$, as observed in Fig. 5.4. Both the free-surface pattern and vorticity field are not obviously interfered by the previous motion stage.

Meanwhile, at the instant that maximum sway velocity is reached, both the wave elevation and vortices become significant near the ship, which is similar to the phenomena observed in the static drift test. At the instant that the sway acceleration becomes maximum while the sway velocity becomes zero, the flow near the ship becomes much milder. The interference of motion-induced vortices becomes insignificant for this stage that the added mass effect works.

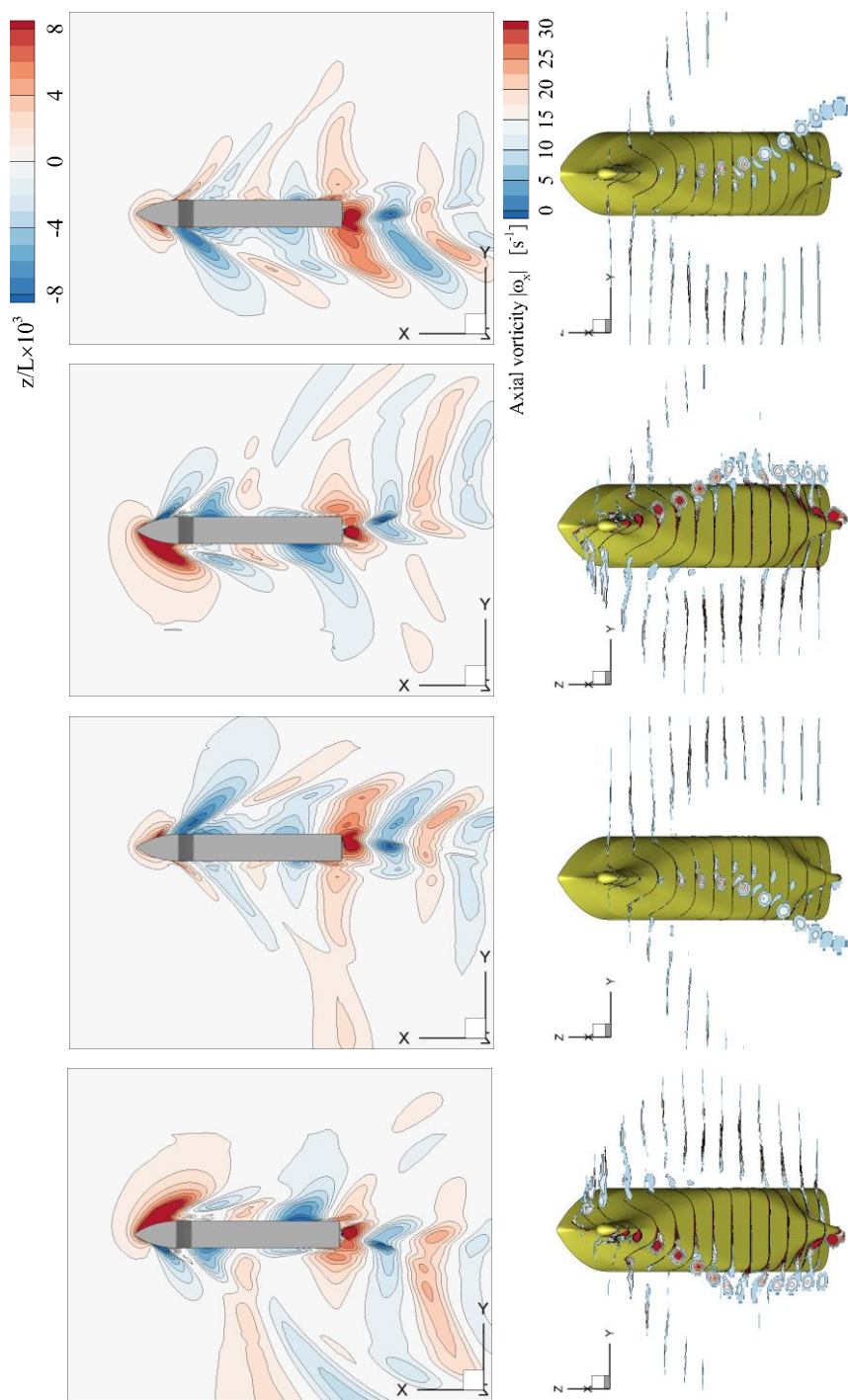


Fig. 5.4 Sequential wave pattern of pure sway test, $v_0' = 0.309$ ($t/T_0 = 1.00, 1.25, 1.50, 1.75$)

Fig. 5.5 presents the 1st-order sine components (in-phase components) of sway force $Y^{(1,\sin)}$ and yaw moment $N^{(1,\sin)}$ that are used to generate the added mass coefficients that are almost independent of viscous effect. The sway force has a considerable in-phase component, and the strong linearity is found between the in-phase component and the sway acceleration. The in-phase component of yaw moment is always small.

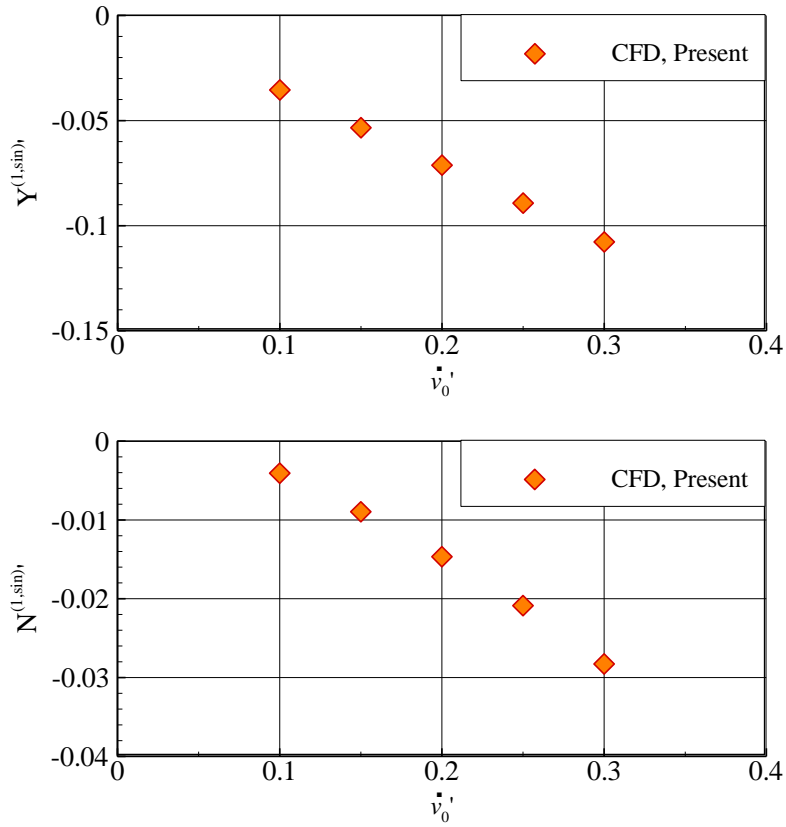


Fig. 5.5 Comparison of the normalized force/moment w.r.t. sway acceleration

5.1.3 Yaw test

This part involves a series of ship yawing tests including both the pure yaw test and the combined drift-yaw test. The yawing motion has a yaw rate r_0' ranging from 0.1 to 0.5, and the additional static drift angle is up to 12° . The pure yaw test is used to generate the manoeuvring coefficients of yaw rate r , and the combined drift-yaw test is designed for the cross-coupling coefficients of sway velocity v and yaw rate r .

The evolutions of the free surface pattern and the vorticity fields of the ship pure yaw test are presented in Fig. 5.6. Similar to the pure sway test, the symmetric characteristic of flow development is also observed in the pure yaw test. The vorticity field near the ship is still mild at the instants $t/T_0 = 1.0$ and 1.5 when ship has zero yaw rate but maximum yaw acceleration. By comparison, both the free surface elevation and vortices become significant when the ship maximum yaw rate is reached. Due to the yawing motion, the bow vortex and the stern vortex are found to be distributed at the different sides of the hull.

Fig. 5.7 compared the motion and force/moment signals obtained under different motion conditions. The yaw rate r_0' is fixed to be 0.5, and the combined drift angle varies from 0 to 12° . The signal of yaw rate is added to help understand the effects between yawing rate and body force/moment. The mean force and moment in Fig. 5.7 are observed to naturally increase with the additional drift angle, while a considerable change is also observed in the harmonic components of sway force or yaw moment. Particularly for the sine component of yaw moment which is used to extract the coupling coefficient N_{rv} , its significant increase at the highly motion coupled condition indicates that this coefficient plays an important role in ship turning ability.

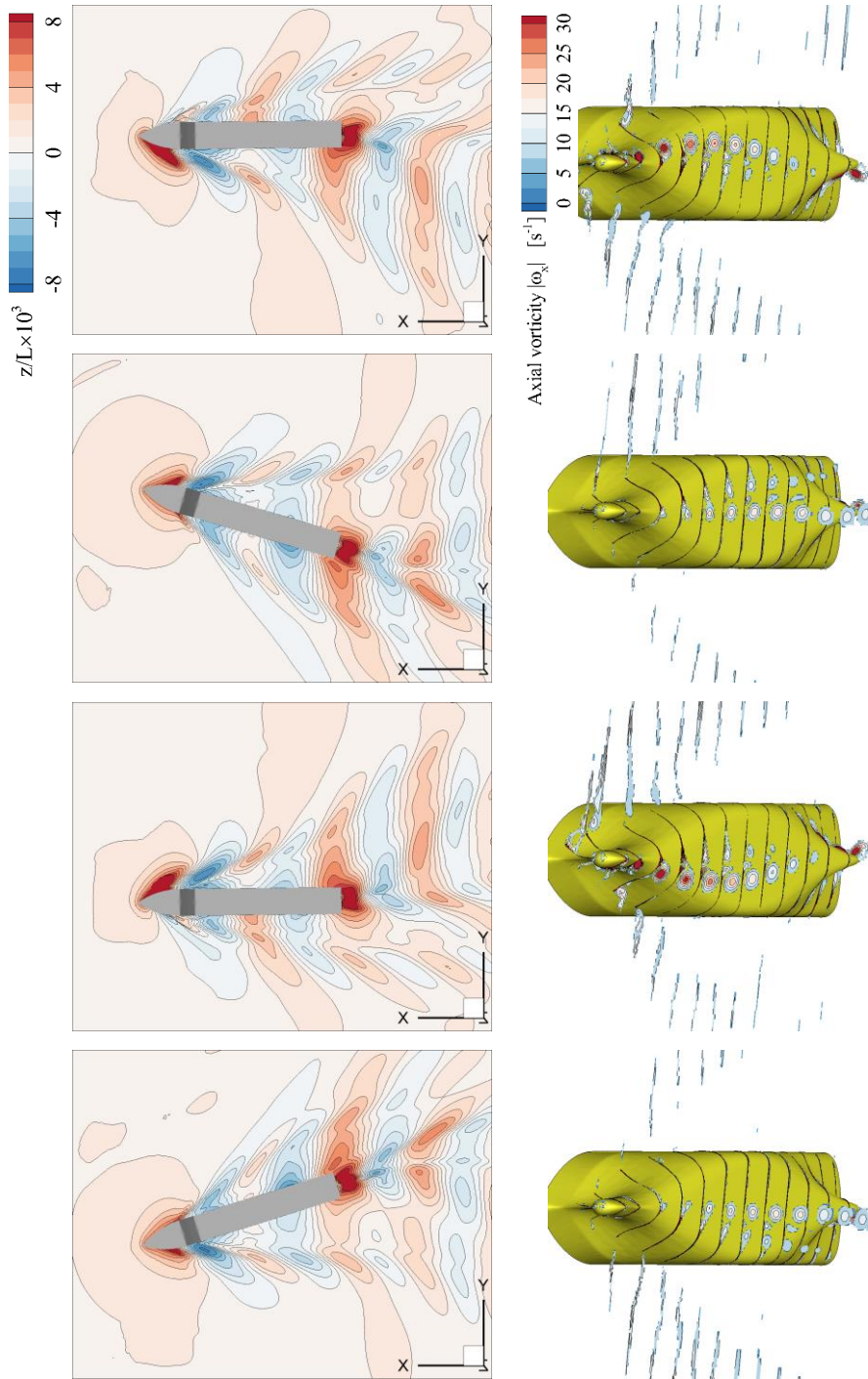


Fig. 5.6 Sequential wave pattern of pure yaw test $r_0' = 0.5(t/T_0) = 1.00, 1.25, 1.50, 1.75$

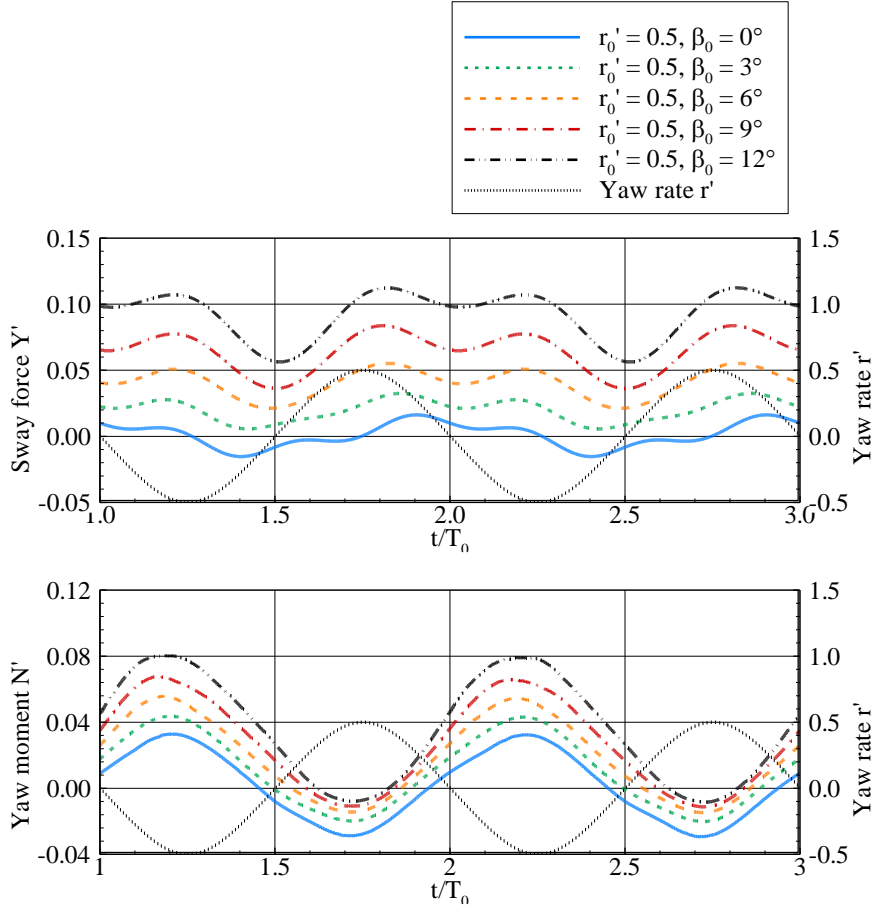
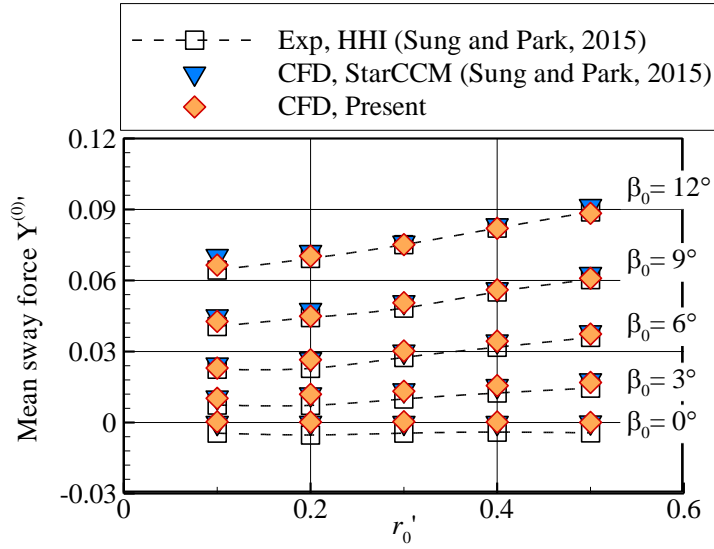
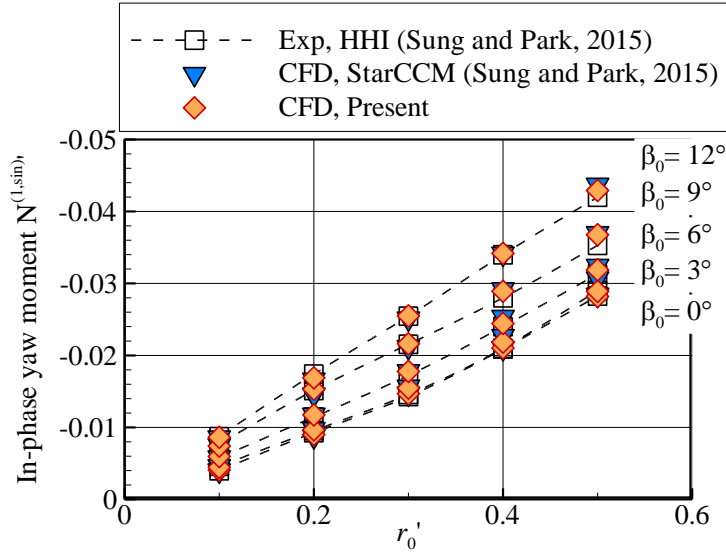


Fig. 5.7 Force/moment signals of the combined drift-yaw test

The force/moment validation of the complete series of combined drift-yaw tests is shown in Fig. 5.8. Generally, the present CFD computation has provided a satisfactory prediction by comparing the predicted results with the other data. The coupling effect on the mean sway force is very weak at the low drift condition and it becomes much nonlinear as the coupling motion increases. For the 1st-order sine component of yaw moment shown in Fig. 5.8(b), the strong linearity is observed even in the highly coupling cases.



(a) Normalized sway force component $Y^{(0)}$



(b) Normalized yaw moment component $N^{(1,\sin)}$

Fig. 5.8 Comparison of the normalized force/moment w.r.t. drift angle and yaw rate

5.2 Case II: Seakeeping test

This case applied a 1/85 scaled KCS model, and it was validated with various experimental and numerical results from the Tokyo 2015 CFD workshop. The wave frequency effect was the first part to validate, and then the wave direct effect was also validated because the later PMM test in waves would involve an oblique wave effect that changes the ship motion responses and added forces. Such validation of ship seakeeping tests can also examine the 6-DOF algorithm of body-wave interactive motion which was designed for the PMM test in waves.

5.2.1 Wave frequency effect

The wave frequency is represented by wavelength, and this validation test has considered the wavelengths varying from $0.5L$ to $1.8L$. A constant wave slope of $H/\lambda = 1/60$ was used for both the present numerical computation and the other referred tests. The comparison tests (Stocker 2016) include two experiment works carried out by the FORCE Technology (Denmark) and the IIHR institute (University of Iowa). As discussed in the numerical convergence test of previous Section 4.2, the predicted motion and added resistance are normalized by the measured amplitude η of numerical waves rather than the nominal wave amplitude A .

Fig. 5.9 shows the wave-induced motion responses including mean, 1st-order, and 2nd-order amplitude. The ship has relatively large mean sinkage and trim in the short waves. Because the ship originally has a sinkage and trim in the calm sea condition, and the changes are limited by the short waves. But when the wavelength becomes close or even higher than the ship length, the ship starts to “ride” on the propagating waves so the mean sinkage and trim

would be reduced. The smallest mean trim value occurs at the resonance.

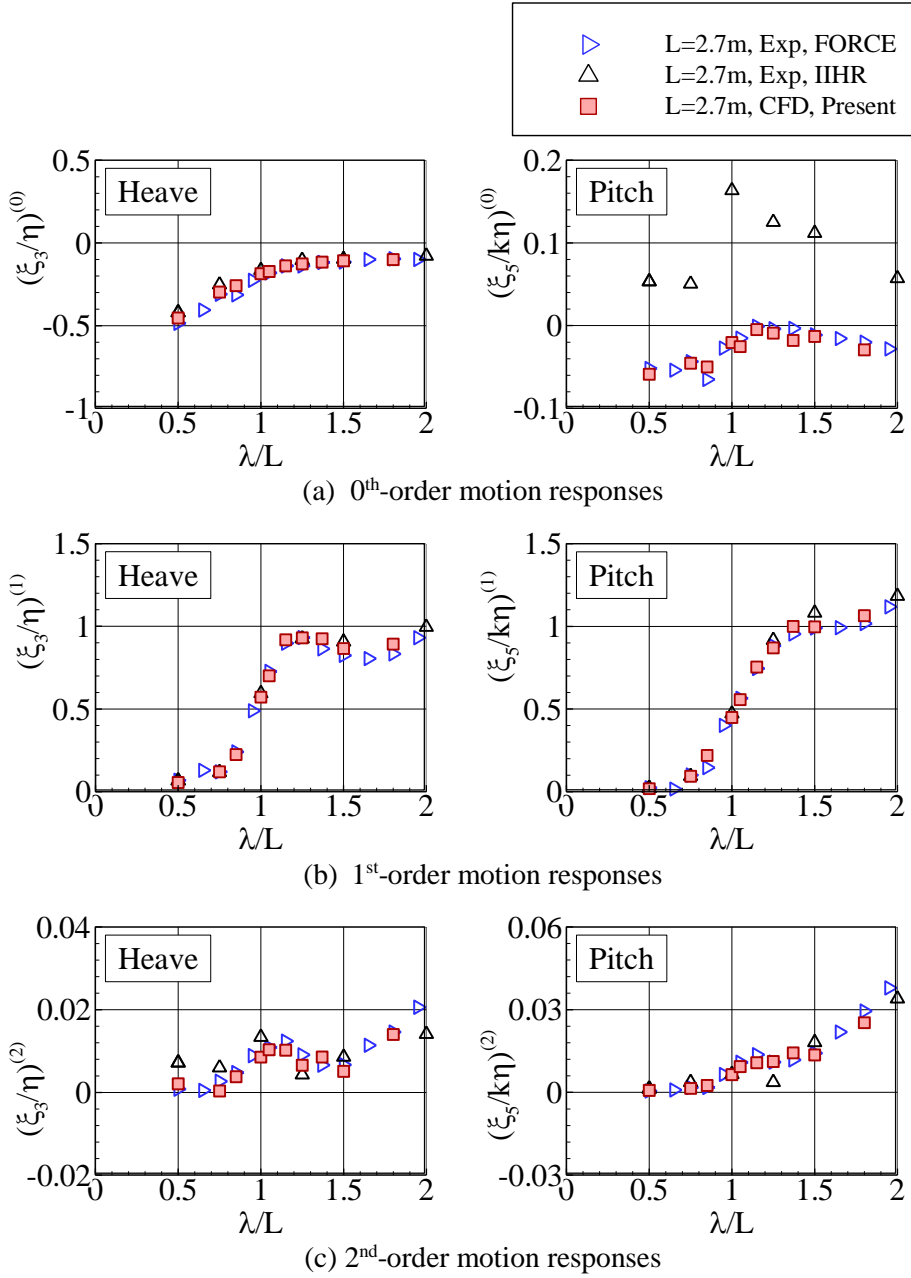


Fig. 5.9 Comparison of the motion responses w.r.t. wavelength

(Fn = 0.26, H/λ = 1/60)

For the 1st-order and 2nd-order motion responses, the results predicted by the present numerical solver generally agree well with that of the experiments. The peak of the 1st-order heave response locates near the resonance region, while the 1st-order pitch tends to converge as increasing wavelength. The 2nd-order motion responses have the similar tendency although the magnitudes are generally small. The 2nd-order heave motion has a high response at the resonance region, and the 2nd-order pitch motion has a gradually increasing tendency.

Fig. 5.10 summarizes the added resistance under different wavelengths. The peak added resistance is observed near the resonance region, nearly $\lambda/L = 1.15$. The peak value of added resistance is about 10 for the current cases that have a high Fn condition. The normalized values of added resistance are very small in the short waves or the long waves.

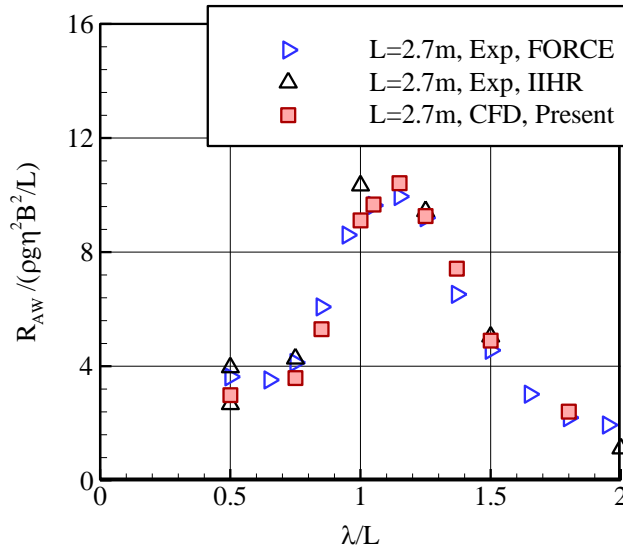


Fig. 5.10 Comparison of the added resistance w.r.t. wavelength
(Fn = 0.26, $H/\lambda = 1/60$)

5.2.2 Wave direction effect

The tests of this part involved the wave directions varying from head sea to the following sea. Constant wavelength of $\lambda/L=1.0$ and constant wave slope of $H/\lambda = 1/60$ were used for both the present computations and the other tests. The ship was allowed to be free in heave, roll, and pitch. The comparison data includes the experimental work by the IIHR institute (**Stocker, 2016**), the numerical results by the IIHR's in-house CFD program (**Sadat-Hosseini, et al., 2015**), and the numerical results by a SWENSE (Spectral Wave Explicit Navier-Stokes Equations) solver (**Vukcevic and Jasak, 2016**).

Fig. 5.11 compares the motion responses predicted under various wave directions. The comparison contains the mean and the 1st-order responses of the wave-induced heave, roll, and pitch.

For the mean heave response, the numerical methods provided negative values which means the downwards sinkage of ship. By comparison, the experimental measurement shows an upward sinkage at the beam sea and stern quartering sea condition.

For the roll motion, the mean heel angle is small in the bow quartering sea because the wave encounter frequency is far from the ship natural roll frequency. The mean heel angle is also small in the beam sea, because the waves of ship length have an insignificant effect on the ship lateral surface. This phenomenon in beam sea will be explained later in Fig. 5.15. Besides, a large discrepancy in the mean heel angle is found at the stern quartering condition, the experimental test generates a positive heel angle while the two numerical methods provide a negative heel angle. The experimental result is hard to explain, but the numerical prediction can be explained by the free surface patterns and the surface distribution of wave added pressure which

will be given in Fig. 5.13 ~ 5.15. For the bow quartering waves, higher free surface elevation is observed on the port side (PS), and more positive added pressure is also observed on the port side. As a result, the bow quartering waves provide the ship a positive mean roll moment that induces a positive mean heel angle. But for the stern quartering sea case, more positive added pressure is observed on the starboard side (STBD) although the wave effect is very weak. This means the mean roll moment and the corresponding mean heel angle are caused to be negative.

The 1st-order amplitude of motion responses generally agree well between each data. The heave motion increases when the head waves become bow quartering waves or beam waves; the first-order heave amplitude becomes close to the wave amplitude, which means the ship is riding the incoming waves. In the beam sea, the wavelength ($\lambda/L = 1.0$) is much higher than the ship width so the ship naturally heaves along the waves' crest and trough. The pitch motion also increases at the bow quartering sea and it is almost zero at the beam sea. The roll motion is only significant at the stern quartering sea condition, as the wave encountering frequency becomes close to the natural roll frequency. For the following sea, ship motion responses are generally small.

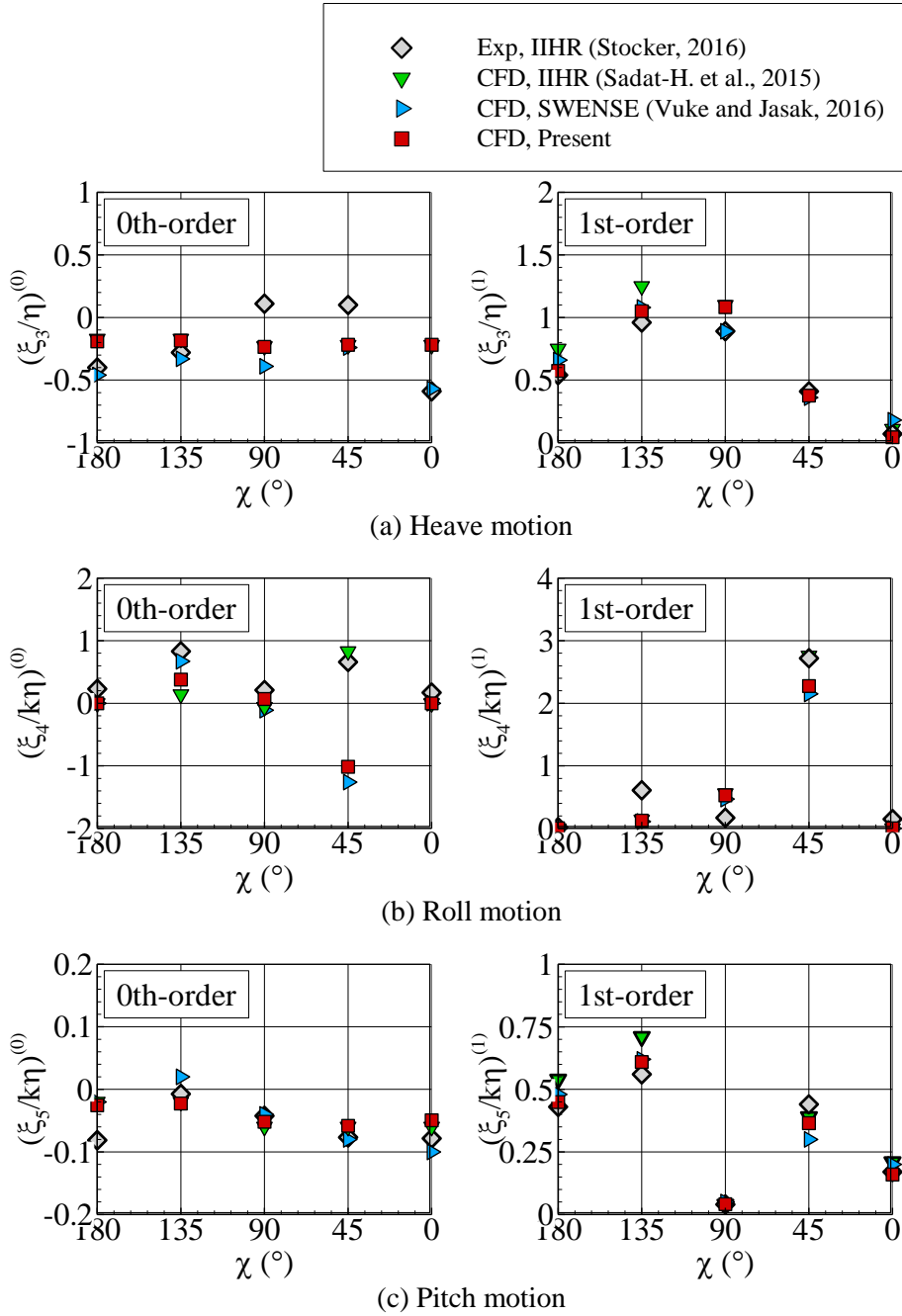


Fig. 5.11 Comparison of the motion responses w.r.t. wave direction
 ($F_n = 0.26$, $\lambda/L = 1.0$, $H/\lambda = 1/60$)

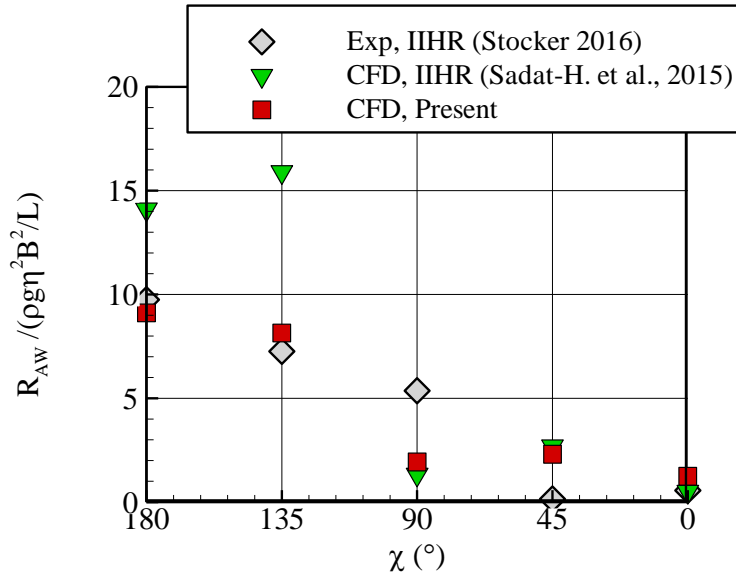


Fig. 5.12 Comparison of the added resistance w.r.t. wave direction
($F_n = 0.26$, $\lambda/L = 1.0$, $H/\lambda = 1/60$)

Fig. 5.12 compares the added resistance measured under various wave directions. In the bow waves, the CFD results of IIHR provide very high added resistance, and the corresponding heave and pitch responses are also high as shown in Fig. 5.11. The present CFD results are close to the experimental data in bow waves, while a discrepancy is found in the beam sea condition. The beam sea usually provides the ship with a very small added resistance if the wavelength is much higher than ship beam length. Because the ship is riding the beam waves and the pitch motion is negligible, providing little changes to the ship wetted surface. In the works (**Park et al., 2019; Lee et al., 2021; Seo et al., 2021**) that involve the seakeeping tests in various wave directions, it was also observed that the normalized added resistance at the beam sea condition is generally less than 3 for intermediate wavelength.

Meanwhile, the experimental work showed a typo for the added resistance of beam sea condition [see the C_T values of $\chi = 90^\circ$ condition in the Table 4.25 of **Stocker (2016)**]. Thus the computational results seem to be reasonable for the beam sea case.

Fig. 5.15 has summarized the surface distribution of wave added pressure under various wave directions. The added pressure p_{AW} is calculated by subtracting the pressures obtained in calm-sea and in waves. The added pressure is normalized by $\rho g A$, where the A is wave amplitude. Its distribution on the bow and two lateral sides is observed in the various figures.

For the current containership hull with a high Fn condition, the wave added pressure is mostly distributed beyond the design draft line, and no significant effect is observed on the stern. For the bow quartering wave case ($\chi = 135^\circ$), the distribution of added pressure is naturally asymmetric. For the beam sea case, the wave effect is very weak because the ship width is much shorter compared to the wavelength. For the case of stern quartering sea, the added pressure is found to be widely distributed along the hull, although the magnitude is not as strong as that of the bow wave conditions.

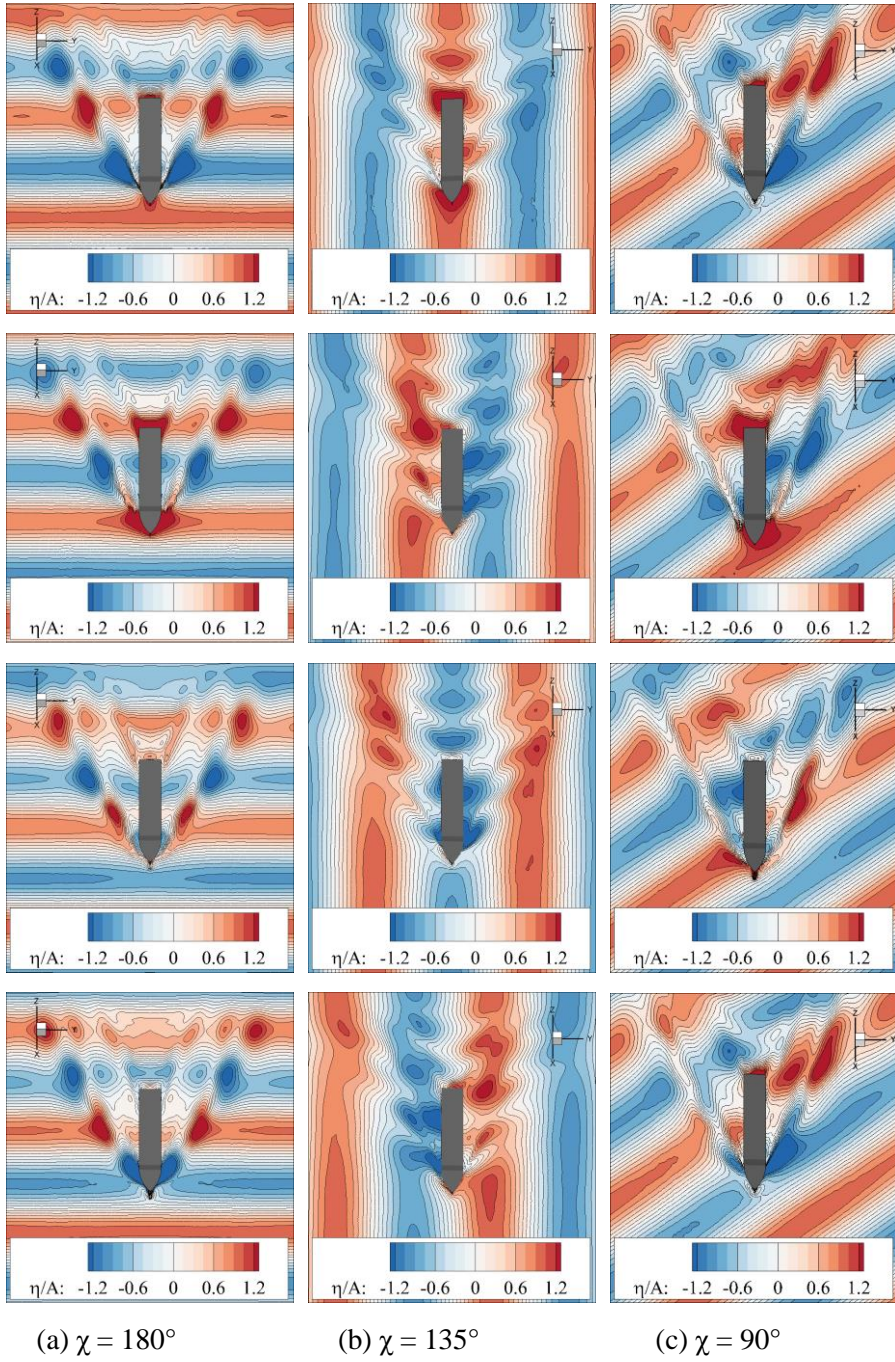


Fig. 5.13 Sequential wave patterns under different wave directions (a)

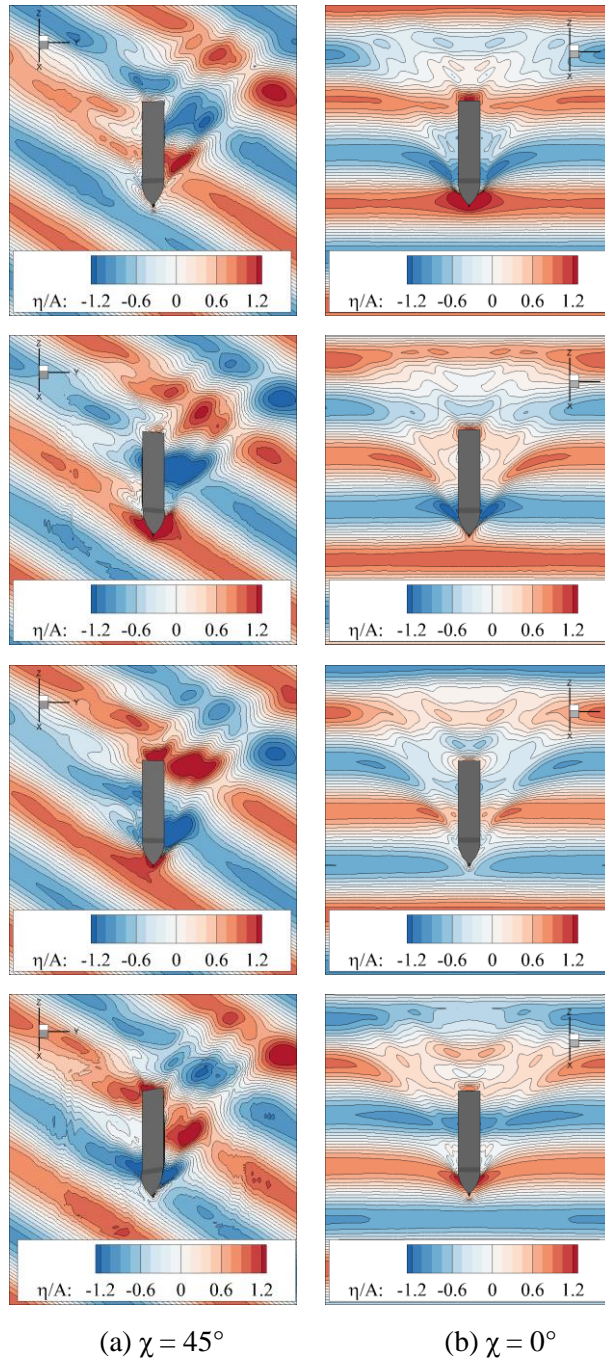
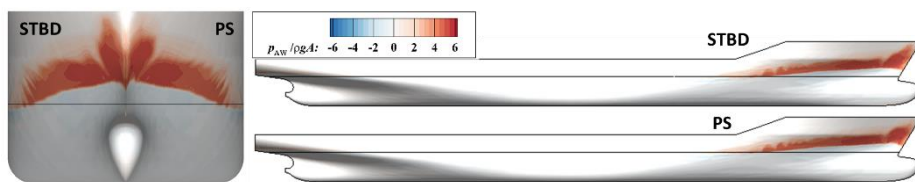
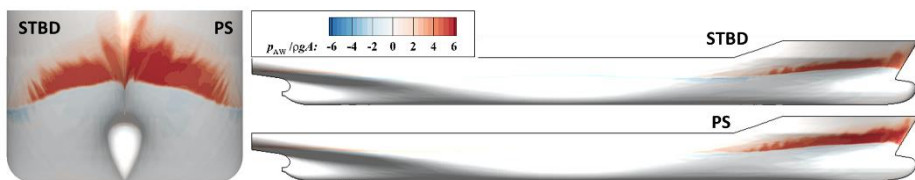


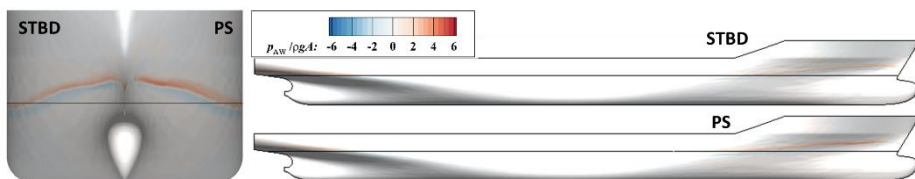
Fig. 5.14 Sequential wave patterns under different wave directions (b)



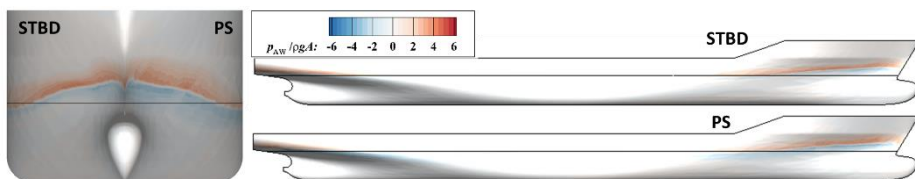
(a) $\chi = 180^\circ$, head sea



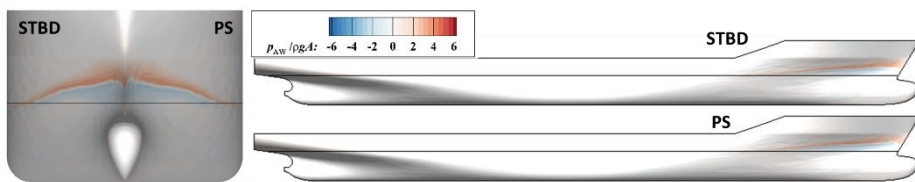
(b) $\chi = 135^\circ$, bow quartering sea



(c) $\chi = 90^\circ$, beam sea



(d) $\chi = 45^\circ$, stern quartering sea



(e) $\chi = 0^\circ$, following sea

Fig. 5.15 Surface distribution of added pressure under different wave directions

6. Numerical PMM Tests in Waves

To investigate the wave effect on the PMM tests and corresponding manoeuvring coefficients, this study has involved three wave parameters: wave frequency, wave slope, and wave direction. The static drift test and the pure yaw test that determine the manoeuvring coefficients of sway velocity and yaw rate were selected as the study cases.

The wave added forces and moment are introduced under various PMM motion conditions. Eq. (6.1) specifies the added surge force $X_{AW}^{(0)'}$, added sway force $Y_{AW}^{(0)'}$, and added yaw moment $N_{AW}^{(0)'}$ for the static drift test, and the mean components of force/moment are considered. Eq. (6.2) specifies the added sway force $Y_{AW}^{(1,\sin)'}$, and added yaw moment $N_{AW}^{(1,\sin)'}$ for the pure yaw test, and the sine component related to the prescribed yaw rate is considered.

$$X_{AW}^{(0)'} = \frac{\Delta X^{(0)}}{\rho g A^2 B^2 / L} = \frac{X_{\text{wave}}^{(0)} - X_{\text{calm}}^{(0)}}{\rho g A^2 B^2 / L} \quad (6.1\text{-a})$$

$$Y_{AW}^{(0)'} = \frac{\Delta Y^{(0)}}{\rho g A^2 B^2 / L} = \frac{Y_{\text{wave}}^{(0)} - Y_{\text{calm}}^{(0)}}{\rho g A^2 B^2 / L} \quad (6.1\text{-b})$$

$$N_{AW}^{(0)'} = \frac{\Delta N^{(0)}}{\rho g A^2 B^2} = \frac{N_{\text{wave}}^{(0)} - N_{\text{calm}}^{(0)}}{\rho g A^2 B^2} \quad (6.1\text{-c})$$

$$Y_{AW}^{(1,\sin)'} = \frac{\Delta Y^{(0)}}{\rho g A^2 B^2 / L} = \frac{Y_{\text{wave}}^{(1,\sin)} - Y_{\text{calm}}^{(1,\sin)}}{\rho g A^2 B^2 / L} \quad (6.2\text{-a})$$

$$N_{AW}^{(1,\sin)'} = \frac{\Delta N^{(0)}}{\rho g A^2 B^2} = \frac{N_{\text{wave}}^{(1,\sin)} - N_{\text{calm}}^{(1,\sin)}}{\rho g A^2 B^2} \quad (6.2\text{-b})$$

6.1 Wave frequency effect

This part investigated the wave frequency effect on PMM tests, and the wave frequency is represented by wavelength. Based on the constant wave slope $H/\lambda = 1/60$ and the wave direction $\chi = 180^\circ$, three typical wavelengths have been considered, namely $\lambda/L = 0.5, 1.0, 1.5$.

6.1.1 Static drift test

Firstly, a typical static drift case (drift angle $\beta_0 = 18^\circ$) was used to observe the hydrodynamic characteristics under various wavelengths. Fig. 6.1–6.3 presented the sequential development of wave pattern and surface pressure distribution for each wavelength condition. The sequential interval is $0.25T_e$, and the dynamic pressure is normalized by ship total speed U_0 . The ship trim attitude can be observed with respect to the reference line $z_0 = 0$.

The effect of short waves is mainly focused on the bow region, while the effect of long waves is distributed along with the hull. Particularly, the port side of bow is the location where the high pressure is caused by the static drift motion. The nonlinear phenomena of long waves are very prominent. The bow becomes exposed and the waterline is more nonlinear during the pitch motion.

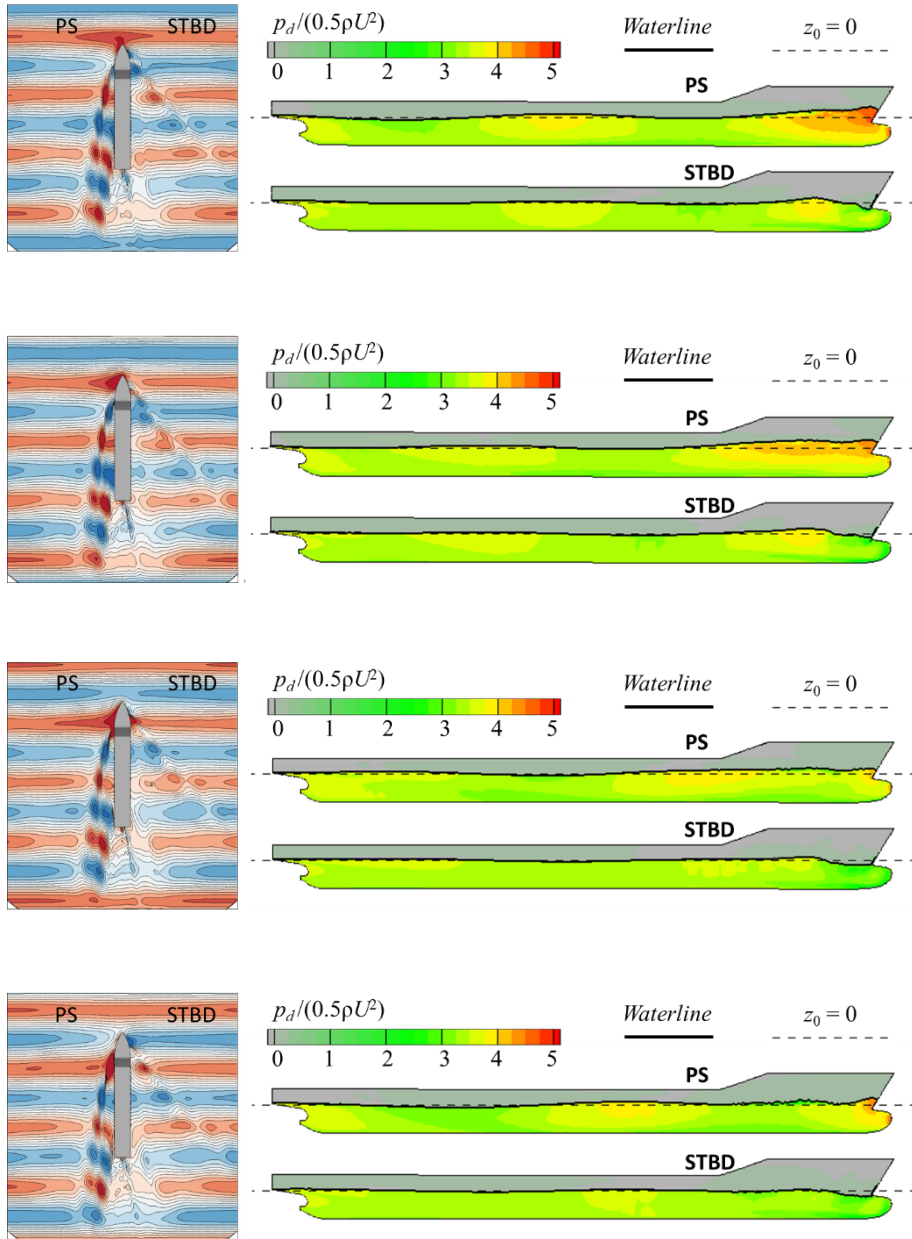


Fig. 6.1 Sequential development of wave pattern and hull dynamic pressure
(static drift test $\beta_0 = 18^\circ$, $\lambda/L = 0.5$, sequential interval $0.25T_e$)

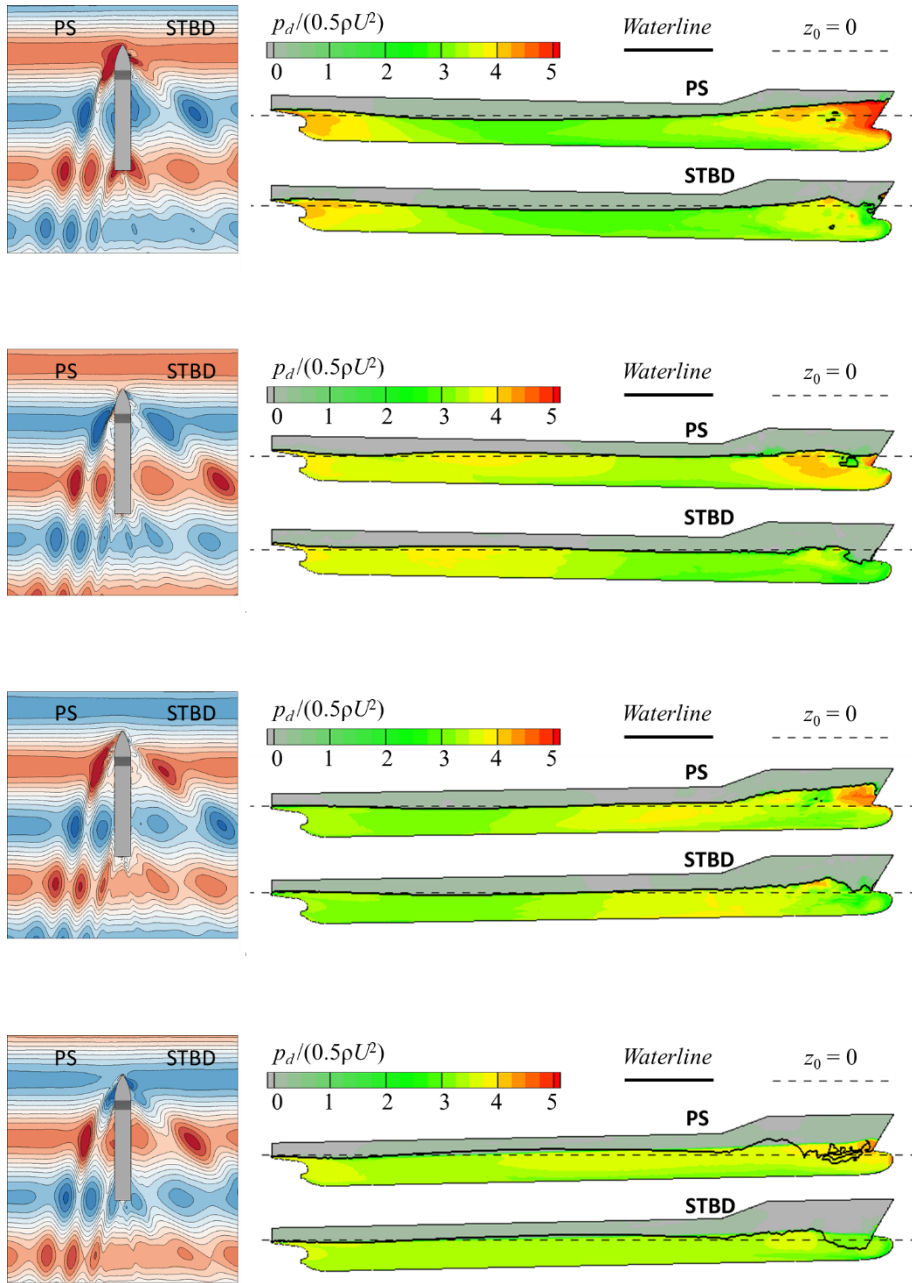


Fig. 6.2 Sequential development of wave pattern and hull dynamic pressure
(static drift test $\beta_0 = 18^\circ$, $\lambda/L = 1.0$, sequential interval $0.25 T_e$)

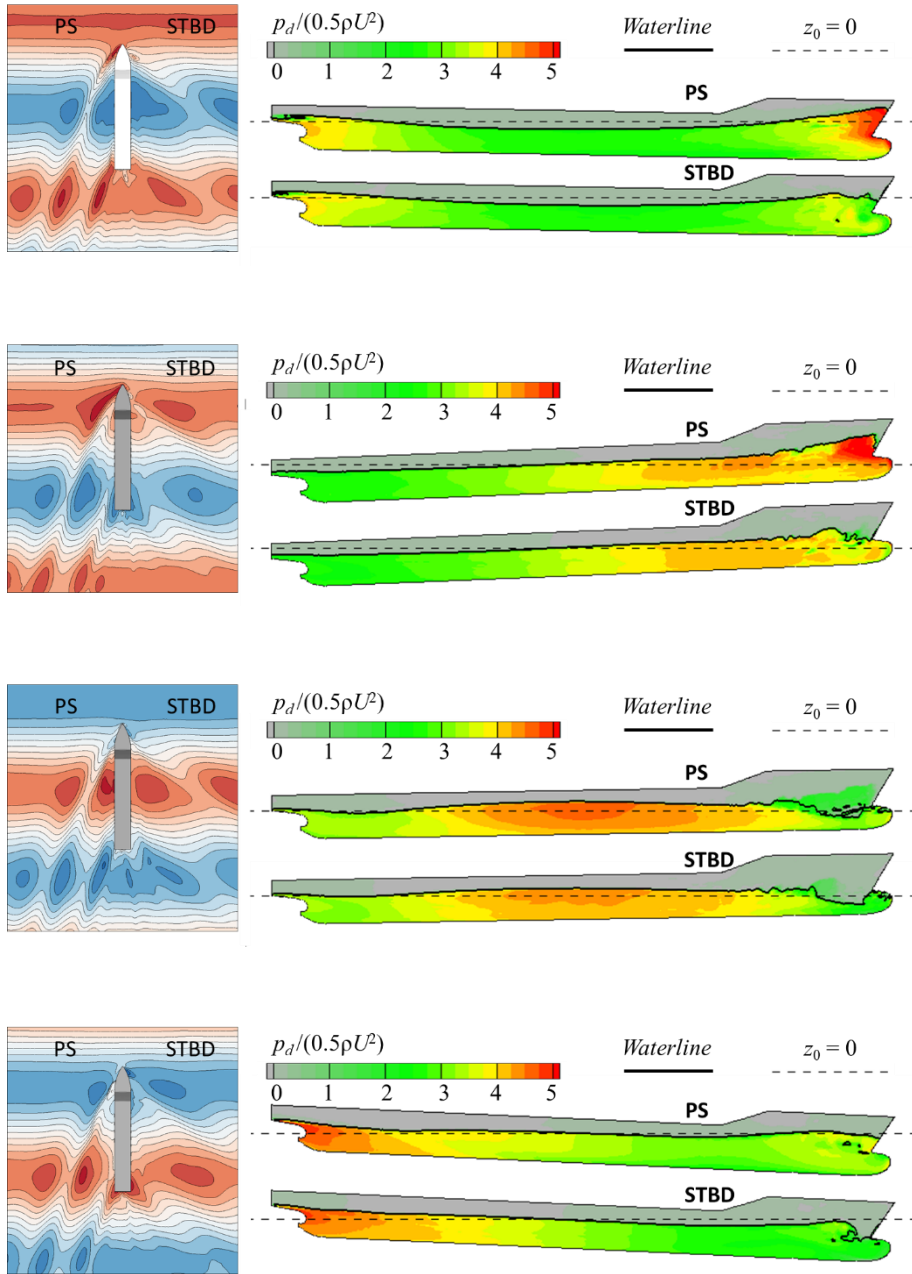


Fig. 6.3 Sequential development of wave pattern and hull dynamic pressure
(static drift test $\beta_0 = 18^\circ$, $\lambda/L = 1.5$, sequential interval $0.25T_e$)

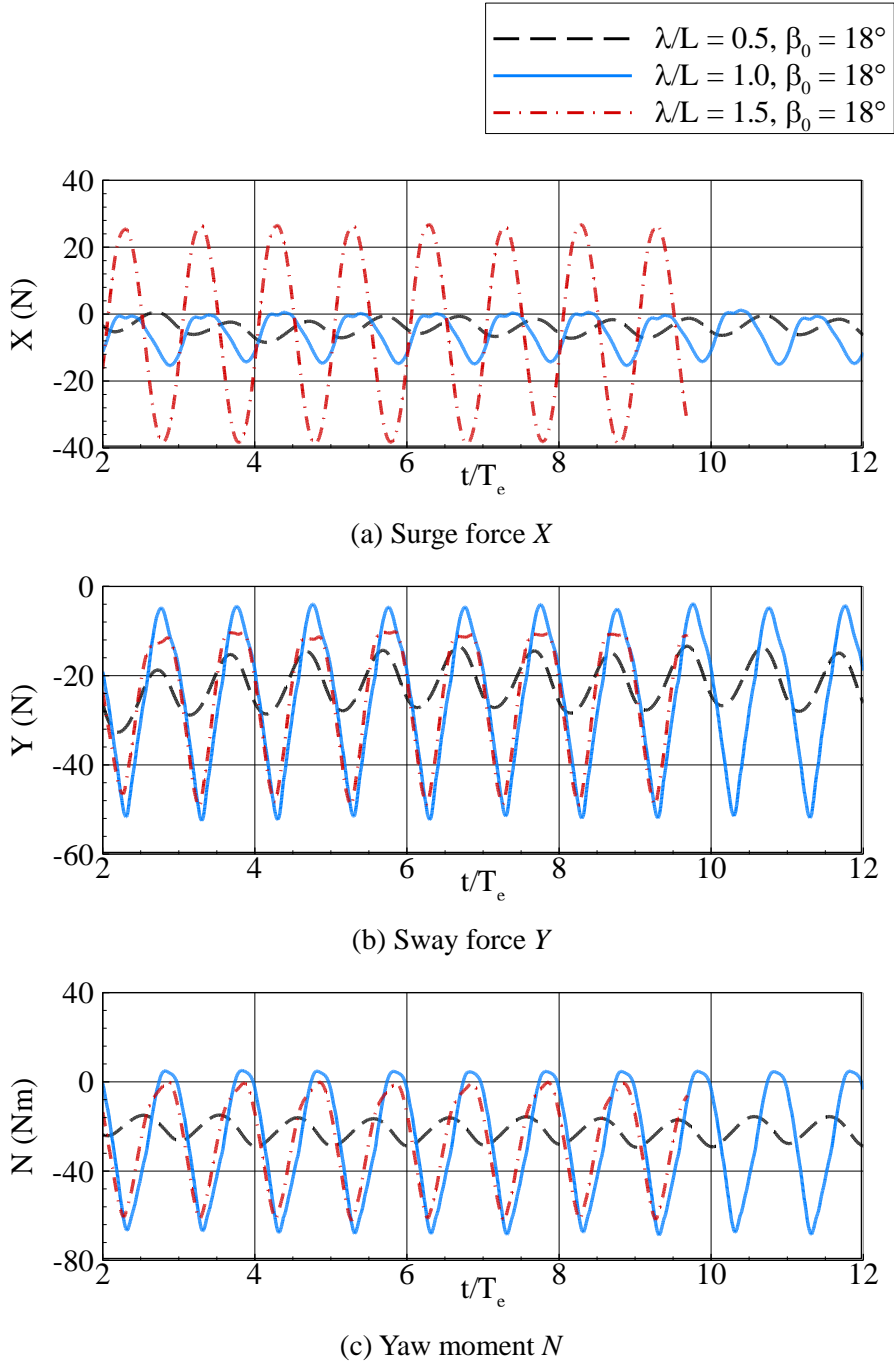


Fig. 6.4 Force/moment signals under different wavelengths, $\beta_0 = 18^\circ$

Fig. 6.4 shows the time history of body forces and moments obtained under different wavelengths. The surge force mainly focuses on the bow region, so higher wave amplitude usually provides the larger amplitude of surge force. However, for the sway force and yaw moment that is dominated by the pressure on the ship lateral surface, the wave elevations on both bow and stern act important roles. The amplitude of sway force or yaw moment is determined not only by the amplitude of incoming waves but also by the hull shape (particularly the shape of bow and stern). Thus, the present hull shape causes the phenomenon that the long wavelength case ($\lambda/L = 1.5$) has a smaller amplitude than that of the intermediate wavelength case ($\lambda/L = 1.0$).

Fig. 6.5 and 6.6 present the wave-induced motion RAOs and added forces at various drift conditions and different wavelengths. For the motion RAOs shown in Fig. 6.5, both the heave and pitch motions are less sensitive to the static drift condition. The static drift condition caused a very minor difference in the motion responses under each wavelength, it is because the wave encountering speed is slightly changed by the different drift angles.

Generally, as the wavelength increases, the heave RAO increases but it is far below the value 1. This is due to the Fn number. The design Fn number is 0.26 (see Section 5.2), but this series of tests uses the Fn of 0.16. Such tendency can also be observed in the work of **Nakamura and Naito (1977)** that an S-175 containership model is used to investigate the Fn effect on the ship motion in waves.

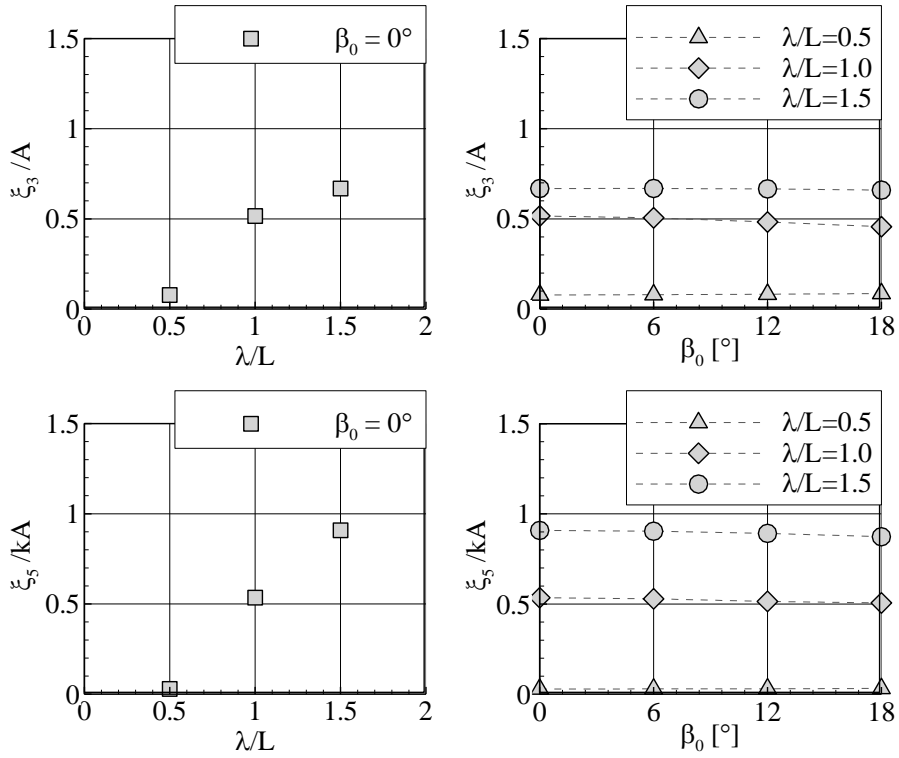


Fig. 6.5 Ship motion RAOs w.r.t. wavelengths and drift angles

Fig. 6.6 presents the added surge force, added sway force, and added yaw moment measured with respect to wavelength. The peak added force/moment occurs at the intermediate wavelength condition. The drift angle provides a significant effect on the added sway force and the added yaw moment. Actually, an almost linear relationship can be observed between the drift angle and the added sway force or added yaw moment, as shown in Fig. 6.7. Besides, it can be noted that the short wave case has provided significant added sway force at the large static drift condition.

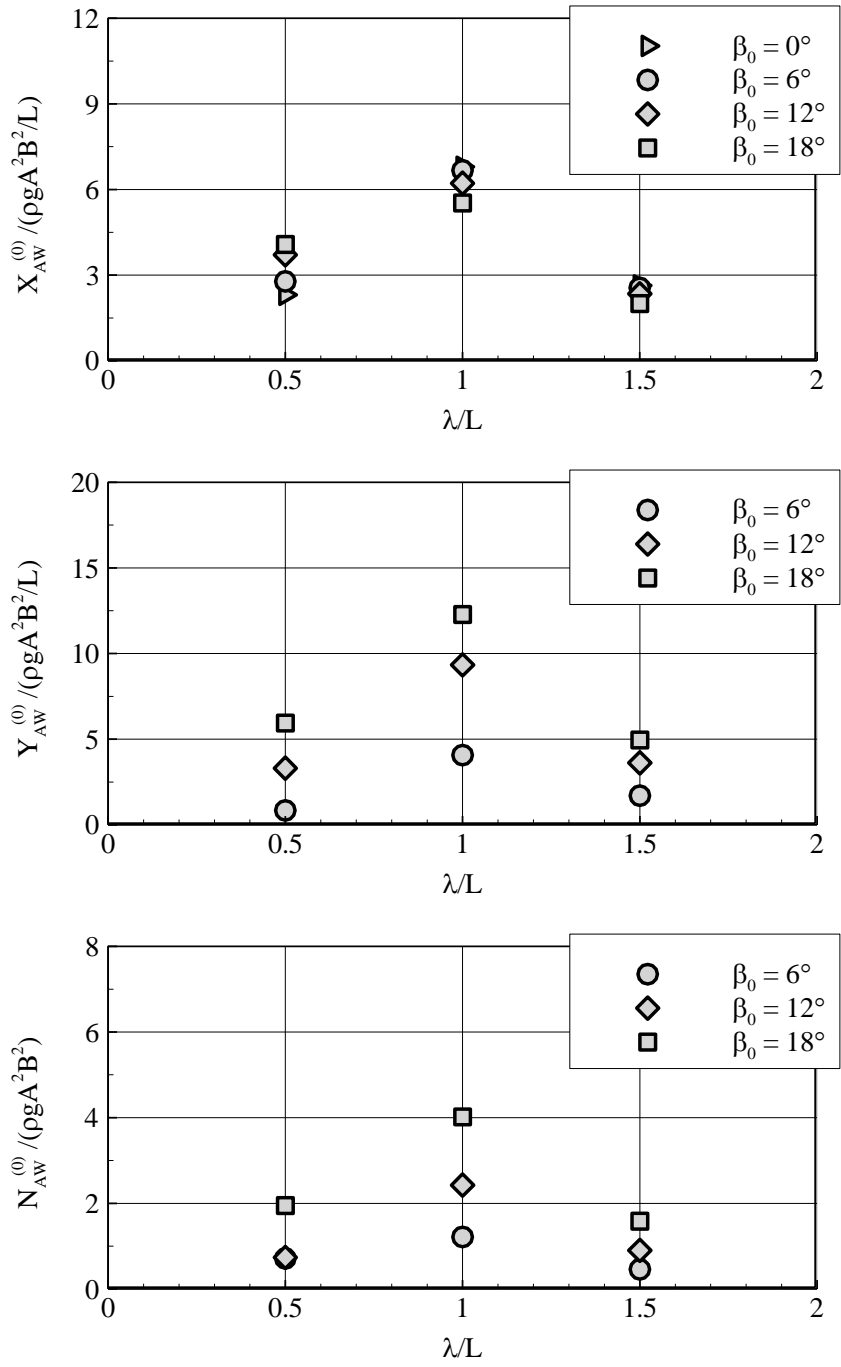


Fig. 6.6 Added forces and moment w.r.t. wavelengths

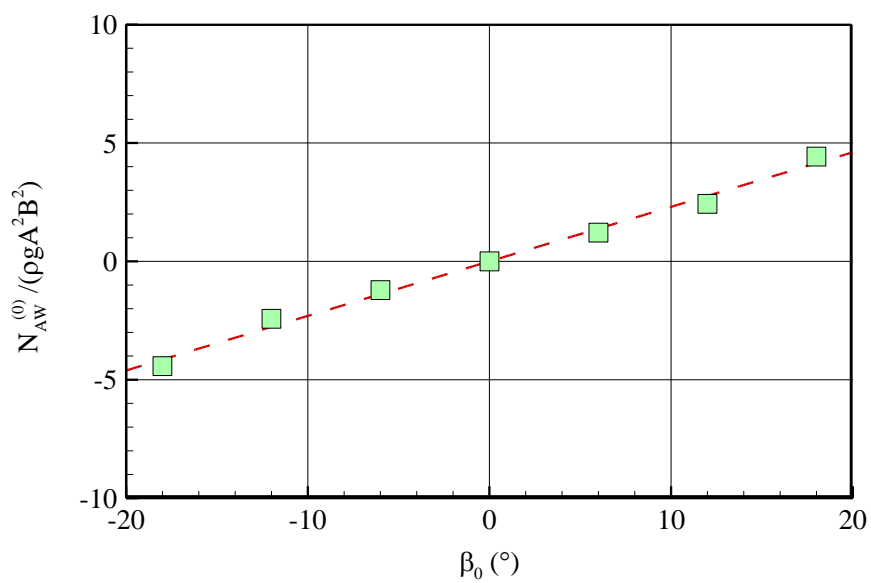
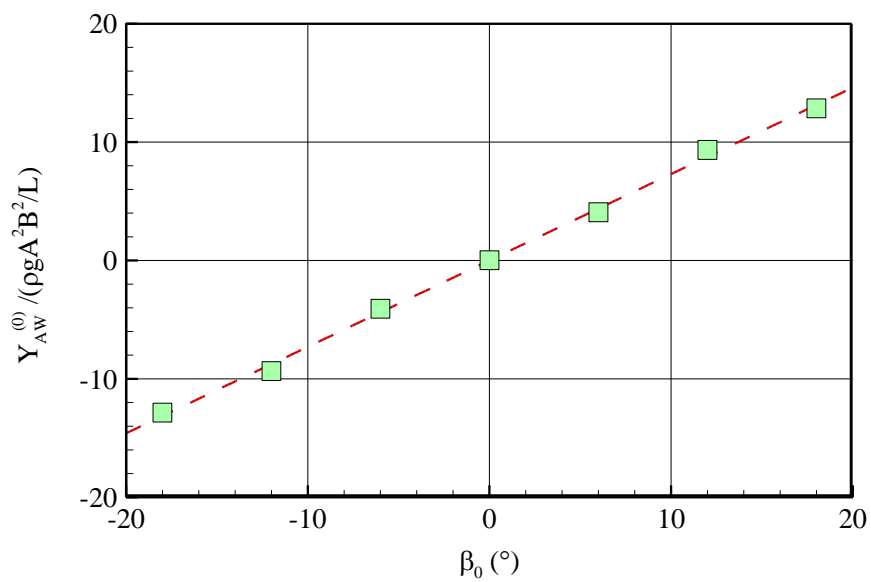


Fig. 6.7 Relation between added force/moment and drift angle
 $(\beta_0 = 18^\circ, \lambda/L = 1.0)$

Fig. 6.8 summarizes the manoeuvring coefficients obtained under different wavelengths, the case $\lambda/L = 0$ indicates the calm-sea result. Two coefficients Y_v and N_v that represent the derivatives of sway force and yaw moment with respect to sway velocity are observed. Under the current head sea and constant wave slope condition, the short wave ($\lambda/L = 0.5$) case provided a very limited change to the coefficients because the wave contribution on total force/moment is not that significant. By comparison, the long waves ($\lambda/L = 1.5$) that have higher wave amplitude changed the coefficients significantly although the normalized added forces and moment are small.

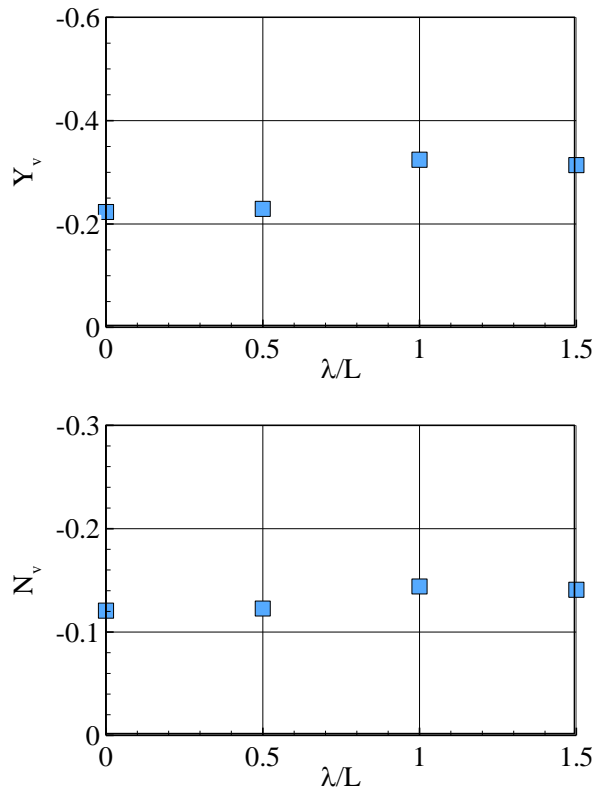


Fig. 6.8 Wavelength effect on the coefficients Y_v and N_v

6.1.2 Pure yaw test

Different from the static drift tests, the pure yaw test provides the ship with a dynamic yawing rate interacting with the incoming waves. Meanwhile, the dynamic ship orientation relative to the wave incoming direction can induce the oblique wave effect that affects the wave-induced ship motion responses as well as body forces. This oblique wave effect will be discussed in Section 6.3.

One main concern of dynamic PMM tests in waves is the memory effect of flow development. It is difficult to quantify and minimize the memory effect by using an analytic solution. Present work chose to observe the potential memory effect of flow development by examining the wave patterns and vorticity field. The hydrodynamic characteristics of the pure yaw test in waves were presented using the case $r_0' = 0.5$. Figs. 6.9 and 6.10 present the sequential development of wave pattern and vorticity field at three yawing motion stages. The first stage is near the instant when the ship has the maximum yaw angle but zero yaw rate. The wave shows a stable development and the vorticity near hull is very mild, because there is no yawing motion at this stage. At the second stage when the ship has the maximum yaw rate, the ship heading direction has a slight change but the wave development is still stable enough. It can be seen that the wave pattern and vorticity field remain similar after one encountering wave period T_e . In the third stage, the wave patterns and vorticity fields are symmetric to that of the first stage. These observations indicate that the potential memory effect of flow development is not that significant.

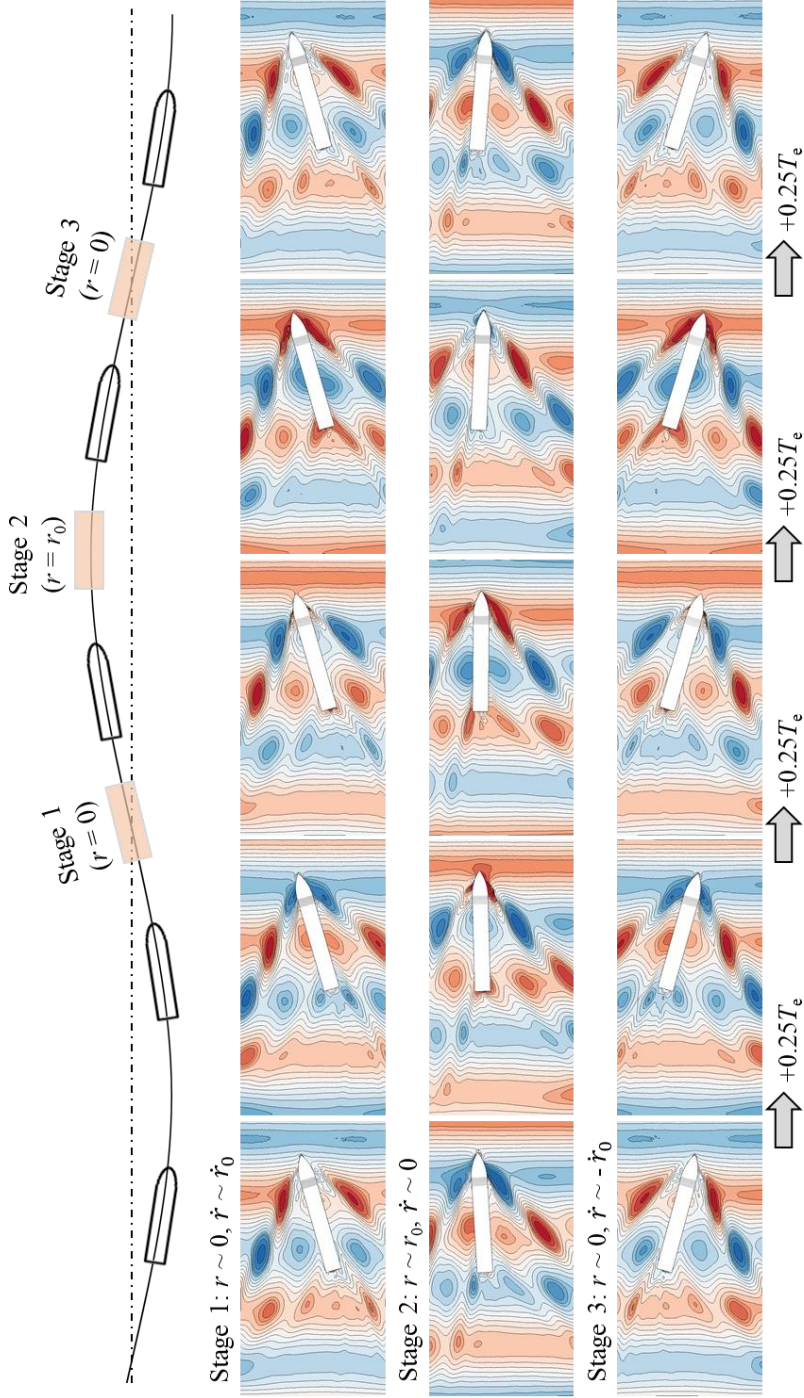


Fig. 6.9 Sequential wave pattern of the pure yaw test in waves

($r_0' = 0.5, \lambda/L = 1.0, H/\lambda = 1/60, \chi = 180^\circ$)

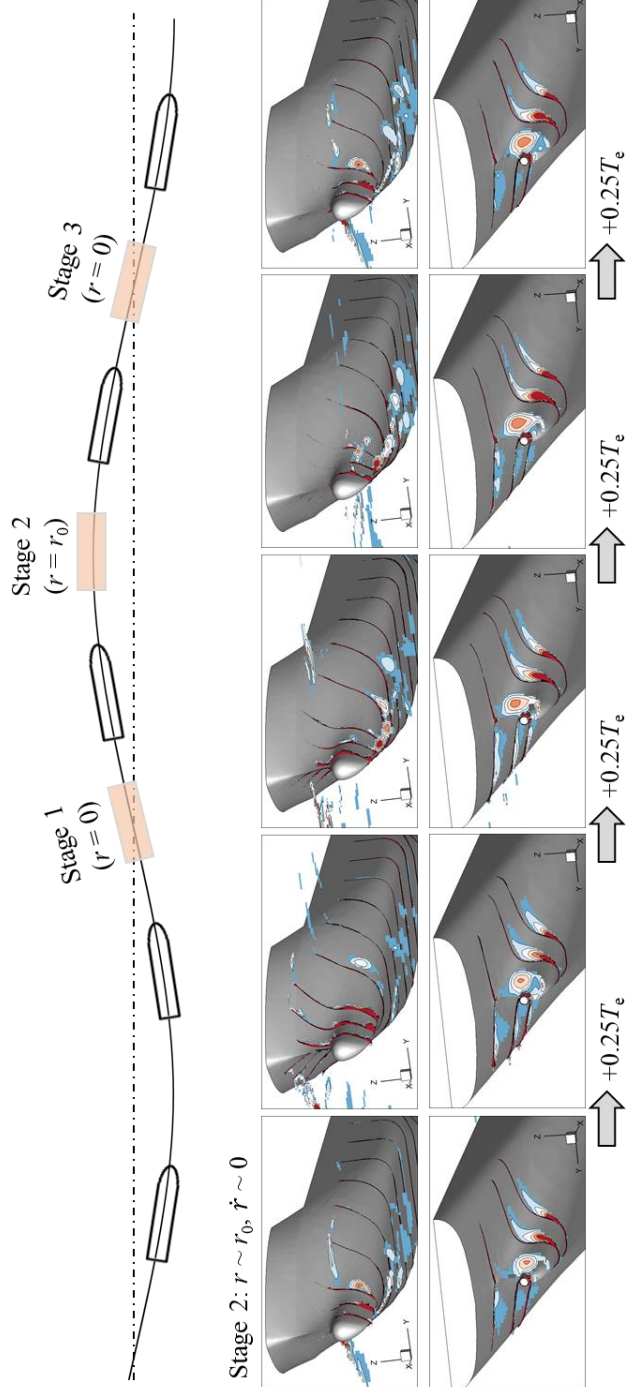


Fig. 6.10 Sequential vorticity field of the pure yaw test in waves

$$(r_0' = 0.5, \lambda/L = 1.0, H/\lambda = 1/60, \chi = 180^\circ)$$

Fig. 6.11 presents the time history of body yaw moment measured in the pure yaw test in waves. The sway force is too weak for yawing motion so it is not discussed. The time history of yaw angle is also added in the figures. The yaw angle has a cosine function and its corresponding yaw rate has a sine function, which means the ship has the maximum yaw rate when the yaw angle is zero. For each wavelength case, the amplitudes of the yaw moment become high at the turning stage when the ship arrives at the maximum yaw rate (e.g. the instant $t/T_0 = 0.25, 0.75$). Compared with the intermediate wavelength case ($\lambda/L = 1.0$), the long wavelength case has smaller amplitudes of sway force and yaw moment. This tendency is similar to what was observed from the static drift test in waves.

To observe the wave mean contribution in each wave encountering period, the running average with the interval of wave encountering period is performed to the yaw moment signal, as shown in Fig. 6.11. It can be observed that the wave contribution mainly occurs at the turning stage, namely the stage that the ship reaches the prescribed yaw rate as well as the desired heading direction. Meanwhile, the wave mean effect is negligible when the ship yaw rate approaches zero and the ship heading direction changes. So the ship's dynamic orientation with respect to the incoming wave direction is not a critical issue.

Fig. 6.12 summarizes the added force/moment with respect to the wavelength. The general tendency is very similar to that observed in the previous static drift test. The peak values of both the added sway force and added yaw moment are observed in the intermediate wave cases. But the magnitudes are much less than that observed in the static drift test.

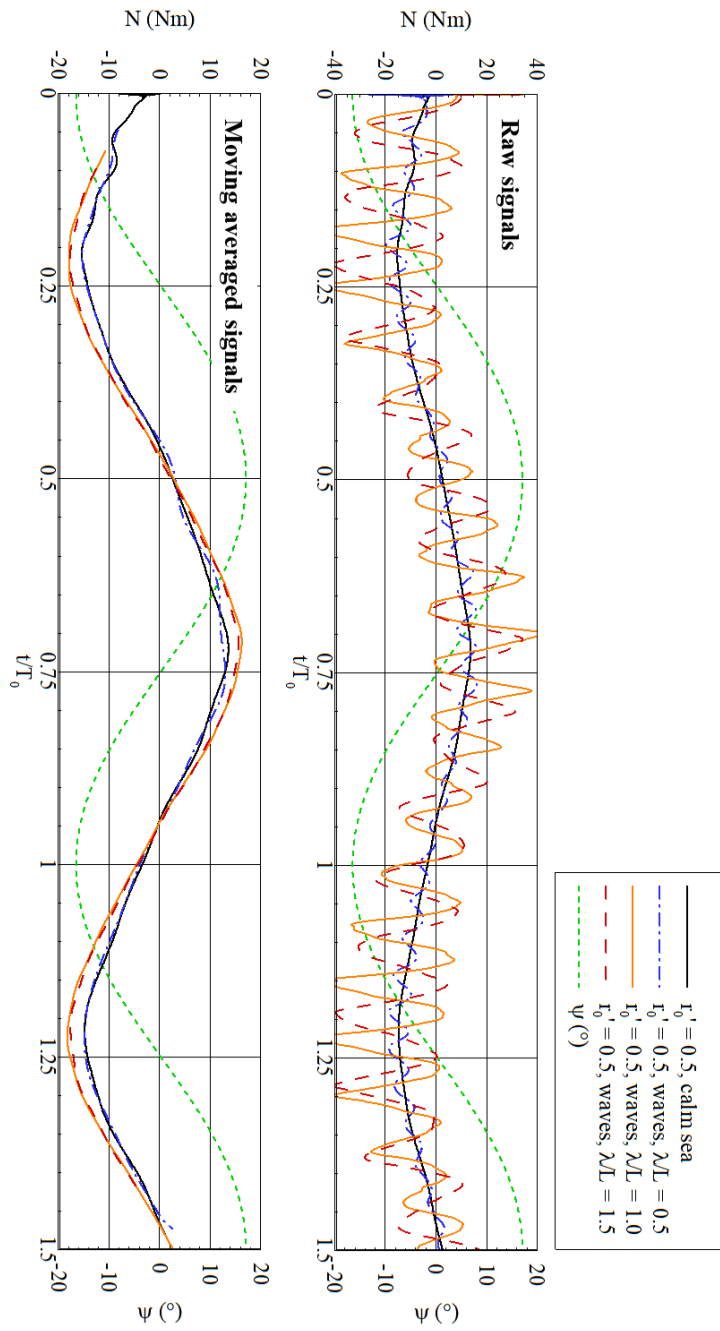


Fig. 6.11 Force/moment signals under different wavelengths, $r_0' = 0.5$

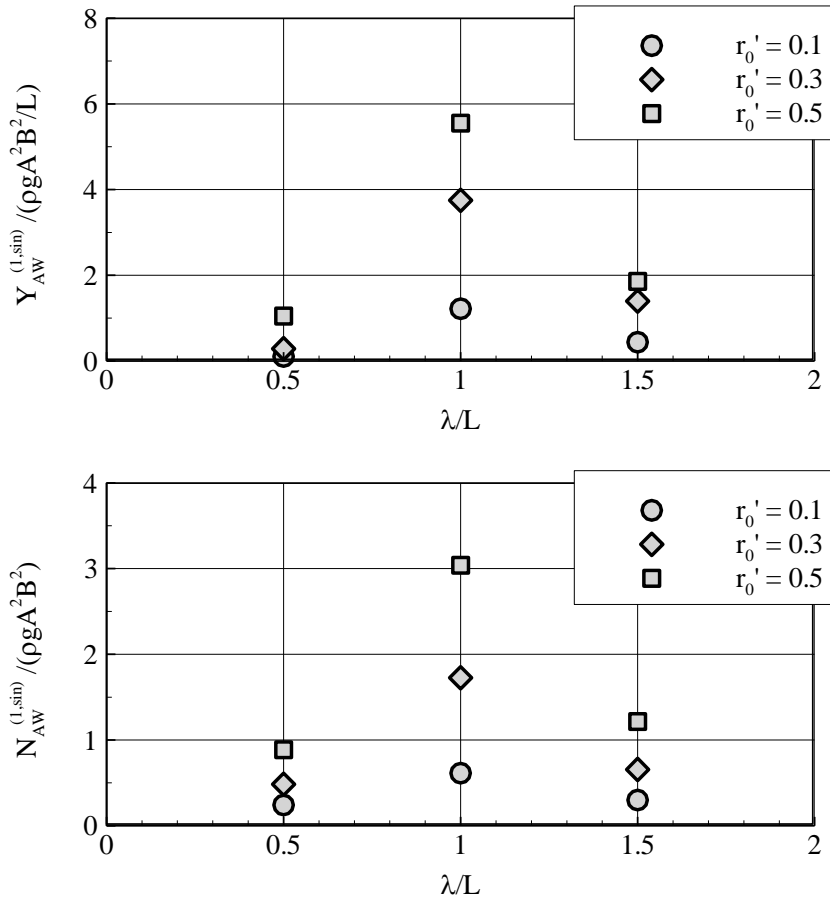


Fig. 6.12 Added forces and moment w.r.t. wavelengths

Meanwhile, the short wave condition has provided a very limited effect on the manoeuvring coefficients of yaw rate, while the two longer wave cases have improved the coefficients by nearly 50%, as shown in Fig. 6.13. Unlike most manoeuvring coefficients that have negative values, the coefficient Y_r is positive under the calm-sea condition. The physical interpretation of positive Y_r is that the sway force of hull acts towards the center of ship turning motion. But in waves, the waves mainly act on the ship bow, providing a sway force in the opposite direction of bow's turning direct. As a result, the total sway force

of hull becomes negative in waves, and negative Y_r is observed in Fig. 6.13.

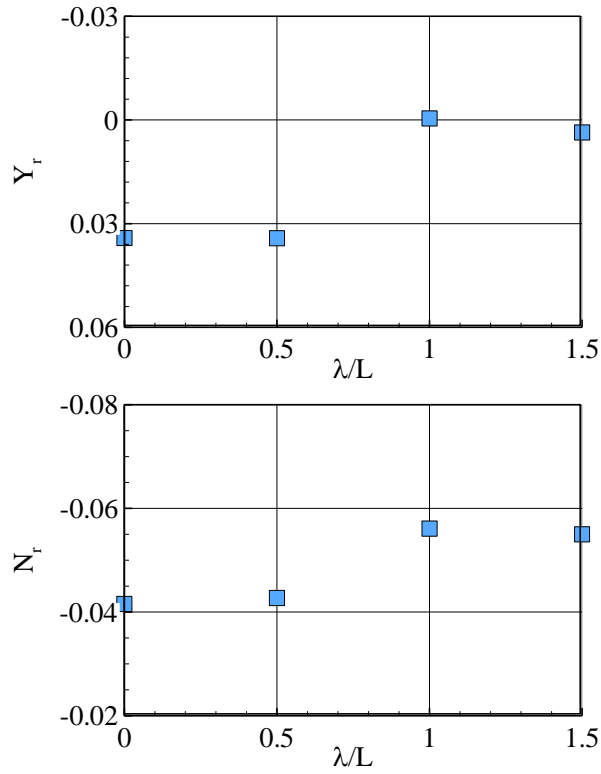


Fig. 6.13 Wavelength effect on the coefficients Y_r and N_r

6.2 Wave slope effect

Considering the high curvature of the present containership model and the challenging wave field of adverse weather, the wave slope effect was investigated for the ship PMM tests and corresponding manoeuvring coefficients.

Based on the wavelength $\lambda/L = 1$ and the wave direction $\chi = 180^\circ$ (head sea), this section has observed three wave slope conditions, namely $H/\lambda = 1/30$, $1/60$, $1/90$. Fig. 6.14 presents the nominal waterlines under different wave slope conditions and their interaction with the body plan. The $H/\lambda = 1/30$ shows a high variation of waterlines, especially near the bulbous bow.

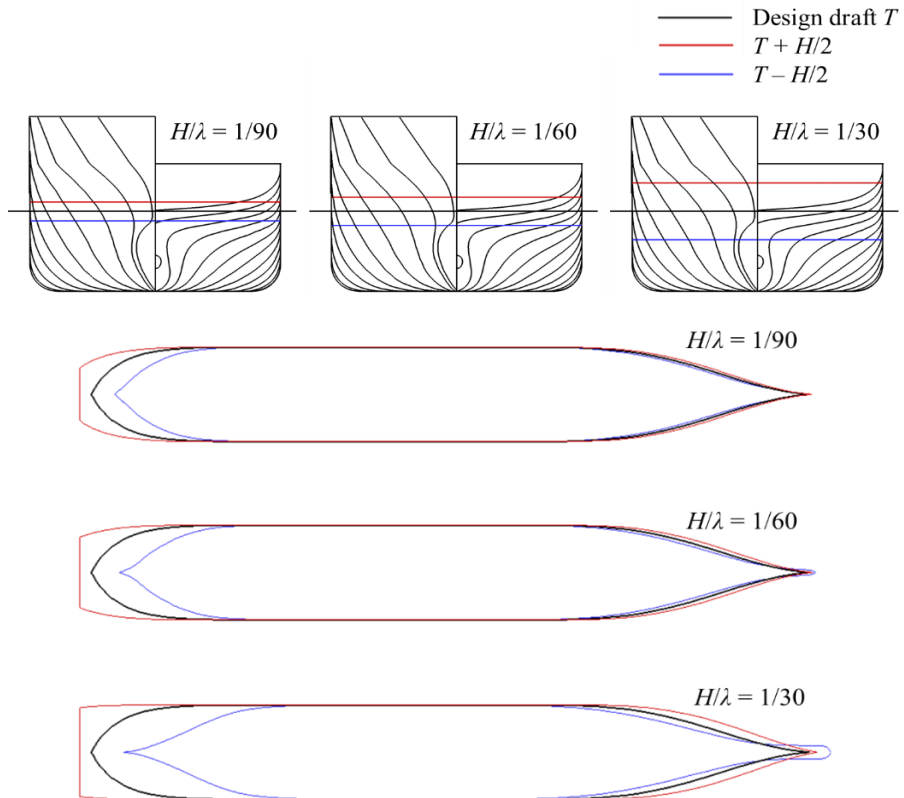


Fig. 6.14 Ship waterlines under different wave slopes

Both the static drift test and the pure yaw test were selected to estimate the wave slope effect on the corresponding coefficients. The sequential development of wave pattern and the distribution of wave added pressure were presented, and the time history of wave-induced ship motion and body forces were also compared to observe the nonlinear phenomena caused by wave slope conditions. The mean, linear, and quadratic components of wave excitation forces and wave-induced motion were summarized with respect to the wave slopes for a detailed understanding of the wave slope effect

6.2.1 Static drift test

Firstly, the static drift case of 18° drift angle was tested to observe the wave slope effect on the sequential development of body forces and flow fields.

Fig. 6.15 presents the time histories of body surge force, sway force, and yaw moment with respect to the wave slope. The absolute values of force/moment are presented so that the nonlinear phenomena can be observed more directly. The time history of ship dynamic trim τ (pitch motion) is also added in the figures, the positive trim indicates the bow-up.

By Fig. 6.15, it can be observed that the wave exciting forces and moment are non-harmonic and the increasing wave slope has induced more strong nonlinearity. At the instant of bow-up, namely the positive trim attitude, the signal of surge force becomes flat or even reduced because the bow is coming out of the water. The wave patterns can be found in Fig. 6.16, it can be seen that the bulbous bow already come out of the water under the highest wave slope case. At the instant of bow-down, namely the negative trim attitude, the surge force has increased because the bow starts to submerge into the water.

For the nonlinearity of sway force and yaw moment, both the bow and stern act important roles. The bow-up also means the stern-down, so the

longitudinal distribution of pressure is highly dependent on the hull shape. As seen in Fig. 6.15, the highly nonlinearity is also observed in the highest wave slope case.

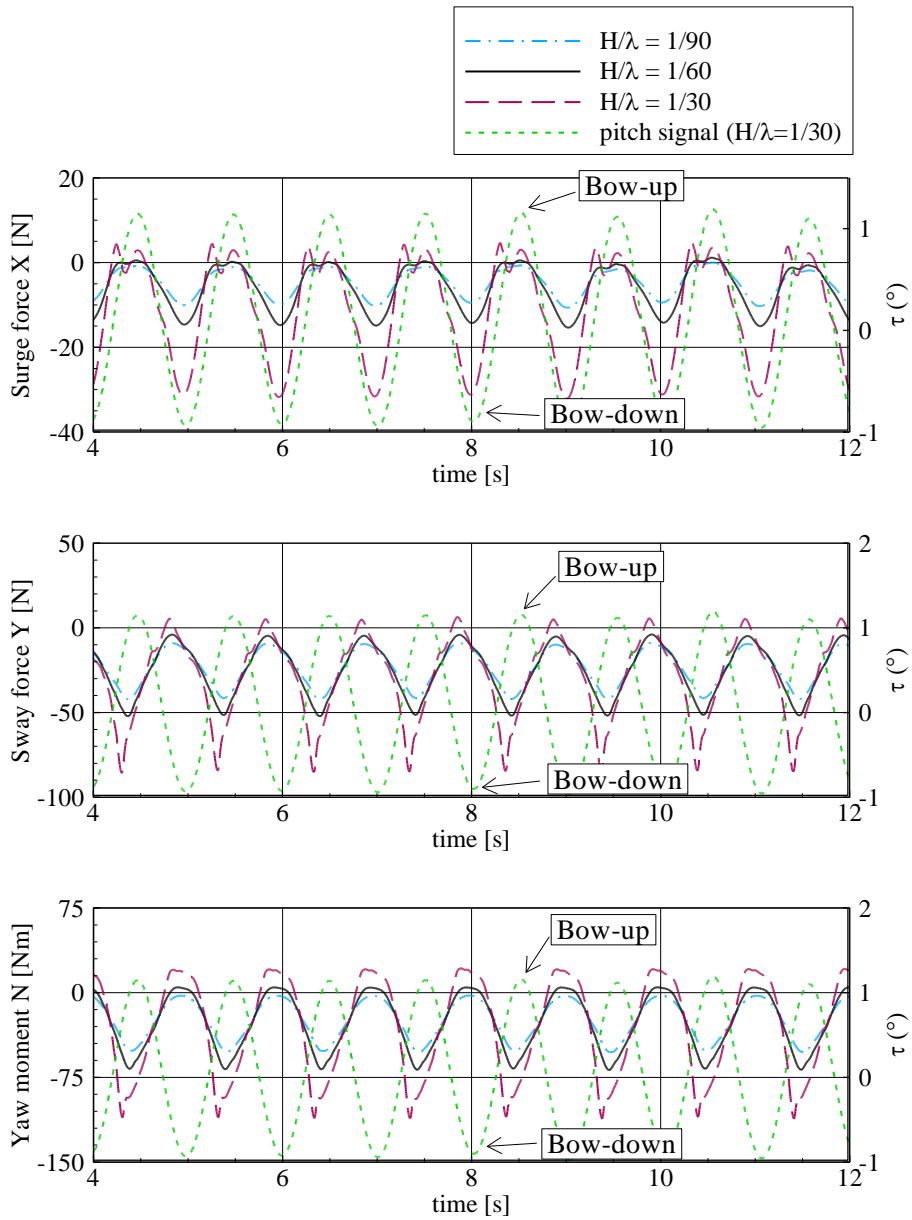


Fig. 6.15 Force/moment signals under different wave slopes, $\beta_0 = 18^\circ$

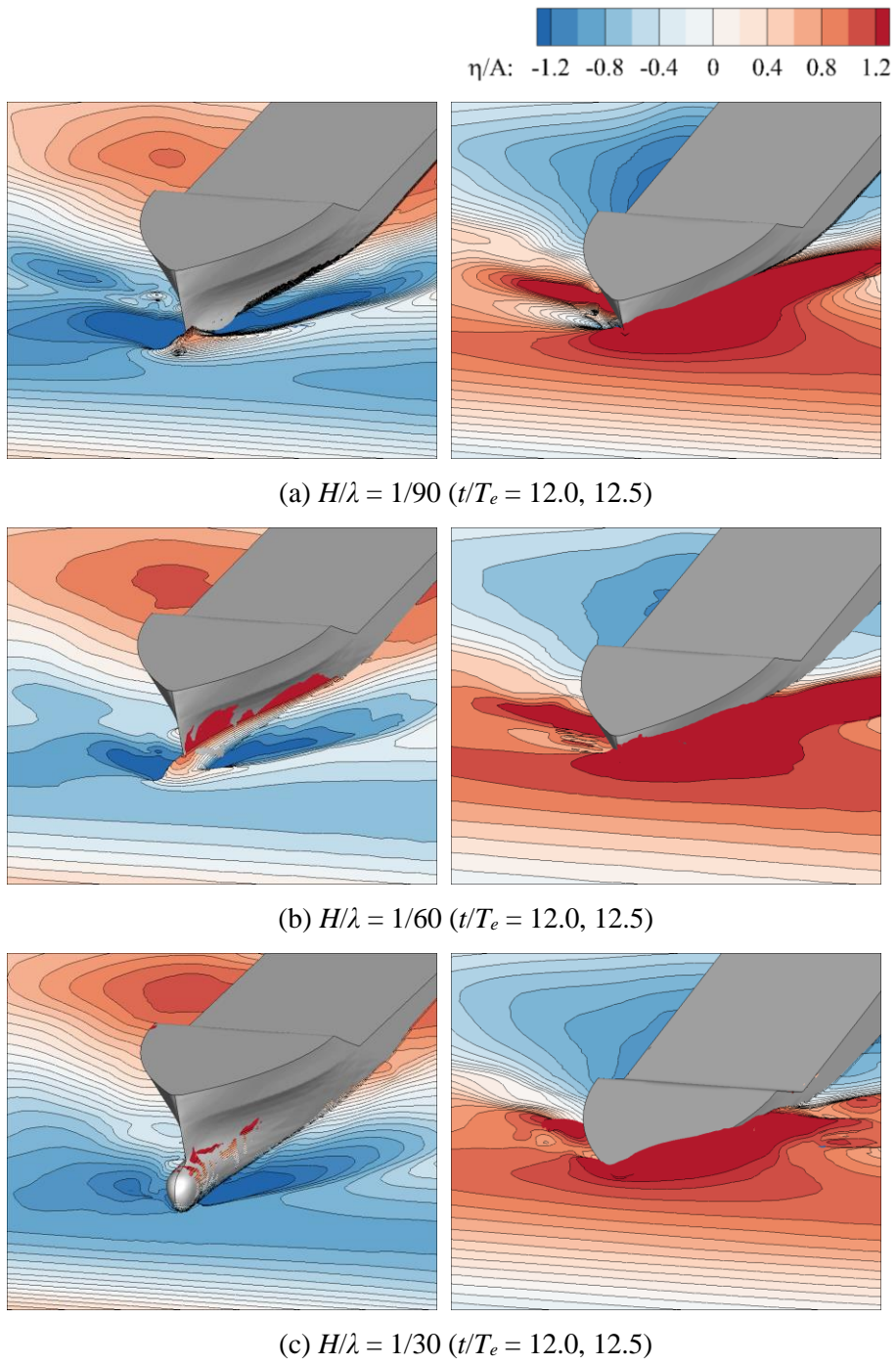
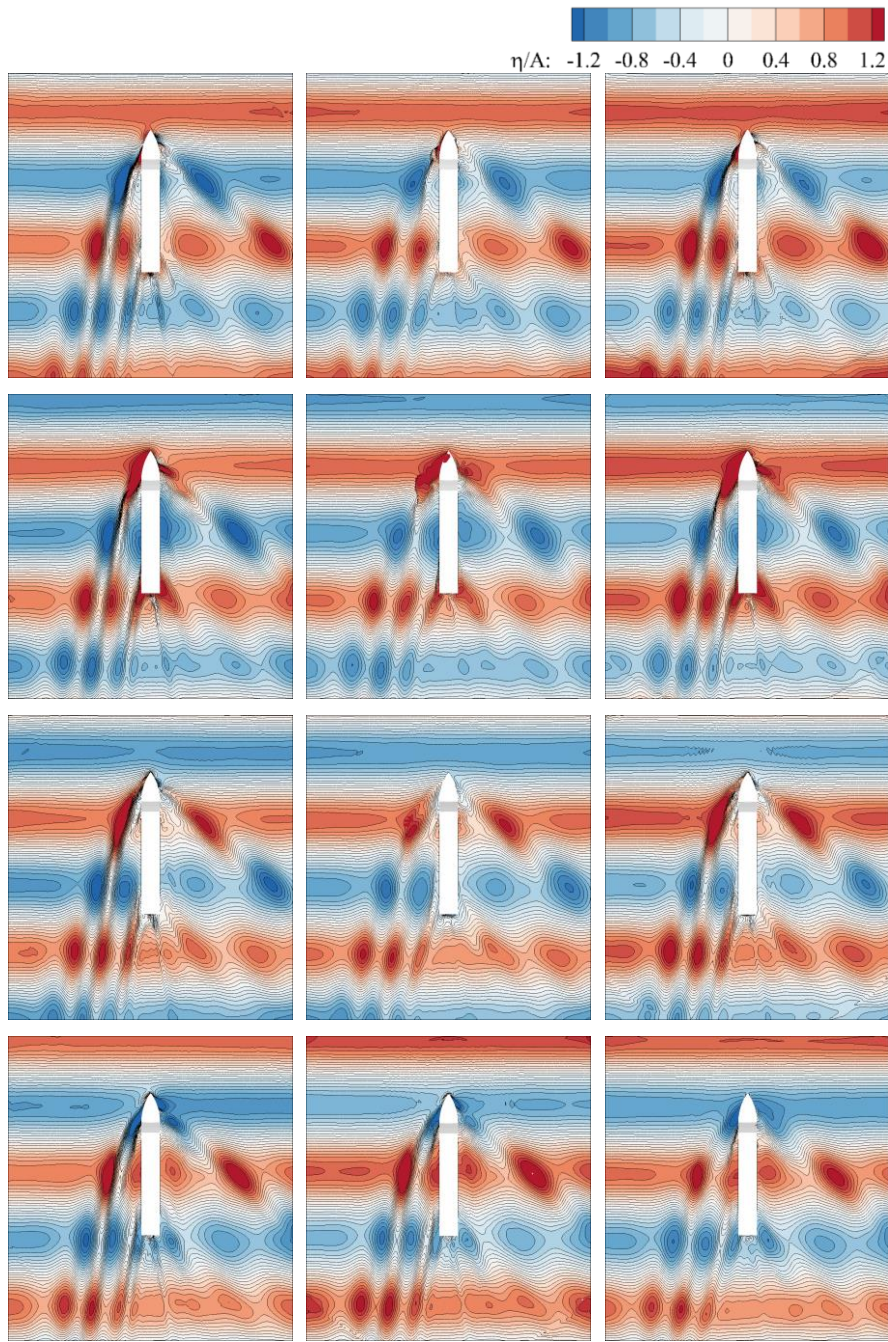


Fig. 6.16 The nonlinear phenomena under different wave slopes, $\beta_0 = 18^\circ$

Then the sequential developments of wave patterns are compared in Fig. 6.17. The wave patterns are generally similar for each wave slope condition, and the asymmetric patterns are caused by the static drift motion. Compared with the high wave slope ($H/\lambda = 1/30$), the diffracted waves of the lower wave slope case ($H/\lambda = 1/90$) seem to be more compressed and to have higher density. This might indicate that the lower wave slope case has higher added forces from the viewpoint of wave pattern analysis.

Fig. 6.18 compares the hull surface distribution of added pressure p_{AW} for each wave slope condition. Only the bow is observed because the added pressure is insignificant on the lateral surface and the stern. The bold black line in Fig. 6.18 is the design waterline, and thinner black lines are the body plan used to indicate the body curvature. To show the effect of hull curvature, the longitudinal component of added pressure $(p_{AW})_x$ is also added for comparison. The normalization factor of added pressure is $\rho g A$.

The nonlinearity of wave added effect is very prominent as observed in Fig. 6.18. The added pressure is very high at the low wave slope condition, while it becomes very small as the wave slope increases. Meanwhile, due to the small flare angle of this containership model, the wave added effect mainly acts in the ship transverse direction for the ship static drift motion. When the wave slope is $1/90$, the region of wave added effect upward moves to nearly the deck. This is due to the significant change in the waterlines shown in previous Fig. 6.14.

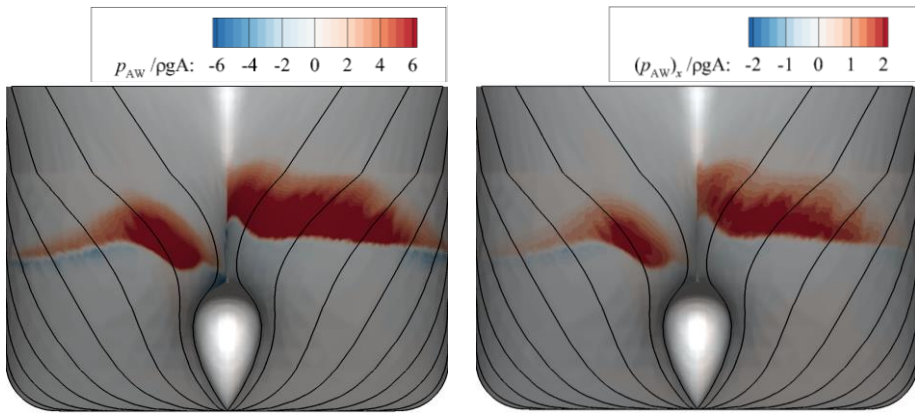


(a) $H/\lambda = 1/90$

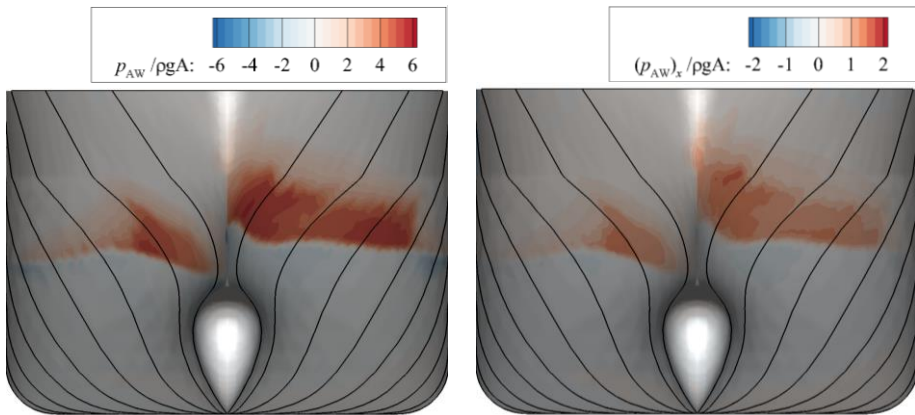
(b) $H/\lambda = 1/60$

(c) $H/\lambda = 1/30$

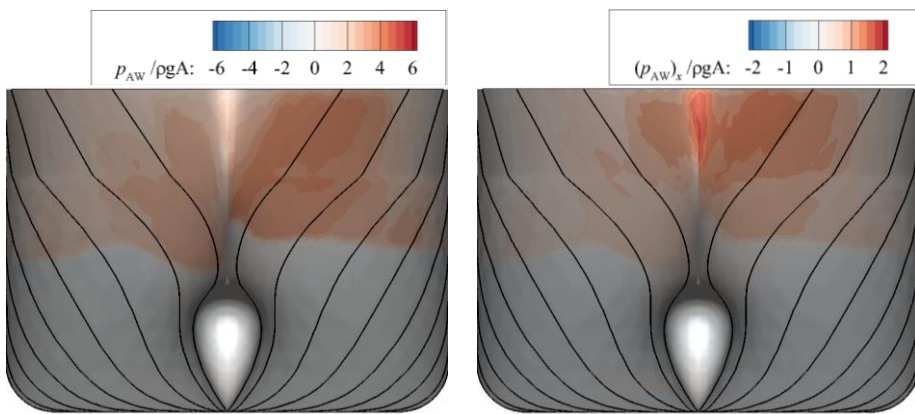
Fig. 6.17 Wave patterns under various wave slopes, $\beta_0 = 18^\circ$



(a) $H/\lambda = 1/90$



(b) $H/\lambda = 1/60$



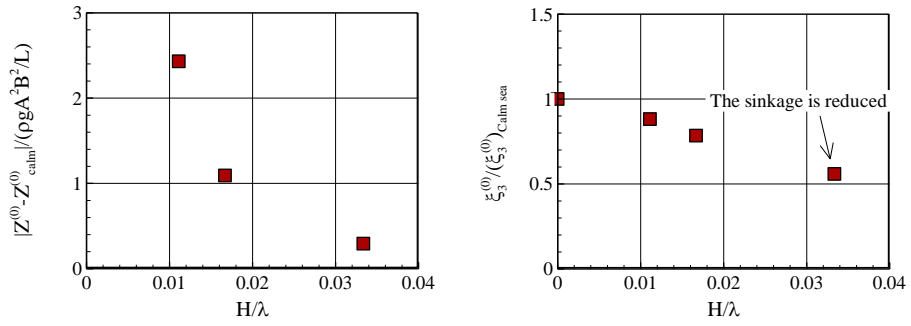
(c) $H/\lambda = 1/30$

Fig. 6.18 Added pressure distribution under various wave slopes, $\beta_0 = 18^\circ$

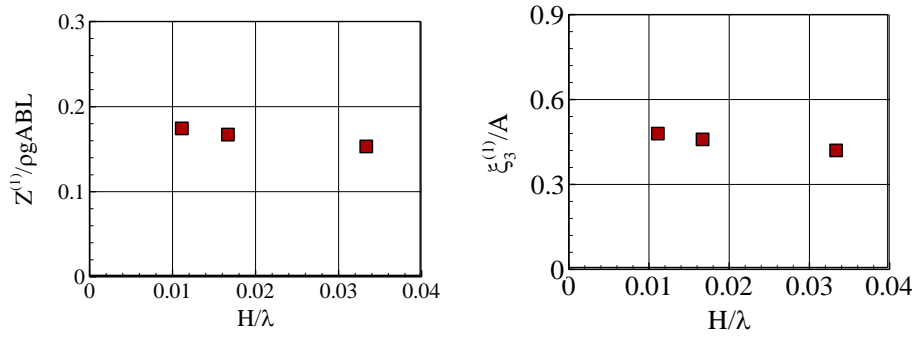
To further understand the nonlinear effect of wave slope on the ship static drift motion in waves. The harmonic components of wave-induced heave and pitch motions and the corresponding ship vertical force and pitch moment were discussed. Fig. 6.19 shows the mean, 1st-order, and 2nd-order amplitudes of heave motion and ship vertical force.

The mean heave motion is normalized by the mean sinkage measured in calm sea. The $H/\lambda = 0$ case indicates the results measured under the calm-sea condition. It can be observed that the ship sinkage becomes reduced as the wave slope increases, and the mean vertical force is also reduced correspondingly. The 1st-order and the 2nd-order amplitudes of heave motion and vertical force are normalized by wave amplitude A and A^2 , respectively. Fig. 6.19 shows a clear tendency that the higher wave slope provides smaller motion and force amplitudes.

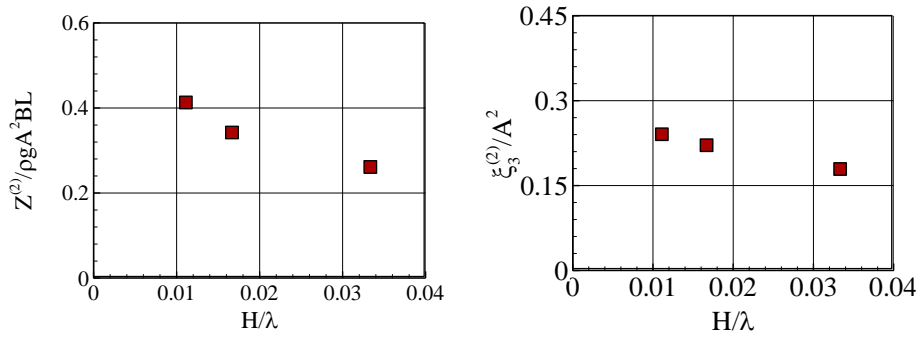
A similar tendency of the wave slope effect is observed in the pitch moment and corresponding pitch motion, as shown in Fig. 6.20. The increasing wave slope has reduced the mean trim attitude, and it has also reduced the amplitudes of pitch motion and pitch moment.



(a) 0th-order component

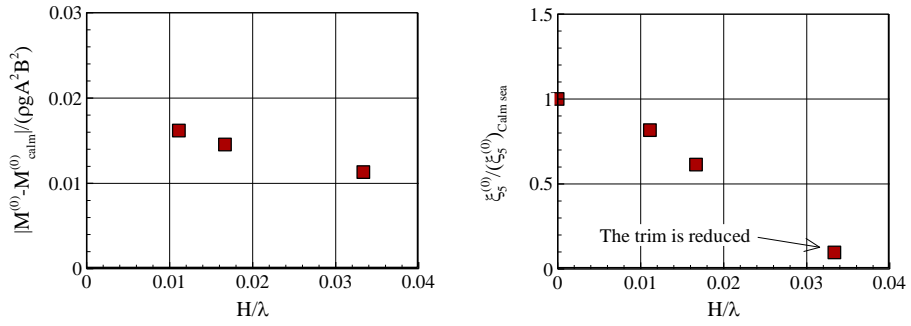


(b) 1st-order component

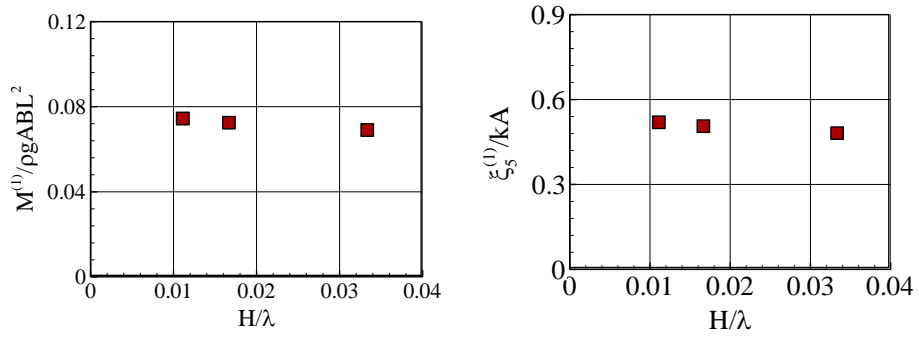


(c) 2nd-order component

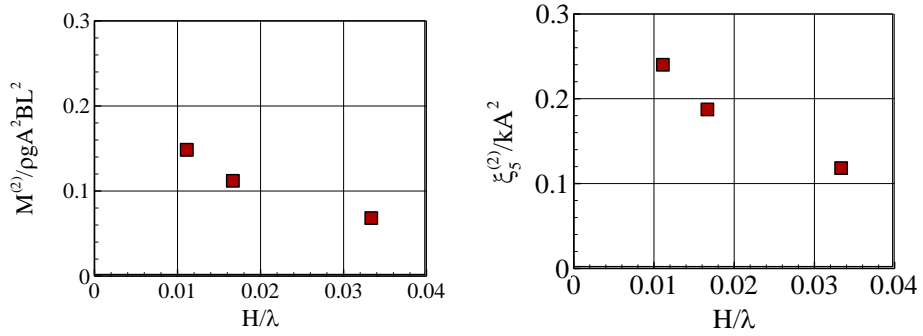
Fig. 6.19 Exciting vertical force Z and heave motion ξ_3 w.r.t. wave slope



(a) 0th-order component



(b) 1st-order component



(c) 2nd-order component

Fig. 6.20 Exciting pitch moment M and pitch motion ξ_5 w.r.t. wave slope

Similar to the tendency observed on heave and pitch motion, the added sway force and added yaw moment also reduce significantly in the high wave slope case. Fig. 6.21 presents the mean value and 1st-order amplitude of the added sway force and the added yaw moments.

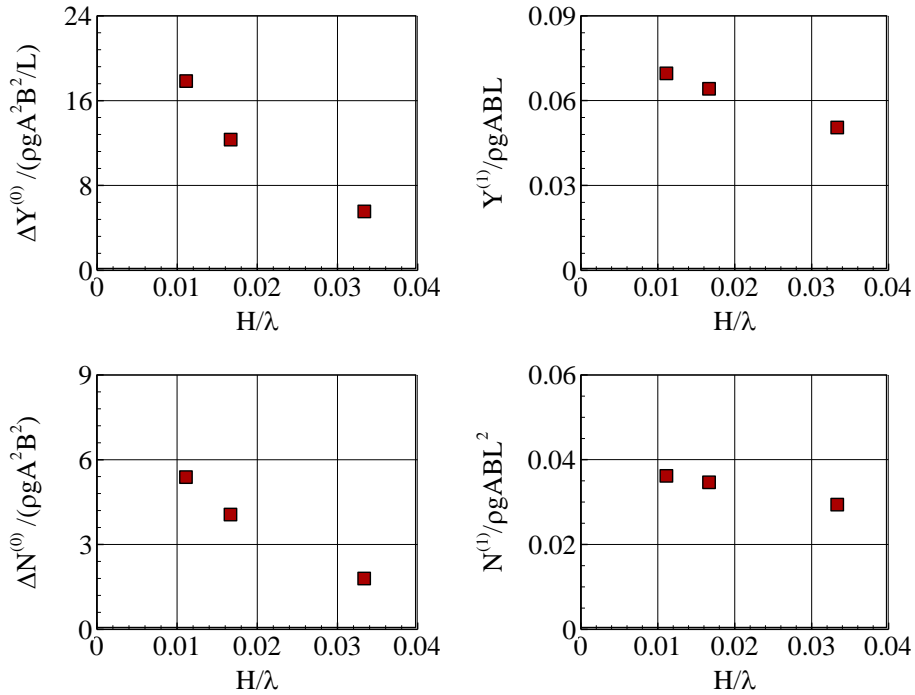


Fig. 6.21 Force/moment of the static drift test w.r.t. wave slope

Fig. 6.22 presents the wave slope effect on the manoeuvring coefficients that are obtained by total sway force and total yaw moment. The dashed line in the figures indicates the value obtained under the calm-sea condition. Opposite to the tendency that added force/moment decreases with the increasing wave slope, the manoeuvring coefficients are shown in Fig. 6.22 actually increase as the wave slope. The high-slope waves have improved the

coefficients significantly because the total force or moment is considerable. A nonlinear tendency is observed between the coefficients and the wave slope, as observed in Fig. 6.22.

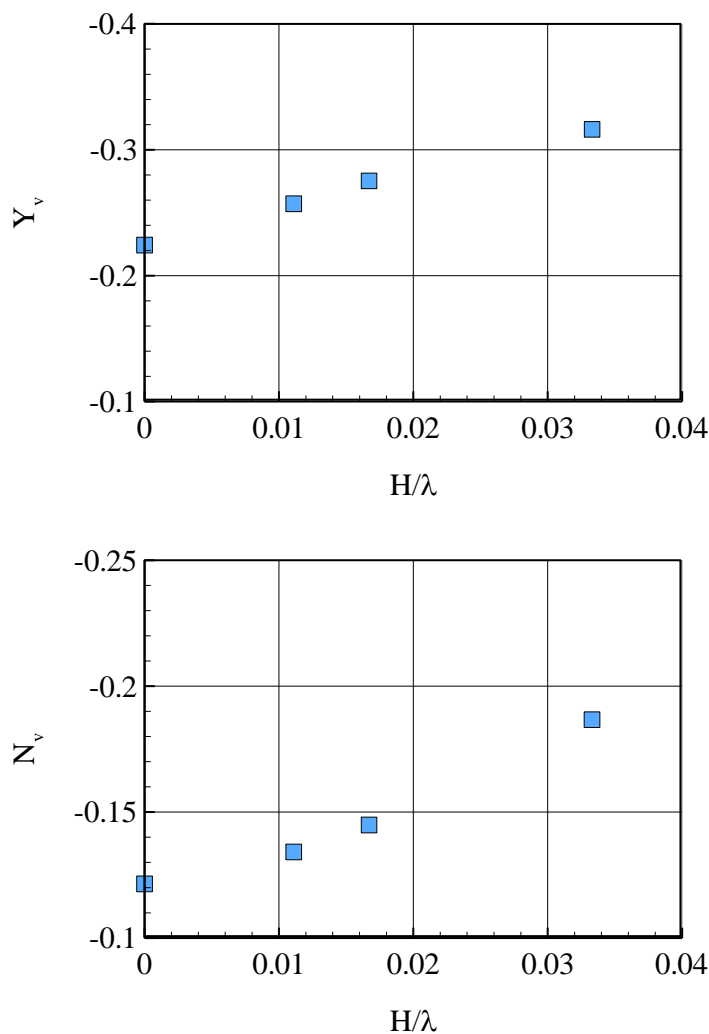


Fig. 6.22 Wave slope effect on the manoeuvring coefficients Y_v and N_v

6.2.2 Pure yaw test

To understand the wave slope effect on the interested force/moment component of the pure yaw test, the case with a large yaw rate $r_0' = 0.5$ was selected for observing the motions and forces.

Fig. 6.23 and 6.24 present the time histories of wave-induced motion responses and body force/moment obtained under different wave slope conditions. The time history of ship yaw angle is also added to indicate the ship's yawing state.

For the heave and pitch motion shown in Fig. 6.23, the motion amplitudes slightly increase at the stage that the ship yaw angle is large and the oblique wave effect occurs. The normalized motion amplitudes, especially the amplitudes of heave motion, decrease as the wave slope becomes high. This tendency is similar to that observed in the static drift test.

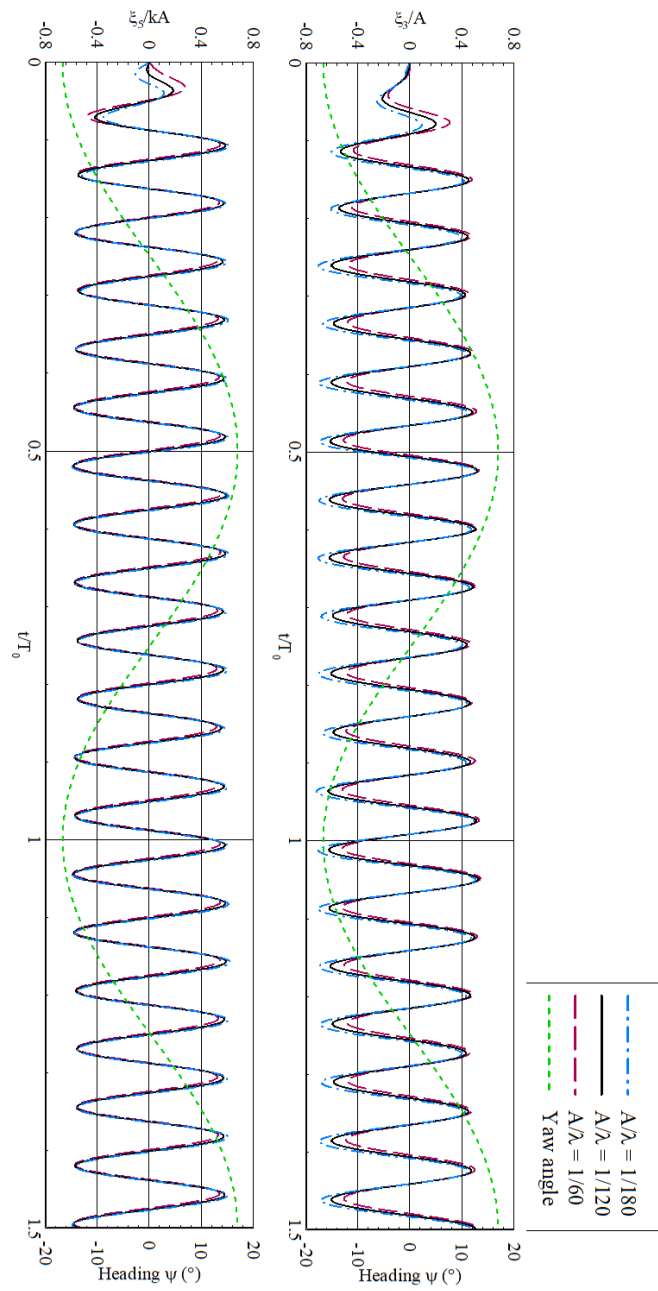


Fig. 6.23 Motion signal of the pure yaw test in waves

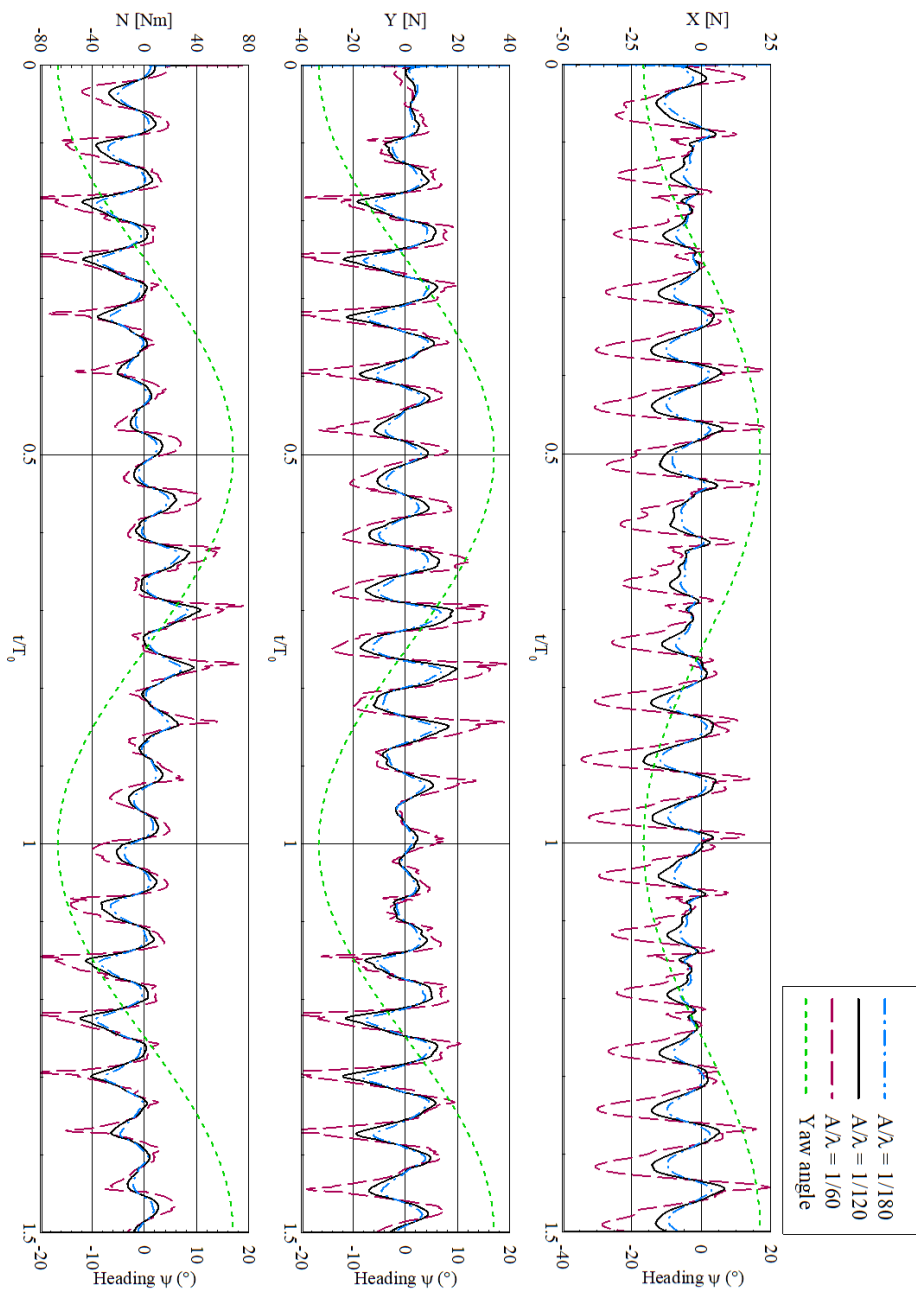


Fig. 6.24 Force/moment signal of the pure yaw test in waves

For the body force/moment shown in Fig. 6.24, the wave excitation amplitude of surge force is stronger when the ship has a large yaw angle and oblique wave effect. Whereas the wave excitation amplitudes of sway force and yaw moment are much stronger when the ship has zero yaw angle but maximum yaw rate. The nonlinearity of sway force and yaw moment is also stronger at the stage of maximum yaw rate, due to the increasing wave elevation on the bow.

Fig. 6.25 summarizes the added sway force and added yaw moment of the pure yaw tests under different wave slopes. The nonlinear tendency of wave slope is generally similar to what was observed from the static drift tests.

Moreover, the manoeuvring coefficients also show the nonlinear relation with the wave slope conditions, as Fig. 6.26. The high slope condition has significantly changed the manoeuvring coefficients of yaw rate, particularly the coefficient Y_r which is usually insignificant under the calm-sea condition. Although the normalized added force/moment of the high wave slope condition is weak, the total force/moment is much stronger than that of the low wave slope condition.

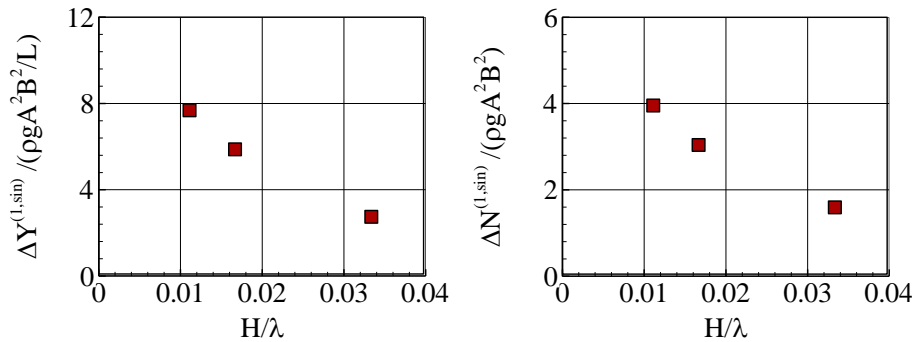


Fig. 6.25 Wave slope effect on the added force/moment of pure yaw test

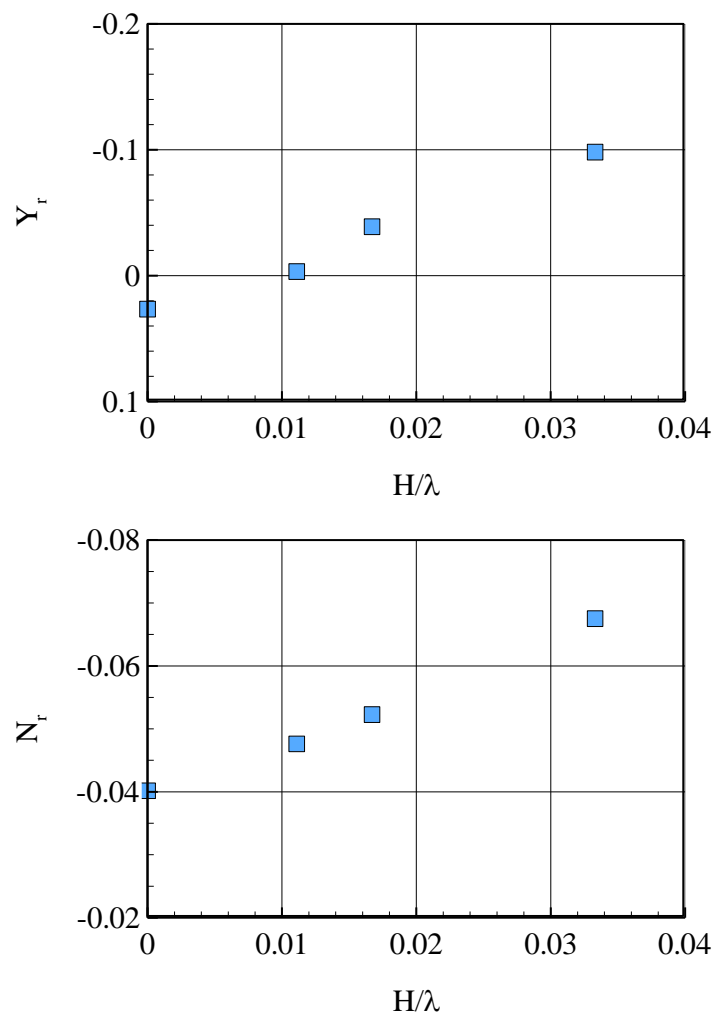


Fig. 6.26 Wave slope effect on manoeuvring coefficients

6.3 Wave direction effect

The wave incident direction with respect to ship heading direction always changes when the ship manoeuvres in waves. In terms of the wave added forces or moments, usually the bow waves provide more significant contributions to the ship. The added force/moment of stern waves is relatively small. Although the stern waves can rise special safety-related issues, such as parametric roll and broaching, these issues were not involved in the present PMM tests in waves since the ship roll motion was always fixed.

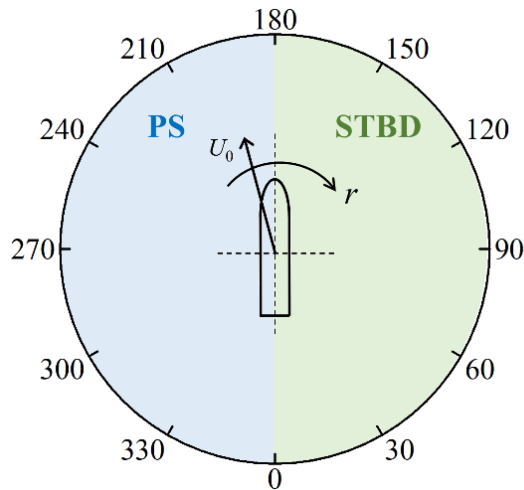


Fig. 6.27 Wave incident direction for the manoeuvring ship

This part is to investigate the ship manoeuvrability under different wave directions. The wavelength and wave slope were fixed to be $\lambda/L = 1$ and $H/\lambda = 1/60$, respectively. The wave directions ranging from 0° to 360° were examined. Fig. 6.27 described the wave direction specified with respect to the ship heading direction. The 180° is the head sea case and the 0° indicates the

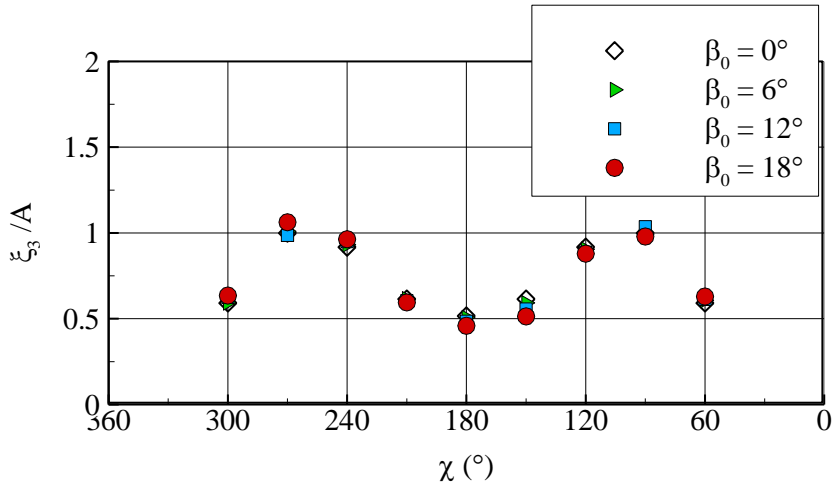
following sea. The positive static drift angle and positive yaw rate are marked to understand its interaction with the wave incident direction. The term “PS” shown in Fig. 6.27 indicates the region where waves incident towards the ship port side, namely $\chi = 180^\circ \sim 360^\circ$; and the term “STBD” indicates the region that the waves incident towards the ship starboard side, namely $\chi = 0^\circ \sim 180^\circ$.

6.3.1 Static drift test

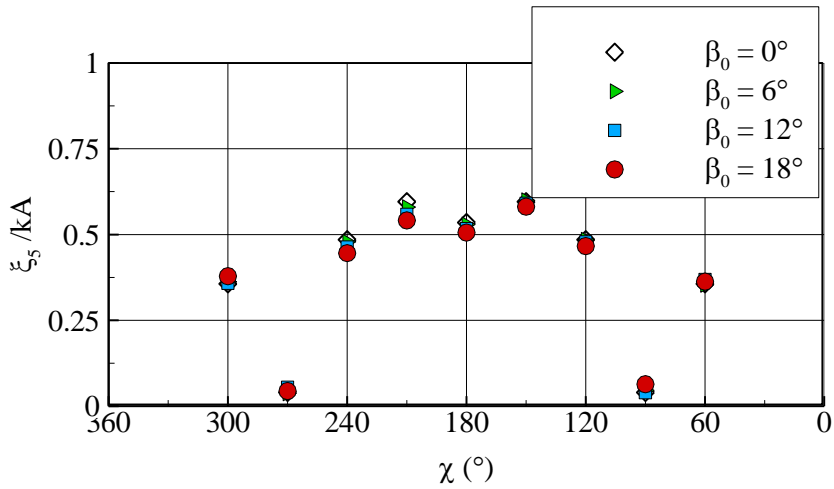
The previous validation study (Section 5.2) examined the wave direction effect on an advancing ship without static drift or yaw conditions. The hydrodynamic characteristics show that the wave added pressure mainly focuses on the bow region, and the beam sea or stern sea provides a very limited effect on the ship motion and forces. It should be mentioned that this conclusion about the wave direction effect only works for the high speed ($Fn = 0.26$), the intermediate wavelength ($\lambda/L = 1.0$) and the fixed wave slope ($H/L = 1/60$).

Due to the static drift motion that changes the wave encountering frequency, the waves of incident direction $0^\circ \sim 180^\circ$ (incidence towards the ship portside, see Fig. 6.27) should induce stronger motion responses than that of the starboard side (wave incident direction $180^\circ \sim 360^\circ$). Fig. 6.28 presented the wave-induced heave and pitch motions for various static drift angles and wave directions. It can be seen that the motion responses at the range of $\chi = 210^\circ \sim 330^\circ$ are larger than that of $\chi = 30^\circ \sim 150^\circ$. The heave motion is very strong in the bow quartering waves and it reaches 1.0 at the beam sea condition. By comparison, the pitch response reaches the peak value at the bow quartering sea condition, and it is almost zero in the beam waves. It can also be observed that the general effect of static drift angle has provided minor changes to the

wave-induced heave or pitch. The general tendency of the wave-induced motions with respect to wave direction is similar to the tendency observed in the previous seakeeping tests (Section 5.2.2). Therefore, the further presentation of the ship hydrodynamic characteristics is not discussed in this part, as already described in Section 5.2.2.

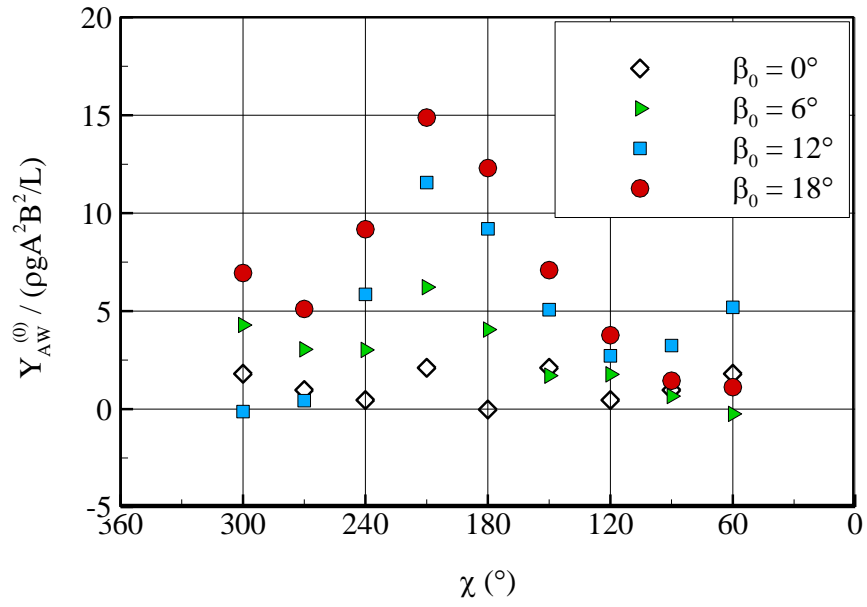


(a) Heave motion

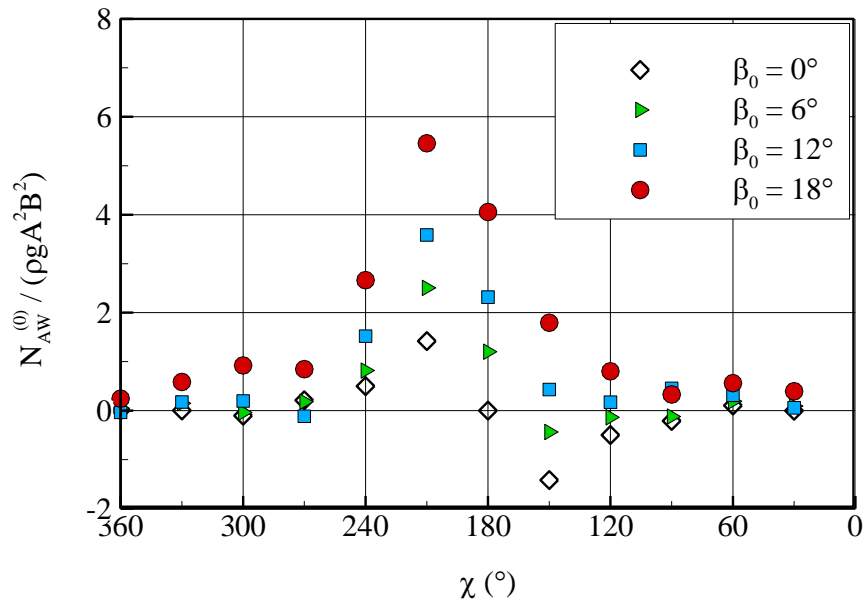


(b) Pitch motion

Fig. 6.28 Wave direction effect on wave-induced motions for static drift tests



(a) Added sway force



(b) Added yaw moment

Fig. 6.29 Wave direction effect on added force/moment for static drift test

Fig. 6.29 shows the wave direction effect on the added sway force and added yaw moment. It can be observed that mainly the “PS” region provides significant added force/moment, and the values are particularly large at the $\chi = 210^\circ$ condition. By comparison, the case that $\chi = 150^\circ$ provides a much smaller added force/moment. This discrepancy between the two ship sides is caused by the different wave encountering conditions of ship drifting motion.

Fig. 6.29 also shows that both the added force and moment are insignificant under the beam sea conditions, although the static drift motion is involved and ship has a large lateral surface. This phenomenon is also observed in **Yasukawa and Adnan (2006)** that the static drift test of a containership was conducted in head sea and beam sea. The reason is that the ship width is much smaller than the length of crossing waves. When the wavelength becomes shorter and closer to ship width, the added force/moment under the beam sea condition can be expected to be stronger.

Fig. 6.30 summarizes the linear manoeuvring coefficients of sway velocity obtained under various wave directions. In the legend, the $(Y_v)_{\text{calm}}$ and $(N_v)_{\text{calm}}$ indicates the coefficients obtained under the calm-sea condition, while the $(Y_v)_{\text{wave}}$ and $(N_v)_{\text{wave}}$ indicates the coefficients obtained under the waves.

It can be seen that the main effect focus on the bow region, particularly the port side towards which the static drift motion U_0 is prescribed. The maximum increase can be nearly 50% at the bow quartering waves of the port side. The physical interpretation of the polar plots of Fig. 6.30 is that a manoeuvring ship would have a stronger turning ability in the bow waves. But in the beam waves or stern waves, the present wave condition ($\text{Fn}=0.26$, $\lambda/L=1.0$, $H/\lambda=1/60$) would not provide significantly improve or reduce the ship turning capability.

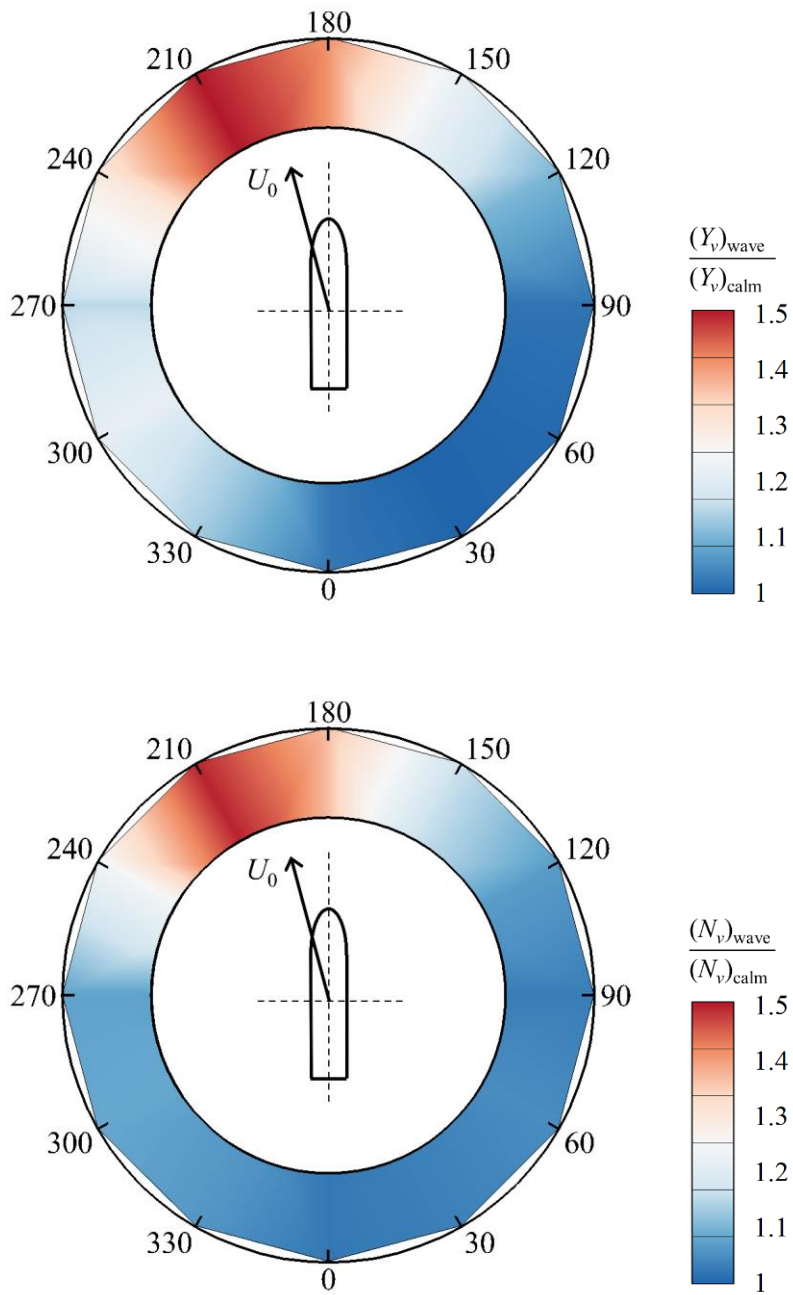


Fig. 6.30 Wave direction effect on the manoeuvring coefficients Y_v and N_v

6.3.2 Pure yaw test

The ship yawing in waves has a dynamic orientation, so it raises a concern that the wave incident direction cannot be fixed with respect to the ship heading direction.

Fig. 6.31 – 6.32 present the typical motion and force signals of a pure yaw test in an oblique sea. The maximum yaw rate r_0' is 0.5, and the wave direction is fixed to be 150° in the global inertial frame. In these figures, the x -axis indicates the time t normalized by harmonic yawing period T_0 . The time history of yaw angle ψ is added in each figure to understand the interaction between the ship yawing motion and the waves. Each figure also contains the schematic description of the ship harmonic yawing trajectory, and the wave incident direction in the global inertia frame is marked as well.

Fig. 6.31 shows the time histories of wave-induced heave (ξ_3/A) and pitch (ξ_5/kA) motions. The heave motion shows a varying amplitude which is caused by the dynamic wave direction rather than the ship yawing rate. At the stage $t/T_0 = 0.5$, the wave incident direction is nearly 180° with respect to the ship heading direction at this stage, so the wave-induced heave amplitude is relatively small. But at the stage $t/T_0 = 1.0$, the oblique effect of incident waves becomes more strong, so the wave-induced heave response also reaches the maximum amplitude. A similar tendency is observed in the pitch motion although the change is not as noticeable as the heave motion. Additionally, the effect of yaw rate on the motions is not that significant.

Fig. 6.32 shows the signals of sway force and yaw moment. Each figure contains four sets of signals: (1) the signal of yaw angle ψ (green dashed line) which is used to understand the interaction between ship yawing direction and wave effects; (2) the signal of the force/moment obtained in calm-sea

condition (black dash-dotted line); (3) the raw signal of the force/moment obtained in the waves (red solid line); (4) the moving-averaged signal of the force/moment obtained in the same waves (blue long-dashed line). To understand the mean wave effect in each wave encountering, the wave encounter period is selected to be the interval of moving average, and the phase shift issue of moving average analysis has been corrected.

For the signals of sway force shown in Fig. 6.32, the sway force has a significant amplitude when the oblique wave effect increases. But the moving-averaged signal shows that the mean wave effect is still very small in each encountering period. It is a hydrodynamic characteristic that the yawing ship usually has insignificant sway force. So the wave effect on the coefficient Y_r will be out of interest.

For the signals of yaw moment shown in Fig. 6.32, the wave effect is more direct and clear. Three motion stages will be analyzed, namely $t/T_0 = 1.25, 1.0, 0.75$. (1) At the stage $t/T_0 = 1.25$, the wave incident direction is actually 150° (see the wave direction defined in Fig. 6.27) because of the negative sign of yaw rate. The amplitude of yaw moment is large due to the oblique wave effect; the moving averaged yaw moment is also large, which means the waves have increased the mean yaw moment in each encounter. (2) At the stage $t/T_0 = 1.25$, the wave oblique direction becomes larger. The amplitude of yaw moment is still large but the moving averaged result shows an insignificant wave added effect in each wave encountering. (3) At the stage $t/T_0 = 1.25$, the wave incident direction is actually 210° (see the wave direction defined in Fig. 6.27) due to the yawing direction. The ship is yawing towards the opposite direction of wave incidence, so the added yaw moment naturally becomes insignificant. It can also be observed at this stage that the moving averaged signal of yaw moment almost overlaps with that measured

in the calm sea.

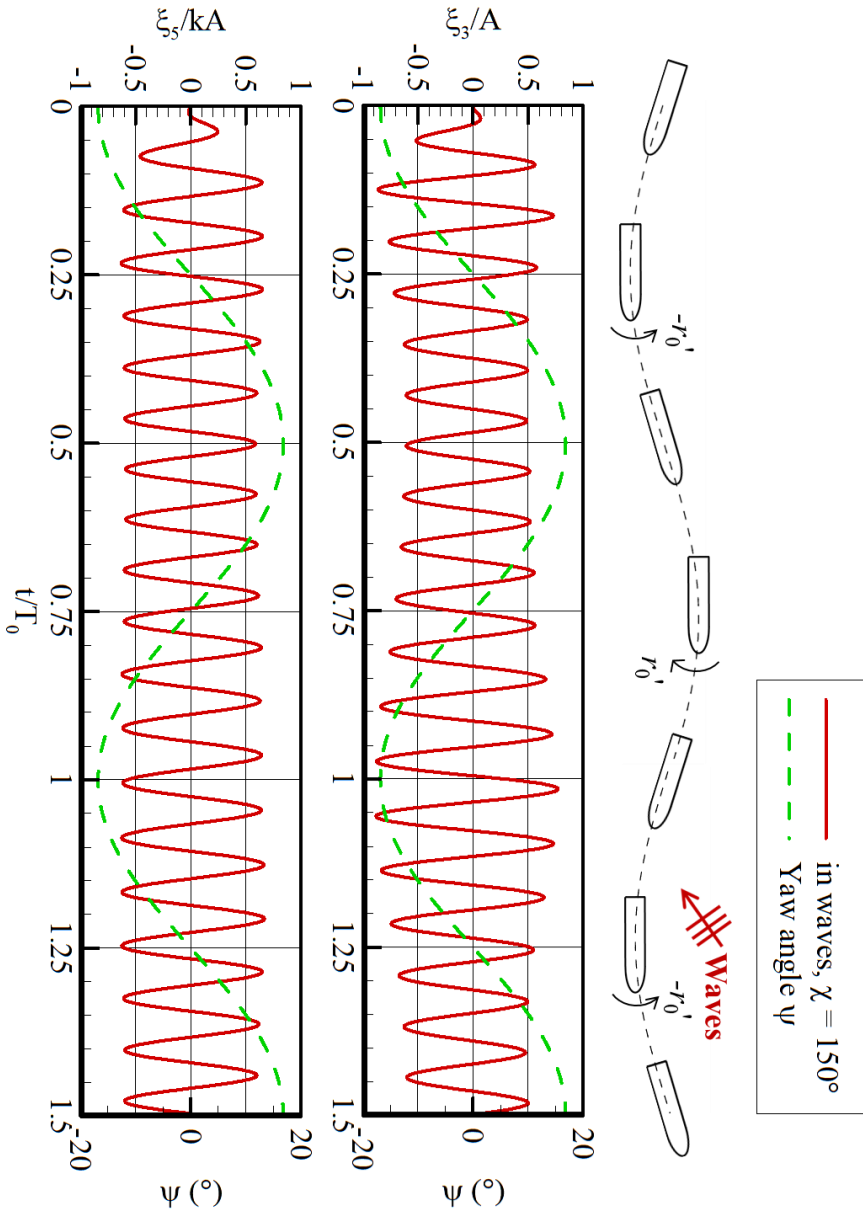


Fig. 6.31 Signals of ship motion for the pure yaw test in an oblique sea

$$(r_0' = 0.5, \lambda/L = 1.0, H/\lambda = 1/60, \chi = 150^\circ)$$

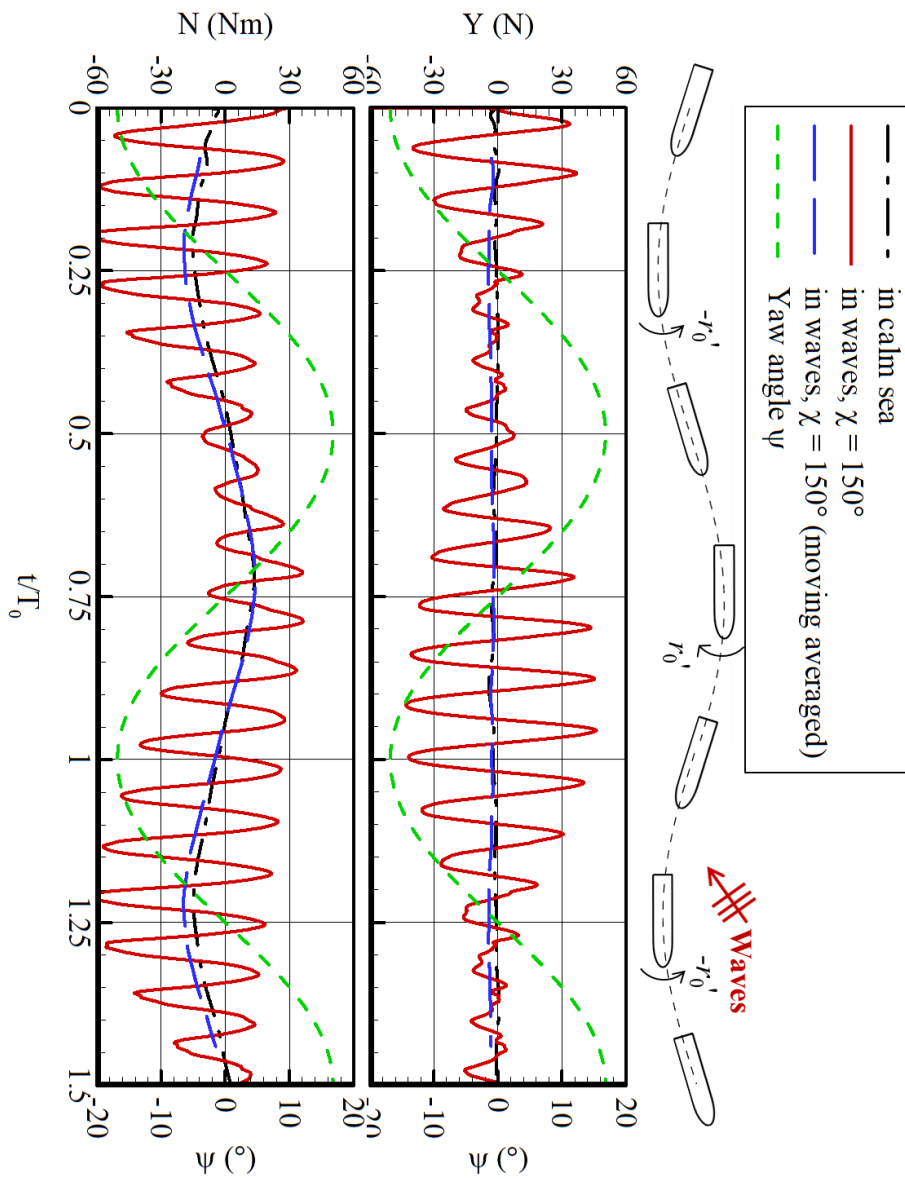
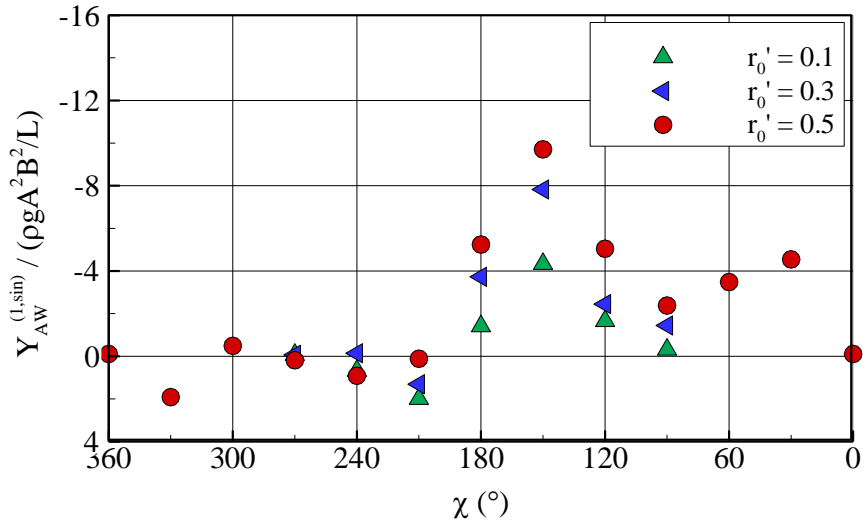
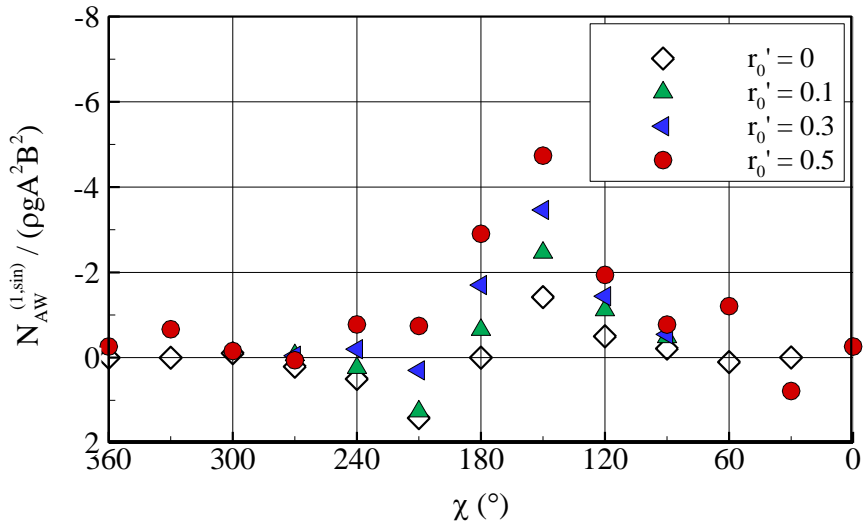


Fig. 6.32 Signals of ship force/moment for the pure yaw test in an oblique sea
 $(r'_0 = 0.5, \lambda/L = 1.0, H/\lambda = 1/60, \chi = 150^\circ)$



(a) Added sway force



(b) Added yaw moment

Fig. 6.33 Wave direction effect on the wave-induced motions for pure yaw test

Fig. 6.33 has summarized the added sway force and added yaw moment with respect to the wave direction specified in the global inertial frame. The values are generally very small except on the starboard side of the bow quartering wave. This is also observed in the manoeuvring coefficients summarized in Fig. 6.34. The beam sea or stern quartering sea provides a very insignificant effect to the added force/moment, so they are not considered in the analysis of manoeuvring coefficients. The physical interpretation of the improved coefficients N_r is that ship turning ability is restrained by the oblique sea condition.

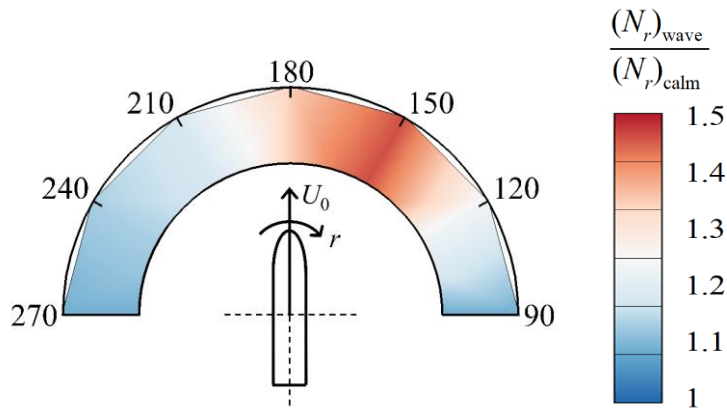


Fig. 6.34 Wave direction effect on the manoeuvring coefficients N_r

7. Conclusions

This study aims to understand the ship manoeuvrability in waves. A series of numerical PMM tests of the KCS containership model has been carried out to observe the manoeuvring coefficients under different wave frequencies, wave slopes, and wave directions. The following conclusions were drawn from the present study:

A numerical tank has been successfully applied for the PMM tests

- A computational domain that works as a moving wave tank was built based on the CFD method. The tank can be used for diverse PMM motions, and the coupling between prescribed planar motion and wave-induced motion was achieved through the local deforming mesh technique.
- An effective wave forcing region was implemented inside the tank, and the traditional $k-\omega$ SST turbulence model has been enhanced to control the over-production of the turbulence fields.
- Meanwhile, the computational cost was estimated for carrying out a series of PMM tests for obtaining the complete list of hull manoeuvring model. Based on the 100 cluster cores shown in this work, the total cost is about 12-18 days for the calm-sea tests.

Systematic verification and validation tests have been examined

- Two independent series of tests, the calm-sea PMM tests and the seakeeping tests, have been considered to examine the numerical uncertainties and validation.
- The uncertainty of time window was discussed for the data analysis. The uncertainties of discretization factor, grid size and time step, were also

investigated for a reliable prediction of the body y^+ fields and numerical wave fields. Generally, the uncertainties were well restrained by a convergent numerical model.

- It is one of the future works to reduce the smearing phenomenon observed in this study. The numerical waves were found to be slightly smearing along with the space. But the wave smearing caused by time is not found, the wave profile and propagating phase remain well as the simulation time marches.
- Meanwhile, the validation work on the calm-sea PMM tests involves static drift test, pure yaw test, pure yaw test, and combined drift-yaw test. The results generally agreed well with the test data and other numerical results. The manoeuvring coefficients of KCS hull have been compared with the sources of other studies, and the coefficients were further applied for predicting ship manoeuvring motion.
- The validation of seakeeping tests involved the wave frequency effect and the wave direction effect. By the advantages of CFD method, the hydrodynamic characteristics, such as wave pattern and wave added pressure, were presented for various wave conditions. The predicted motion and added resistance also showed an agreeable tendency with the other comparing data.

Manoeuvring coefficients have been observed under wave effects

- A series of static drift tests and pure yaw tests were conducted in the waves. Three wavelengths ($\lambda/L = 0.5, 1.0, 1.5$) were considered to observe the hydrodynamic characteristics and wave added force/moment. Limited to the constant wave slope condition, the short waves provided a very small change to the manoeuvring coefficients, whereas both the intermediate

waves and long waves increased the coefficients by about 50%.

- The wave slope condition was also examined for the PMM tests. The wave patterns and the surface distribution of added pressures were found to be very nonlinear to the wave slope. A nonlinear relation was also observed between the wave slope and the manoeuvring coefficients.
- The pure yaw test has a dynamic orientation with respect to the incident waves. The oblique wave effect can alter the wave-induced motions and forces, but the analysis showed that the in-phase region of yaw motion was actually less disturbed by the ship dynamic orientation. The memory effect of such dynamic PMM tests was not that severe by examining the sequential development of wave pattern and vorticity field.
- For the wave direction effect, the applied wave conditions ($\lambda/L=1.0$, $H/\lambda=1/60$) showed that manoeuvring coefficients mainly change in a bow quartering sea. It is one of the future works to apply these observed phenomena to explain the ship manoeuvrability observed from the direct manoeuvring tests.

Reference

- [1] Abdel-Maksoud, M., Muller, V., Xing, T., Toxopeus, S., Stern, F., Petterson, K., Tormalm, M., Kim, S., Aram, S., Gietz, U., Schiller, P., Rung, T., 2016. Experimental and numerical investigations on flow characteristics of the KVLCC2 at 30° drift angle. *Transactions – Soc. of Naval Archit. and Mar. Eng.* 123, 139-164.
- [2] Abkowitz, M.A., 1969. *Stability and motion control of ocean vehicles.* The MIT Press, USA.
- [3] Abkowitz, M.A., 1980. Measurement of hydrodynamic characteristics from ship maneuvering trials by system identification. *SNAME Trans.* 88, 283–318.
- [4] Burcher, R.K., 1975. Studies into the validity of quasi-steady prediction techniques. In: *Proc. 14th ITTC.* Ottawa, Canada.
- [5] Celik, I., Chia, U., Roache, P.J., and Raad, P.E., 2008. Procedure of estimation and reporting of uncertainty due to discretization in CFD applications. *J. Fluids Eng, ASME*, 130(7), 078001.
- [6] Clarke, D., Gedling, P., Hine, G., 1983. The application of manoeuvring criteria in hull design using linear theory. *Transactions of RINA*, 45-68.
- [7] Cura-Hochbaum, A., 2011. On the numerical prediction of the ship's manoeuvring behavior. *J. Ship Sci. and Tech.* 5, 27-39.
- [8] Deshpande, S.S., Anumolu, L., Trujillo, M.F., 2012. Evaluating the performance of the two-phase flow solver interFoam. *Comput. Sci. Disco.* 5(1), 014016.
- [9] Devolder, B., Rauwoens, P., Troch, P., 2017. Application of a buoyancy-modified k- ω SST turbulence model to simulate wave run-up around a

- monopile subjected to regular waves using OpenFOAM®. J. Coastal Eng. 125, 81-94.
- [10] Gertler, M., 1959. The DTMB planar-motion-mechanism system. Symposium on the Towing Tank Facilities, Instrumentation and Measuring Technique. Zagreb, Croatia.
- [11] Goodman, A., 1960. Experimental techniques and methods of analysis used in submerged body research. In: Proc. 3rd Symp. on Naval Hydrodyn. Scheveningen, Netherlands.
- [12] Goodman, A., Gertler, M., Kohl, R., 1976. Experimental techniques and methods of analysis used at HYDRONAUTICS for surface-ship maneuvering predictions. In: Proc. the 11th Symp. on Naval Hydrodyn. London, UK.
- [13] Grim, O., Oltmann, P., Sharma, S.D., Wolff, K., 1976. CPMC – A novel facility for planar motion testing of ship models. In: Proc. the 11th Symp. on Naval Hydrodyn. London, UK.
- [14] Haddara, M. R. and Wang, Y., 1999. Parametric identification of maneuvering models for ships. International Shipbuilding Progress. 46(445), 5-27.
- [15] Sadat-Hosseini, H., Toxopeus, S., Kim, D.H., Castiglione, T., Sanada, Y., Stocker, M., Simonse, C., Otzen, J.F., Toda, Y., Stern, F., 2015. Experiments and computations for KCS added resistance for variable heading. In: Proc. of 5th World Maritime Tech. Conf. Rhode island, USA.
- [16] Hasnan, M.A.A., Yasukawa, H., Hirata, N., Terada, D., Matsuda, A., 2019. Study of ship turning in irregular waves. J. Mar. Sci. Technol. 25, 1024-1043.
- [17] Hess, D., and Faller, W., 2000. Simulation of ship manoeuvres using recursive neural networks. In: Proc. of 23rd Symposium on Naval

- Hydrodyn., 17-22.
- [18] Hirano, M., Takashina, J., Takeshi, K., Saruta, T., 1980. Ship turning trajectory in regular waves. *Trans. West-Japan Soc. Naval Archit.* 60, 17–31.
 - [19] Hirayama, T., Kim, S.E., 1994. Manoeuvrability of a full ship in directional spectrum waves of short wave length. *J. Soc. Naval Archit. Jpn.* 176, 129–136.
 - [20] Islam, H., Soares, G., 2018. Estimation of hydrodynamic derivatives of a container ship using PMM simulation in OpenFOAM. *J. Ocean Eng.* 164, 414-425.
 - [21] ITTC, 2014. ITTC – Recommended procedures and guidelines: Practical guidelines for ship CFD applications. 7.5-03-02-03.
 - [22] ITTC, 2021. ITTC – Recommended procedures and guidelines: Uncertainty analysis in CFD verification and validation methodology and procedures. 7.5-03-01-01.
 - [23] ITTC, 2021. ITTC – Recommended procedures and guidelines: Captive model test. 7.5-02-06-02.
 - [24] ITTC, 2021. The special committee on manoeuvring in waves, final report and recommendations to the 29th ITTC.
 - [25] Jacobsen, N.G., Fuhrman, D.R. and Fredsoe, J., 2011. A wave generation toolbox for the open-source CFD library: OpenFoam®. *Int. J. Num. Methods in Fluids*, 70, 1073-1088.
 - [26] Kijima, K., Nakiri, Y., Tsusui, Y., and Matsunaga, M., 1990. Prediction method of ship manoeuvrability in deep and shallow water. In *Proc. of MARSIM*, Tokyo, Japan.
 - [27] Kim, D.J., Yun, K., Park, J.Y., Yeo, D.J., Kim, Y.G., 2019. Experimental investigation on turning characteristics of KVLCC2 tanker in regular

- waves. *Ocean Eng.* 175, 197–206.
- [28] Kim, D.J., Yun, K., Yeo, D.J., Kim, Y.G., 2020. Initial and steady turning characteristics of KCS in regular waves. *Applied Ocean Res.* 105, 1024210.
 - [29] Kim, G.H., Park, S., 2017. Development of a numerical simulation tool for efficient and robust prediction of ship resistance. *Int. J. Naval Archit. and Ocean Eng.* 9 (5), 537-551.
 - [30] Mahfouz, A. B. and Haddara, M. R., 2003. Effects of the damping and excitation on the identification of the hydrodynamic parameters for an underwater robotic vehicle. *Ocean Eng.* 30, 1005-1025.
 - [31] Milanov, E., Efremov, D. and Anastasov, A., 2021. Experimental study on KCS container ship initial turning at low speed in regular waves. *Maritime Tech. and Res.* 3(2).
 - [32] Larsen, B.E., Fuhrman, D.R., 2018. On the over-production of turbulence beneath surface waves in Reynolds-averaged Navier-Stokes models. *J. Fluid Mech.* 853, 419-460.
 - [33] Lee, J. H., Kim, Y., 2020. Study on steady flow approximation in turning simulation of ship in waves. *Ocean Eng.*, 195, 106645.
 - [34] Lee, J.H., Kim, Y., Kim, B.S., Gerhardt, F., 2021. Comparative study on analysis methods for added resistance of four ships in head and oblique waves. *Ocean Eng.*, 236, 109552.
 - [35] Lee, J.; Nam, B.W.; Lee, J.-H.; Kim, Y., 2021. Development of new two-time-scale model for ship manoeuvring in waves. In *Proc. of the 31th Int'l Ocean and Polar Eng. Conf.*, Rhodes, Greece.
 - [36] Lee, J.H., Nam, B.W., Lee, J-H., Kim, Y., 2021. Development of enhanced two-time-scale model for simulation of ship maneuvering in ocean waves. *J. Mar. Sci. Eng.*, 9, 700.

- [37] Liu, Y., Zou, L., Zou, Z., Guo, H., 2018. Predictions of ship maneuverability based on virtual captive model tests. *J. Eng. Applications of Computational Fluid Mech.* 12 (1), 334-353.
- [38] MEPC, 2017. 2013 interim guidelines for determining minimum propulsion power to maintain the manoeuvrability of ships in adverse conditions.
- [39] Nakamura, S., Naito, S., 1977. Propulsive performance of a containership in waves. *J. Soc. Nav. Archit. Japan*, 15, 24–48.
- [40] Nomoto, K., 1975. Ship response in directional control taking account of frequency dependent hydrodynamic derivatives. In: *Proc. 14th ITTC*. Ottawa, Canada.
- [41] OpenFOAM®, 2019. OpenFOAM: API Guide v1912. <https://www.openfoam.com/documentation/guides/latest/api/> (accessed 1 February 2020)
- [42] Oltmann, P., 1992. Coefficient estimation. Report of Hamburg Ship Model Basin.
- [43] Park, D.M., Lee, J.H., Jung, Y.W., Lee, J., Kim, Y., 2019. Experimental and numerical studies on added resistance of ship in oblique sea conditions. *Ocean Eng.*, 186, 106070.
- [44] Rabliås, Ø., Kristiansen, T., 2019. Free running maneuvering tests of the DTC hull in calm water and regular waves with focus on uncertainty analysis based on repetition tests. In: *Proc. of Int. Conference on Ship Manoeuvring in Shallow and Confined Water (MASHCON2019)*. Ostend, Belgium.
- [45] Ren, Z., Wang, J., Wan, D., 2020. Investigation of the flow field of a ship in planar motion mechanism tests by the vortex identification method. *J. Mar. Sci. and Eng.* 8 (9), 649.

- [46] Roache, P.J., 1998. Verification and validation in computational science and engineering. Hermosa Pub, USA.
- [47] Sakamoto, N., 2009. URANS and DES simulations of static and dynamic maneuvering for surface combatant. PhD Dissertation. The Univ. of Iowa, USA.
- [48] Sanada, Y., Tanimoto, K., Takagi, K., Gui, L., Toda, Y., Stern, F., 2013. Trajectories for ONR Tumblehome maneuvering in calm water and waves. *Ocean Eng.* 72, 45–65.
- [49] Seo, M.G., Ha, Y.J., Nam, B.W., Kim, Y., 2021. Experimental and numerical analysis of wave drift force on KVLCC2 moving in oblique waves. *J. Mar. Sci. Eng.* 9, 136.
- [50] Seo, M.G., Kim, Y., 2011. Numerical analysis on ship maneuvering coupled with ship motion in waves. *Ocean Eng.*, 38, 1934-1945.
- [51] Simonsen, C.D., Otzen, J.F., Klimt, C., Larsen, N.L., Stern, F., 2012. Maneuvering predictions in the early design phase using CFD generated PMM data. In: *Proc. 29th Symp. on Naval Hydrodyn.* Gothenburg, Sweden.
- [52] Skejic, R., Faltinsen, O.M., 2008. A unified seakeeping and maneuvering analysis of ships in regular waves. *J. Mar. Sci. Technol.* 13 (4), 371–394.
- [53] Smitt, L.M., Chislett, M.S., 1974. Large amplitude PMM tests and manoeuvring predictions for a Mariner class vessel. In: *Proc. 10th Symp. on Naval Hydrodyn.* Boston, USA.
- [54] Sprenger, F., Hassani, V., Maron, A., Delefortrie, G., Zwijnsvoorde, T.V., Cura- Hochbaum, A., Lengwinat, A., 2016. Establishment of a validation and benchmark database for the assessment of ship operation in adverse conditions. In: *Proc. of the 35th Int’l Conf. on Ocean, Offshore & Arctic Eng. (OMAE2016).* Busan, Korea.

- [55] Stern, F., Wilson, V.R., Coleman, H.W., Paterson, E.G., 1999. Verification and validation of CFD simulations. IIHR Report No. 407.
- [56] Strom-Tejsen, J., Chislett, M.S., 1966. A model testing technique and method of analysis for the prediction of steering and manoeuvring qualities of surface ships. In: Proc. the 6th Symp. on Naval Hydrodyn. Washington DC, USA.
- [57] Stocker, M.R., 2016. Surge free added resistance tests in oblique wave headings for the KRISO container ship model. Degree thesis, Univ. of IOWA.
- [58] Sung, Y.J., 2013. Sensitivity analysis on the manoeuvrability indices based on the confidence interval of manoeuvring coefficients from PMM test. The Korea Assoc. of Ocean Sci. Tech. Soc., Jeju, Korea.
- [59] Sung, Y.J., Lee, H.H., Lee, T., Kim, S.E., 2012. Analysis on the manoeuvring performance of ship motion in waves (in Korean). The Korea Assoc. of Ocean Sci. Tech. Soc., Daegu, Korea.
- [60] Sung, Y.J., Park, S.H., 2015. Prediction of ship manoeuvring performance based on virtual captive model tests. J. the Soc. of Naval Archit. of Korea. 52 (5), 407-417.
- [61] Ueno, M., Nimura, T., Miyazaki, H., 2003. Experimental study on manoeuvring motion of a ship in waves. In: Proc. of Int'l conf. on Marine Simulation and Ship Manoeuvrability (MARSIM'03). Kanazawa, Japan.
- [62] Vantorre, M., 2001. Manoeuvring coefficients for a container carrier in shallow water: an evaluation of semi-empirical formulae. 23rd ITTC Manoeuvring Committee.

- [63] Vantorre, M., Eloot, K., 1997. Requirements for standard harmonic captive manoeuvring tests. 4th IFAC Conf. on Manoeuvring and Control of marine craft. Brijuni, Croatia.
- [64] Vukcevic, V., Jasak, H., 2016. Validation and verification of decomposition model based on embedded free surface method for oblique wave seakeeping simulations. In: Proc. of Tokyo 2015: a workshop on CFD in ship hydrodyn. Tokyo, Japan.
- [65] Wicaksono, A., Kashiwagi, M., 2019. Efficient coupling of slender ship theory and modular maneuvering model to estimate the ship turning motion in waves. In Proc. of the 29th Int'l Ocean and Polar Engineering Conference, Honolulu, USA.
- [66] Xing, T., Bhushan, S., Stern, F., 2012. Vortical and turbulent structures for KVLCC2 at drift angle 0, 12, and 30 degrees. J. Ocean Eng. 55, 23-43.
- [67] Xu, Y., Kinoshita, T., Itakura, H., 2007. A PMM experimental research on ship maneuverability in waves. In: Proc. of the 26th Int. Conf. on Offshore Mech. and Arctic Eng., California, USA.
- [68] Yamato, H., Koyama, T., Uetsaki, H., 1990. Automatic berthing by the neural controller. In: Proc. of the 9th Ship Control Systems Symposium, Maryland Bethesda, MD, USA.
- [69] Yao, J., Liu, Z., Song, X., Su, Y., 2021. Ship manoeuvring prediction with hydrodynamic derivatives from RANS: development and application. J. Ocean Eng. 231, 109036.
- [70] Yasukawa, H., 2006. Simulation of ship maneuvering in waves (1st report: turning motion). J. Jpn. Soc. Naval Archit. Ocean Eng. 4, 127–136.
- [71] Yasukawa, H., 2008. Simulation of ship maneuvering in waves (2nd

- report: zig-zag and stopping manoeuvres). J. Jpn. Soc. Naval Archit. Ocean Eng. 7, 163–170.
- [72] Yasukawa, H., Adnan, F.A., 2006. Experimental study on wave-induced motions and steady drift forces of an obliquely moving ship. J. Japan Soc. of Naval Arch. and Ocean Eng., 3, 133-138.
- [73] Yasukawa, H., Adnan, F.A., Nishi, K., 2010. Wave-induced motions on a laterally drifting ship. J. Ship Tech. Res., 57(2), 84-98.
- [74] Yasukawa, H., Nakayama, Y., 2009. 6-DOF motion simulations of a turning ship in regular waves. In: Proc. Int'l Conf. on Marine Simulation and Ship Manoeuvrability. Panama, Panama.
- [75] Yasukawa, H., Hasnan, M.A.A., Matsuda, A., 2021. Validation of 6-DOF motion simulations for ship turning in regular waves. J. Mar. Sci. and Tech. 26, 1096-1111.
- [76] Yasukawa, H., Hirata, N., Yonemasu, I., Terada, D., Matsuda, A., 2015. Maneuvering simulation of a KVLCC2 tanker in irregular waves. In: Proc. of Int'l Conference on Marine Simulation and Ship Manoeuvrability (MARSIM2015). Newcastle, UK.
- [77] Yasukawa, H., Yoshimura, Y., 2015. Introduction of MMG standard method for ship maneuvering predictions. J. Mar. Sci. and Tech. 20, 37-52.
- [78] Yen, T.G., Zhang, S., Weems, K., Lin, W.M., 2010. Development and validation of numerical simulations for ship maneuvering in calm water and in waves. In: Proc. of 28th Sym. on Naval Hydrodyn. California, USA.
- [79] Yoon, H., 2009. Phase-averaged stereo-PIV flow field and force/moment/motion measurements for surface combatant in PMM maneuvers. PhD Dissertation. The Univ. of Iowa, USA.

- [80] Zalesak, S.T., 1979. Fully multidimensional flux-corrected transport algorithms for fluid. *J. Comput. Phys.* 31(3), 335-362.
- [81] Zhang, W., Moctar, O.El., Schellin, T.E., 2020. Numerical simulations of a ship obliquely advancing in calm water and in regular waves. *Applied Ocean Res.*, 103, 102330.
- [82] Zhang, W., Zou, Z.J., Deng, D.H., 2017. A study on prediction of ship maneuvering in regular waves. *Ocean Eng.* 137, 367–381.

APPENDIX. Application of KCS Manoeuvring Coefficients

To continue the validation work for the PMM tests in calm sea shown in Section 4.1. The manoeuvring coefficients of KCS model obtained from the PMM tests are compared with the data of existing research works, as summarized in Table A.1. The results of both PMM tests and circular motion tests (CMT) are involved, and the corresponding experimental center and methods are also listed. The methods include both the experimental tests and the CFD computations. The roll-fixed condition was applied by these cited works, although the model scale can be different. The values of some coefficients are blank in the table because the data cannot be directly found from the cited papers. In the reference part, the “present” represents the present numerical PMM tests. It can be seen that different cited studies have shown similar linear coefficients. The coefficient Y_r is always of small magnitude, so its discrepancy is relatively large.

The 35° turning trajectories predicted by the present manoeuvring coefficients are given in Fig. A.1. The MMG model introduced by **Yasukawa and Yoshimura (2015)** and the coefficients of propulsion/rudder models given by **Sung (2013)** and **Sung and Park (2015)** are adopted for the trajectory prediction. The open water parameters of propeller models are from **SIMMAN (2020)**. The initial Fr condition is 0.26 for these cases shown in Fig. A.1. The “FR” indicates the free-running experiments.

Table A.1(a) Comparison on the manoeuvring coefficients of KCS model at $Fn=0.26$

Test type	PMM					CMT		
	Exp.	Exp.	CFD	CFD	CFD	Exp.	Exp.	Exp.
Exp. center	HMRI	HMRI				NMRI	NMRI	JMU
Program			StarCCM	Present	StarCCM			
L	5.75 m	5.75 m	5.75 m	5.75 m	4.37 m	3.05 m	-	2.19 m
X_{yy}	-0.0730	-	-	-0.0719	-0.1309	-0.0549	-0.0726	-0.0603
Y_v	-0.2491	-0.2591	-0.2493	-0.2450	-0.1993	-0.2252	-0.2310	-0.2162
Y_{yyy}	-1.7474	-1.7212	-1.5388	-1.6670	-4.4574	-1.7179	-1.6350	-1.7028
N_v	-0.1434	-0.1421	-0.1442	-0.1386	-0.1093	-0.1111	-0.1130	-0.1172
N_{yyy}	-0.2530	-0.2666	-0.2947	-0.2335	0.0264	-0.1752	-0.1653	-0.1710
X_{rr}	-0.0172	-	-	-0.0292	-0.0767	-0.0120	-0.0139	-0.0162
Y_r	-	-	-	0.0135	0.0412	-	0.0424	-
Y_{rrr}	-0.0269	-0.0228	-0.0076	-0.0415	-0.2619	-0.0050	0.0050	-0.0105
N_r	-0.0486	-0.0462	-0.0475	-0.0437	-0.0497	-0.0465	-0.0446	-0.0443
N_{rrr}	-0.0310	-0.0313	-0.0343	-0.0509	-0.2216	-0.0387	-0.0344	-0.0369
Reference	Sung (2013)	Sung et al. (2015)	Sung et al. (2015)	Present	Liu et al. (2018)	Yoshimura et al. (2008)	Yasukawa et al. (2021)	Fukui et al. (2016)

Table A.1(b) Comparison on the manoeuvring coefficients of KCS model at $F_n=0.26$

Test type	PMM					CMT		
	Exp.	Exp.	CFD	CFD	CFD	Exp.	Exp.	Exp.
Exp. center	HMRI	HMRI				NMRI	NMRI	JMU
Program			StarCCM	Present	StarCCM			
L	5.75 m	5.75 m	5.75 m	5.75 m	4.37 m	3.05 m	-	2.19 m
X_{vr}	-0.0756	-0.0603	-0.0601	-0.1042	0.1320	-	-0.0424	-
Y_{vrr}	-0.4685	-0.5461	-0.4586	-0.9899	-5.4207	-0.8341	-0.8050	-0.8564
Y_{rvv}	-0.4236	-0.4444	-0.4506	-0.3262	-0.2174	-0.4832	-0.3090	-0.5658
N_{vrr}	-0.0498	-0.0570	-0.0768	-0.1472	-0.7883	-0.0512	-0.0349	-0.0200
N_{rvv}	-0.6943	-0.7339	-0.7442	-0.6940	-0.6444	-0.6168	-0.6094	-0.5602
Y_{v_dot}	-0.1895	-0.1881	-0.1687	-0.1718	-0.1839	-	-	-
N_{v_dot}	-	-	-	0.0101	0.0049	-	-	-
Reference	Sung (2013)	Sung et al. (2015)	Sung et al. (2015)	Present	Liu et al. (2018)	Yoshimura et al. (2008)	Yasukawa et al. (2021)	Fukui et al. (2016)

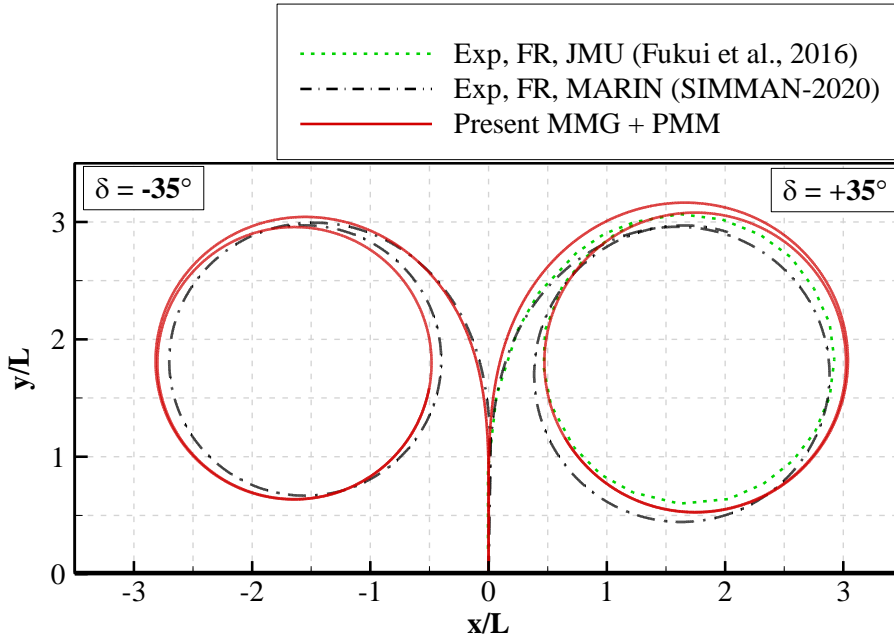
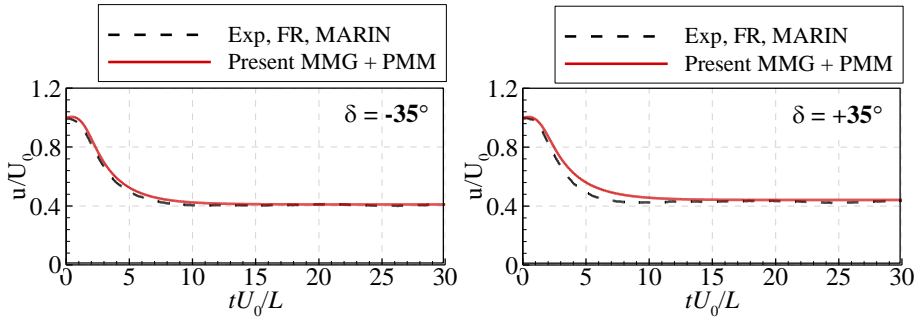


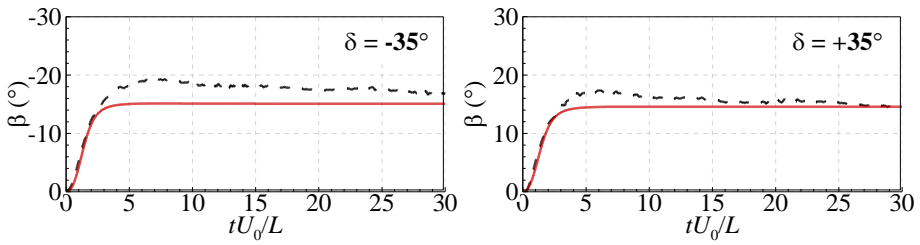
Fig. A.1 Prediction on the KCS 35° turning trajectories

The steering rate that equals 2.33°/s for the full-scale ship was used for both the MARIN and the present prediction. For the manoeuvring trajectories, The the $\delta = -35^\circ$ indicates a port side turning and $\delta = +35^\circ$ indicates a starboard side turning. The manoeuvring indexes are given in Table A.2.

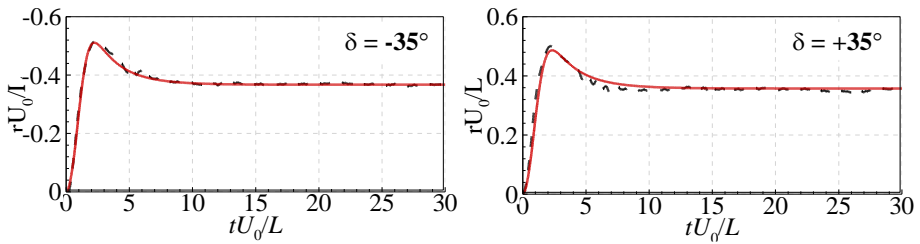
Compared with the free running trajectories, the present prediction generates a higher advance and a higher transfer distance. This discrepancy is more obvious for the $\delta = +35^\circ$ case due to a speed drop observed in Fig. A.2. This discrepancy may come from the roll effect. A strong interaction between the high speed, the roll motion, and the asymmetric propulsion exists at the initial turning stage, resulting a high heel attitude observed in the free-running measurement shown in Fig. A.2.



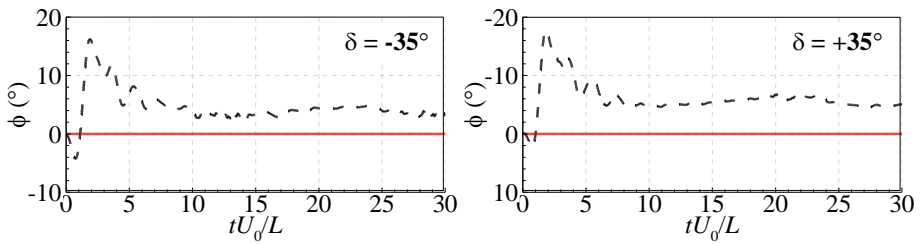
(a) Surge speed



(b) Drift angle



(c) Yaw rate



(d) Roll angle

Fig. A.2 Ship motion signals of 35° turning trajectories

Table. A.2 Comparison on the manoeuvring indices of 35° turning trajectories

Index	$\delta = -35^\circ$			$\delta = +35^\circ$		
	MARIN exp.	Present PMM	Rel. diff.	MARIN exp.	Present PMM	Rel. diff.
Advance distance A_D/L						
Transfer distance T_R/L	2.934	2.998	2.20%	2.902	3.119	7.50%
Tactical diameter T_D/L	-1.085	-1.205	11.10%	1.207	1.3	7.70%
Turning diameter D_T/L	-2.64	-2.775	5.10%	2.831	2.997	5.90%
Maximum speed U/U_0	2.298	2.339	1.80%	2.497	2.572	3.00%
Maximum drift angle β_0	1	1.005	0.50%	1	1.005	0.50%
Maximum yaw rate rL/U_0	-19.305°	-14.622°	-24.30%	-17.384°	-14.169°	-18.50%
Steady speed U/U_0 (at the time $tU_0/L = 30$)	-0.514	-0.511	-0.60%	-0.501	-0.487	-2.80%
Steady drift angle β_0 (at the time $tU_0/L = 30$)	0.41	0.409	-0.20%	0.437	0.438	0.20%
Steady yaw rate rL/U_0 (at the time $tU_0/L = 30$)	-16.865°	-14.622°	-13.30%	14.393°	14.169°	-1.60%

초록

파랑 중 선박 조종계수 추정을 위한 수치 PMM 해석에 대한 연구

주 장

조선해양공학과

공과대학

서울대학교

파랑 중 선박의 조종성을 평가하기 위하여 지난 수십 년 동안 많은 방법들이 제안되었습니다. 대표적인 접근 방법 중 하나는 선박의 내향-조종 연성을 통한 해석 기법입니다. 그러나 이러한 내향-조종 연성 해석의 주요 한계는 정수 중 바다 조건을 기반으로 단순화된 조종 모델을 사용하였으며, 이를 바탕으로 조종 계수들을 얻었다는 점입니다. 또한 이런 조종 모델과 조종 계수들은 파랑에 의한 효과가 무시되어 있습니다. 따라서 파랑 중에서의 수학적 모델이나 조종 계수들을 재검토할 필요가 있습니다.

이 연구는 파랑 중에서 일련의 PMM 테스트를 수행하여 조종 계수에 대한 파랑의 효과를 관찰하는 것을 목표로 합니다. 테스트 모델로는 KCS 컨테이너선을 사용하였습니다. 첫째, CFD 방식을 기반으로 수치 수조를 구축하였으며, VOF (Volume of Fluid) 기법 및 wave forcing 방식을 적용하여 파랑을 생성 및 유지합니다. PMM 운동과 파도에 의한 운동 응답이 연성된 선박 운동은

쿼터니언(quaternion) 기반의 6 자유도 운동알고리즘에 의해 계산됩니다. PMM 운동 중 발생하는 강한 난류 흐름을 계산하기 위해 안정화된 $k-\omega$ SST 난류 모델을 적용하였습니다.

둘째, KCS 모델의 정수 중 PMM 시험과 내항 시험에 대한 수치적 불확도 및 검증 (validation)을 확인하였습니다. 정수 중 PMM의 경우 정적 사향 시험 (static drift test), 순수 좌우동요 시험 (pure sway test), 순수 선수동요 시험 (pure yaw test) 및 선수동요 사향각 시험 (combined drift-yaw test)을 포함한 여러 PMM 테스트를 실험 결과를 통해 검증하였습니다. 선박 내항 시험의 경우, 파도에 의한 운동 응답 및 부가 저항을 다양한 파 주파수 또는 파향에 대해 검증하였습니다.

셋째, 기존의 PMM 시험에 추가로 입사파 조건이 도입되었습니다. 저주파 PMM 운동과 상대적 고주파인 파랑에 의한 운동 응답 간의 연성은 파랑 중 선박의 동적 거동 및 동적 PMM 시험에 의한 메모리 효과와 같은 문제들을 야기합니다. 이러한 문제가 논의되었습니다. 파랑 중 PMM 시험을 위해 다양한 파도 조건을 고려하였고, 파 주파수, 파 기울기, 파향에 따른 조종계수의 변화를 관찰하였습니다.

주요어: 파랑 중 조종성, 조종계수, 수치 PMM, CFD, KCS

학번: 2017-34082